

Universidade de São Paulo  
Instituto de Física

Propriedades Vibracionais e Estruturais das  
Escuteruditas Preenchidas  $R\text{Fe}_4\text{Sb}_{12}$   
( $R = \text{Na}, \text{K}, \text{Ca}, \text{Sr}, \text{Ba}$ )

Juliana Gonçalves de Abrantes

Orientador: Prof. Dr. Fernando Assis Garcia

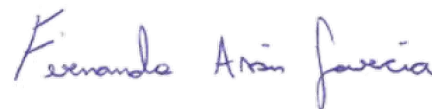
Dissertação de mestrado apresentada ao Instituto de Física  
da Universidade de São Paulo, como requisito parcial para  
a obtenção do título de Mestra em Ciências.

Banca Examinadora:

Prof. Dr. Fernando Assis Garcia - Orientador (IF-USP)

Prof. Dr. Lucas Carvalho Veloso Rogrigues (IQ-USP)

Profa. Dra. Cris Adriano (IFGW-UNICAMP)



São Paulo  
2022

**FICHA CATALOGRÁFICA**  
**Preparada pelo Serviço de Biblioteca e Informação**  
**do Instituto de Física da Universidade de São Paulo**

Abrantes, Juliana Gonçalves de

Propriedades vibracionais e estruturais das escuteruditas preenchidas  $RFe_4Sb_{12}$  ( $R = Na, K, Ca, Sr, Ba$ )/ Vibrational and structural properties of  $RFe_4Sb_{12}$  ( $R = Na, K, Ca, Sr, Ba$ ) filled skutterudites. São Paulo, 2022.

Dissertação (Mestrado) – Universidade de São Paulo. Instituto de Física. Depto. de Física Aplicada.

Orientador: Prof. Dr. Fernando Assis Garcia

Área de Concentração: Cristalografia

Unitermos: 1. Espectroscopia de raio X; 2. Cristalografia de raios X; 3. Termoeletricidade.

USP/IF/SBI-043/2022

University of São Paulo  
Physics Institute

Vibrational and Structural Properties of the  
 $R\text{Fe}_4\text{Sb}_{12}$  ( $R = \text{Na}, \text{K}, \text{Ca}, \text{Sr}, \text{Ba}$ ) Filled  
Skutterudites

Juliana Gonçalves de Abrantes

Supervisor: Prof. Dr. Fernando Assis Garcia

Dissertation submitted to the Physics Institute of the University of São Paulo in partial fulfillment of the requirements for the degree of Master of Science.

Examining Committee:

Prof. Dr. Fernando Assis Garcia - Supervisor (IF USP)

Prof. Dr. Lucas Carvalho Veloso Rorigues (IQ-USP)

Prof. Dr. Cris Adriano (IFGW-UNICAMP)

São Paulo  
2022



# Agradecimentos

Antes de mais nada, gostaria de agradecer a meus pais, Ana Lúcia e Rui, por todo o apoio e suporte, oferecidos generosamente e entregues nas mais variadas formas. Igualmente, sou grata às minhas irmãs, Cristina e Beatriz, por estarem presentes em momentos de importantes decisões, e sempre oferecerem seu carinho e companheirismo.

Agradeço imensamente a meu orientador, Prof. Dr. Fernando Assis Garcia, que me recebeu e investiu em mim desde o início dessa trajetória, apoiando a consolidação da minha educação e conduzindo meu desenvolvimento científico. Se mostrou presente, solícito e gentil em tantas ocasiões, e por isso, muito obrigada.

Quero agradecer a meus companheiros do grupo de pesquisa e outros amigos que fiz na Física, principalmente Pâmela Costa e Elielson Pereira, cuja amizade e ajuda foram indispensáveis para que eu pudesse concretizar mais esta etapa.

Agradeço, ainda, a todos os amigos, familiares e companheiros de caminhada que, além de darem sentido a cada dia vivido, ofereceram sua amizade mesmo quando a academia exigia a minha ausência.

Gostaria de deixar meus agradecimentos ao CNPEM-LNLS por possibilitar este projeto e outros tantos com impecável qualidade científica, com destaque aos pesquisadores do LCTE-Sirius, Danusa e Jairo, por me receberem tão bem durante o treinamento de montagem e manipulação de células de pressão.

Agradeço a todos os professores e demais colaboradores deste trabalho, que participaram ativamente de meu desenvolvimento acadêmico e permitiram que este projeto fosse realizado, além dos que não tiveram uma participação tão direta mas cuja influência se perpetua em minhas escolhas. Estes incluem queridos professores do IQ-USP, primeira base em minha carreira científica.

Agradeço ao Prof. Marcos Ávila e seu aluno Cesar Sônego pela colaboração no trabalho de síntese de outros materiais quânticos.

O presente trabalho foi realizado com apoio da Coordenação de Aperfeiçoamento de Pessoal de Nível Superior - Brasil (CAPES) - Código de Financiamento 001, a quem também devo agradecer por possibilitar o contínuo desenvolvimento científico do país e, particularmente, por possibilitar que eu me dedicasse a esta pesquisa.

Finalmente, quero agradecer profundamente a todas as pessoas que passaram por essa trajetória, seja no meio acadêmico ou não, mas que certamente influenciaram meu caminho e de alguma forma me ofereceram recursos que me trouxessem até aqui.



# Abstract

Skutterudites form a large family of intermetallic solid state functional materials presenting a high potential for thermoelectric applications. They are known to present a wide range of physical properties related to quantum many-body effects, such as superconductivity and magnetism, and in some instances strong electronic correlations giving rise to unexpected physical phenomena, that are sensitive to tuning parameters such as pressure, magnetic fields and chemical substitution. The resulting phase diagrams are rich and diverse. Accordingly, this type of material is in the spotlight of studies in many fields of research, given the vast number of phenomenological possibilities that remain unexplored.

In fact, our group has a longstanding interest in the properties of skutterudite materials and in particular in the subject of this dissertation: the  $R\text{Fe}_4\text{Sb}_{12}$  ( $R = \text{Na, K, Ca, Sr and Ba}$ ) filled skutterudites. This particular series is an example of one of the most challenging problems in condensed matter physics, which is the description of magnetic properties of the itinerant magnets. In this type of magnetism, the magnetic moment per magnetic atom site (in this case, the Fe site) is much smaller than expected for localized spins, suggesting their delocalization. Thence, itinerant magnets are also called small moment magnets. We addressed their electronic properties in order to investigate the nature of their magnetism and XANES (X-ray Absorption Near Edge Structure) experiments were performed, probing the local electronic structure of the  $\text{FeSb}_3$  coordination. It was noteworthy to find that this local structure could be connected to their magnetic behaviour, despite the character of their magnetism being itinerant.

Nevertheless, what seems the main subject triggering most of the skutterudite oriented research is indeed their large potential for thermoelectric applications. Hence, in this dissertation we turn our attention to other properties of the  $R\text{Fe}_4\text{Sb}_{12}$  ( $R = \text{Na, K, Ca, Sr and Ba}$ ) series, namely their vibrational and structural properties, all of which intimately relate to their thermoelectric properties. This way, we are able to present an integral picture of this series of skutterudites, so as to unravel the effect of the  $R$  filler atom substitution among them.

In a first approximation, the good thermoelectric properties of  $R$  filled skutterudites are assigned to specific phonon modes inserted in the system through the presence of the  $R$  filler cations, that are believed to be weakly coupled to the rest of the structure. In this dissertation, we show that this scenario is not outright, and does not comprise all the  $R$  filled materials. This is exposed in the first set of results, that examined the vibrational dynamics of the materials by means of X-Ray Absorption Spectroscopy (XAS) experiments. Additionally, a systematic structural analysis of the materials is conducted via X-Ray Diffraction (XRD) as function of pressure, where the elastic properties of the materials are probed. These lead to theoretical calculations about the bonding properties, aiming to unwind some unexpected features of our experimental findings.

Altogether, with the aid of EXAFS and XRD experiments, we hope to deliver a comprehensive study of the thermoelectric  $R\text{Fe}_4\text{Sb}_{12}$  ( $R = \text{Na, K, Ca, Sr and Ba}$ ) filled skutterudites, providing a complete overview of their vibrational, elastic and bonding properties.

**Keywords:** filled skutterudites; x-ray absorption spectroscopy; thermoelectric materials.





# Resumo

Escuteruditas formam uma grande família de materiais funcionais intermetálicos que apresentam um alto potencial para aplicações termoelétricas. São conhecidos por apresentar uma ampla gama de propriedades físicas relacionadas a efeitos quânticos de muitos corpos, como supercondutividade e magnetismo e, em alguns casos, fortes correlações eletrônicas que dão origem a fenômenos físicos inesperados, sensíveis a parâmetros de ajuste como pressão, campos e substituição química. Os diagramas de fase resultantes são portanto ricos e diversificados. Nesse sentido, esse tipo de material está no centro das atenções de estudos em diversas áreas de pesquisa, dado o grande número de possibilidades fenomenológicas que permanecem inexploradas.

De fato, nosso grupo tem um interesse de longa data nas propriedades das escuteruditas, em particular na série presente nesta dissertação: as escuteruditas preenchidas  $RFe_4Sb_{12}$  ( $R = Na, K, Ca, Sr$  e  $Ba$ ). Esta série em particular representa um dos problemas mais desafiadores da física da matéria condensada, que é a descrição das propriedades magnéticas dos magnetos itinerantes. Neste tipo de magnetismo, o momento magnético por sítio de átomo magnético (neste caso, Fe) é muito menor do que o esperado para spins localizados, sugerindo sua delocalização. Por isso, magnetos itinerantes também são chamados de magnetos de momento pequeno. Na ocasião, abordamos suas propriedades eletrônicas para investigar a natureza de seu magnetismo e realizamos experimentos de XANES (X-ray Absorption Near Edge Structure), sondando a estrutura eletrônica local da coordenação  $FeSb_3$ . Surpreendentemente, esta estrutura local mostrou-se estar ligada ao seu comportamento magnético itinerante.

No entanto, o que parece ser o principal assunto acerca das escuteruditas é seu potencial para aplicações termoelétricas. Assim, nesta dissertação voltamos a nossa atenção para outras propriedades da série  $RFe_4Sb_{12}$  ( $R = Na, K, Ca, Sr$  e  $Ba$ ), como suas propriedades vibracionais e estruturais, que estão intimamente relacionadas com suas propriedades termoelétricas. Desta forma, podemos apresentar um quadro integral desta série de escuteruditas, de modo a desvendar o efeito da substituição do átomo de carga R entre eles.

De início, as propriedades termoelétricas das escuteruditas preenchidas são atribuídas a modos de fônons específicos inseridos no sistema através da presença dos cátions R, que se acredita estarem fracamente acoplados ao resto da estrutura. Nesta dissertação, mostramos que este cenário não abrange todos os materiais preenchidos. Isso é exposto logo no primeiro conjunto de resultados, que descreve a dinâmica vibracional dos materiais por meio de Espectroscopia de Absorção de Raios-X (XAS). Além disso, é realizada uma análise estrutural sistemática dos materiais via Difração de Raios-X (DRX) em função da pressão, onde são apuradas as propriedades elásticas dos materiais. Estes levam a cálculos teóricos sobre as propriedades de ligação, com o objetivo de esclarecer resultados inesperados obtidos.

Assim, valendo-se de experimentos de XAS e XRD, esperamos apresentar um estudo abrangente das escuteruditas termoelétricas  $RFe_4Sb_{12}$  ( $R = Na, K, Ca, Sr$  e  $Ba$ ), fornecendo uma visão completa de suas propriedades vibracionais, elásticas e de ligação.

**Palavras-chave:** escuteruditas preenchidas; espectroscopia de absorção de raios-x; materiais termoelétricos.



# List of Figures

1.1	Most common representations for the structure of skutterudites. In (a), the representation shows the structure of the cage around the $R$ site. In (b), we show only the elements $M_4X_{12}$ , in order to show the chemical bond structure of the host. The formation of square rings $X_4$ is evident. The $R$ atom is represented in purple, $M$ in red and $X$ in yellow. . . . .	17
1.2	a) Dispersion relation between frequency and momentum. b) Dispersion relation for a two-spring system, originating two phonon modes: optica and acoustic (see main text). Both pictures adapted from [48]. . . . .	19
1.3	1D model adopted in the present work for discussion of the phonon models present in the lattice. Picture taken from [7]. $K_{cc}$ accounts for the effective spring constant between the Fe atoms in the cage, $K_{sc}$ for the spring constant between the Fe atom and Sb square ring, $K_{rc}$ between Fe and the filler atom, and $K_{rs}$ between filler atom and Sb square ring. . . . .	21
2.1	XRD powder data obtained for all the skutterudite samples at ambient pressure and temperature. . . . .	26
2.2	a) A typical XAS spectrum, b) Labels of absorption edges according to the origin of the core photoelectron. . . . .	27
2.3	Scheme of a Diamond Anvill Cell, with its elements stated on the picture [54]. .	33
2.4	Diameter size and geometry of culets to endure given pressures. Picture taken from [40]. . . . .	34
2.5	DAC mounting process. a) Piston and body of the open pressure cell. b) Alignment of the diamonds. c) Cell loaded with sample and ruby sphere. . . .	34
2.6	Scheme for the synchrotron accelerator. Adapted from < <a href="http://pd.chem.ucl.ac.uk/pdnn/inst2/work.h">http://pd.chem.ucl.ac.uk/pdnn/inst2/work.h</a> >, access in July/2022 [41]. . . . .	36
3.1	Temperature dependent X-ray absorption spectra for the $R = K, Ca$ and $Ba$ samples.	38
3.2	a) Local structure scheme of the chemical environment of the Fe absorber atom in the $R$ filled skutterudites. Red spheres represent the $R$ filler, green spheres the Sb and in blue the Fe atoms, being the absorber indicated in the figure. b) Examples of scattering paths for the photoelectron that may contribute to the EXAFS spectrum (adapted from [39]). . . . .	39
3.3	Real part of EXAFS for $R = K$ (black squares) and respective fitting (red lines), for all the temperature dependent spectra collected. The green lines show the subtraction between data and fitting. . . . .	40
3.4	Real part of EXAFS for $R = Ca$ (black squares) and respective fitting (red lines), for all the temperature dependent spectra collected. The green lines show the subtraction between data and fitting. . . . .	41

3.5	Real part of EXAFS for $R = \text{Ba}$ (black squares) and respective fitting (red lines), for all the temperature dependent spectra collected. The green lines show the subtraction between data and fitting. . . . .	42
3.6	Real part of EXAFS for $R = \text{Na}$ (black squares) and respective fitting (red lines), for all the temperature dependent spectra collected. The green lines show the subtraction between data and fitting. . . . .	43
3.7	Real part of EXAFS for $R = \text{Sr}$ (black squares) and respective fitting (red lines), for all the temperature dependent spectra collected. The green lines show the subtraction between data and fitting. . . . .	43
3.8	Debye-Waller parameters in function of $T$ for the single-scattering paths of the $R = \text{K}, \text{Ca}$ and $\text{Ba}$ samples, treated within the Einstein model for the $\text{Fe}-R$ path and Debye model for the remaining $\text{Fe}-Y$ scattering paths. . . . .	45
3.9	a) Representation of the skutterudite unit cell applied to the 1D model for phonon dispersion. In blue, the $\text{Fe}$ atoms belonging to the cage, in red, the $R$ fillers and in green the $\text{Sb}$ atoms, forming a square ring that vibrates inside the metallic structure. b) One dimensional model of the skutterudite unit cell, containing three different masses (rattler, square $\text{Sb}$ ring and $\text{Fe}$ ) and four different spring constants, between each pair of vibrating element. Figure adapted from [22]. . .	47
3.10	Phonon dispersion obtained from the 1D model for vibrational behaviour of the filled skutterudites. The first panel refers to the light cation filled materials ( $R = \text{K}, \text{Ca}$ ), while the second one represents the dispersion obtained for the heavy filler ( $R = \text{Ba}$ ) filled material. . . . .	49
3.11	Pressure dependent diffractograms for all the skutterudite samples. In red are highlighted the Bragg diffraction peaks for the corresponding material and pressure. . . . .	51
3.12	Background removal procedure for XRD data at higher pressures. . . . .	53
3.13	(a) The unit cell volume $V$ as function of $P$ . (b) The cage empty volume fraction $f_E$ as a function of $P$ . (c) The $P$ as a function of $V$ data and their respective fittings to the Birch-Murnaghan model. (d) The compressibility $\beta$ as a function of $P$ for all samples. . . . .	54
3.14	Total DOS and OPDOS for the AOs in the vicinity of $E_F$ taking part in the $\text{Ca } 3p-5p$ $\text{Sb}$ , $\text{Sr } 4d-5p$ $\text{Sb}$ and $\text{Ba } 5d-5p$ $\text{Sr}$ bonding MOs. In each panel, the left axis describes the DOS for all orbitals while the right axis shows the OPDOS. .	57
3.15	Contour plots for the MOs describing the filler-cage bonding in the $(x, y)$ plane in the cases of the $\text{Ca}$ , $\text{Sr}$ and $\text{Ba}$ filled materials as indicated, for low and high pressures. The figures are formed by 120 contours in the isovalue interval indicated in the color scale in the left side of the figure. Ligand Orbitals are plotted via the Gabedit program [1]. . . . .	59

# List of Tables

2.1	Rietveld refinement parameters for the skutterudite samples collected at ambient pressure. . . . .	25
3.1	The $\theta$ (either $\theta_D^{R,Fe-Y}$ or $\theta_E^{Fe-R}$ ) parameters obtained from the analysis of the correlated Debye-Waller parameters. . . . .	46
3.2	$K_{\text{eff}}$ parameters obtained from the analysis of the correlated Debye-Waller parameters. . . . .	46
3.3	Unit cell volume at room conditions and bulk modulus, extracted from the Birch-Murnaghan model for all $RFe_4Sb_{12}$ samples. . . . .	52
3.4	The highest filler derived superposing AOs to the formation of the MOs in the filler-cage bonding. The nature of the AOs and the symmetry character of the MOs are indicated. . . . .	56

# Contents

<b>1</b>	<b>Introduction</b>	<b>15</b>
1.1	Skutterudites . . . . .	15
1.2	Thermoelectricity . . . . .	17
1.3	Vibrational Properties . . . . .	18
1.4	Bonding Properties . . . . .	22
1.5	Elastic Properties . . . . .	23
<b>2</b>	<b>Materials and Methods</b>	<b>25</b>
2.1	Samples . . . . .	25
2.2	X-ray Absorption Spectroscopy . . . . .	27
2.2.1	XAS Experimental Conditions . . . . .	29
2.3	X-ray Diffraction . . . . .	30
2.3.1	XRD Experimental Conditions . . . . .	32
2.3.2	Diamond Anvil Cell . . . . .	32
2.4	Synchrotron Radiation . . . . .	35
<b>3</b>	<b>Results and Discussion</b>	<b>37</b>
3.1	EXAFS Analysis and Vibrational Properties . . . . .	37
3.1.1	Phonon Model . . . . .	47
3.2	XRD Analysis and Elastic Properties . . . . .	50
3.3	DFT Calculations and Bonding Properties . . . . .	55
<b>4</b>	<b>Summary and Conclusions</b>	<b>60</b>
<b>A</b>	<b>Keiber-Bridges model of correlated rattling motion</b>	<b>67</b>
<b>B</b>	<b>Scientific Outputs</b>	<b>71</b>
B.1	Papers . . . . .	71
B.2	Events . . . . .	71

# Chapter 1

## Introduction

In this chapter we introduce important concepts regarding the skutterudite materials, which are the subject of this research. In section 1.1, we present an overview of this intense research field; in section 1.2, the relevant theoretical aspects behind their properties are discussed; in the subsequent sections 1.3, 1.4 and 1.5, the models and premises employed in the interpretation of our experimental findings are presented.

### 1.1 Skutterudites

Skutterudites are a class of materials that greatly attract the interest of materials science community, given the diversity of properties they may present. The main physical properties of filled skutterudites are thermoelectricity, superconductivity, heavy-fermion and non-Fermi liquid behaviour, and magnetism. Antimony based skutterudites are commonly the most explored in terms of thermoelectric properties, which are favoured by their characteristic electronic structure [4]. These thermoelectrics present low cost of production, given the earth-abundance of the constituting elements, and they are particularly efficient in the medium-temperature regime, from 400 to 850 K [4, 57, 3]. The great interest in such appealing thermoelectrics resides in their high energy conversion efficiency, presenting itself as complementary or alternative to other non-renewable, usually less eco-friendly sources of power [57].

In this project, we work with the  $R\text{Fe}_4\text{Sb}_{12}$  ( $R = \text{Na}, \text{K}, \text{Ca}, \text{Sr}, \text{Ba}$ ) filled skutterudites, which adopt the  $\text{LaFe}_4\text{P}_{12}$  structure presented in the pioneering work of Jeitschko [21]. This structure is described by the body-centered cubic space group  $Im\bar{3}$ , and consists of a icosahedron formed by the Sb atoms, bordered by a cubic structure of Fe. At the centre of this structure resides the

site of the  $R$  filling elements, as can be seen in Figure 1.1 (a).

Binary skutterudites stem from the mineral skutterudite  $\text{CoAs}_3$  [17], and have the chemical formula  $M_4X_{12}$ . Since As and Sb belong to the same family, the binary material  $\text{CoSb}_3$  is isoelectronic to  $\text{CoAs}_3$  and also form a stable skutterudite structure. The  $M$  and  $X$  atoms arrange in a rigid cage framework, where  $M$  is a transition metal atom and  $X$  is usually a pnictide. The first proposal for chemical bonding scheme of this structure was also given by Jeitschko [21], which rationalized the structure stabilization in terms of the formation of  $M-X$  and  $X-X$  bondings. The more electronegative  $X$  atoms form square rings, stabilized through charge donation by the electropositive  $M$  atoms. In its turn, each  $M$  atom is coordinated by 6  $X$  atoms in octahedral geometry (see Figure 1.1 (a)-(b)). The number of electron-pair bondings in this structure is  $12 \times 2 X-X$  bondings plus  $\frac{4 \times 6}{2} M-X$  bondings, requiring a total of 72 electrons for an electron-precise formula. These electrons are provided by the  $4 \times \text{Co} 3d^7 4s^2$  electrons plus the  $12 \times \text{Sb} 5p^3$ , present in the valence band of those elements [35]. In this sense, the  $\text{CoSb}_3$  binary skutterudite can be accounted for a polyanionic Zintl compound [31, 26], where the resulting structure is stabilized due to the covalent character of the  $M-X$  and  $X-X$  bondings, and the octet rule is respected for all the atoms [20].

In the present case, the  $\text{FeSb}_3$  framework (or cage) is electron deficient when compared to the  $\text{CoSb}_3$ . Indeed, the total number of electrons of the  $\text{Fe}_4\text{Sb}_{12}$  formula unit is 68 [31]. The  $[\text{Fe}_4\text{Sb}_{12}]$  polyanion is thus stabilized by the addition of a filler cation in the cage's void, mainly by ionic charge donation to the cage. In a ternary  $RM_4X_{12}$  skutterudite, the  $R$  filler atom is usually a lanthanide, alkaline or alkaline earth metal (see Fig.1.1 (a)). Still, the  $R$  metals filling the skutterudites investigated in this work present charges  $R^{+1}$  or  $R^{+2}$ , always resulting in net electron deficiency. This grants metallic behaviour to the solid and electron deficiency is clearly observed since the charge carriers are holes. Moreover, paramagnetism or collective magnetism [17, 31] of the conduction electrons is also observed. Indeed, this particular series of skutterudites is known for presenting itinerant ferromagnetism [27, 46, 14].

Filling skutterudites' cages with guest atoms is also a consolidated method to enhance their thermoelectric qualities (high electric and low thermal conductivities). This effect can be attributed, in a simplified picture, to a relative uncoupling of the filler atom regarding the rest of the structure, such that they vibrate in rather independent, low dispersive modes, known as "rattling" modes. This scenario resembles the Einstein model of a solid, where atoms behave as independent harmonic oscillators [18]. In its turn, this may cause the scattering of phonons



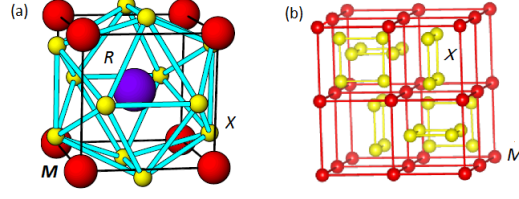


Figure 1.1: Most common representations for the structure of skutterudites. In (a), the representation shows the structure of the cage around the  $R$  site. In (b), we show only the elements  $M_4X_{12}$ , in order to show the chemical bond structure of the host. The formation of square rings  $X_4$  is evident. The  $R$  atom is represented in purple,  $M$  in red and  $X$  in yellow.

(quanta of vibrational energy) propagating throughout the lattice, or the insertion of phonons with low group velocity [32] in the material, thence reducing its thermal conductivity.

## 1.2 Thermoelectricity

Thermoelectric efficiency is commonly described in terms of the dimensionless figure of merit

$$ZT = \frac{S^2 \sigma}{\kappa} T$$

where  $S$  is the Seebeck coefficient (thermoelectric power),  $\sigma$  is the electrical conductivity,  $\kappa$  is the total thermal conductivity and  $T$  the absolute temperature of the system [32]. Thence, the enhancement of  $ZT$  can be achieved by tuning any one of these physical parameters, which are related to the chemical and electronical structures of the materials.

Knowing that the Seebeck coefficient is given by

$$S = \frac{8\pi^2 k_B^2 m^* T}{3eh^2} \sqrt{\left(\frac{\pi}{3n}\right)^2}$$

and the electrical conductivity is

$$\sigma = ne\mu_H$$

where  $m^*$  is the charge carrier effective mass,  $n$  is the number of carriers and  $\mu_H$  the carrier mobility, it is possible to manipulate the type and number of carriers or even the band structure aspects in order to raise  $ZT$ . One should bear in mind, however, that by adjusting one parameter, another one might be disturbed, as they are usually interrelated [49]. For instance,  $\kappa$  considers both lattice and electronic thermal conductivities,  $\kappa = \kappa_{latt} + \kappa_{elec}$ . By increasing the material

disorder, one can tune the lattice and electronic degrees of freedom for low thermal conductivity, but one would also get low electrical conductivity  $\sigma$ , promoting contradicting effects in  $ZT$ .

An alternative way to increase this figure of merit would be to reduce the lattice contribution to the total  $\kappa$  through phonon engineering without disturbing electrical conductivity. This strategy is particularly applied to filled (or partially filled) skutterudite materials, since they present high Seebeck coefficient and electron mobility, but also a large  $\kappa$  [3]. The kinetic theory tells us that

$$\kappa_{latt} = \frac{1}{3} C v_m l$$

where  $C$  is the specific heat of the material,  $l$  is mean free path of the phonons and  $v_m$  is the sound mean velocity [11]. Thereof, the scattering of phonons is an important mechanism through which  $ZT$  can be improved, which can be accomplished by interactions with electrons or other phonons. Electron-phonon scattering, however, would be detrimental to  $\sigma$ . We are thus left with the option of enhancing phonon-phonon scattering. One of the scattering principles that has been assigned to skutterudites is phonon scattering by the *rattling* of the filler atoms, which introduces localized vibrational modes that interact with propagating phonons in the lattice.

Other mechanisms that would sink thermal conductivity are the anharmonic scattering due to the three-phonon (Umklapp) [32] process and the reduction of the acoustic phonon group velocity [11], also obtained through the insertion of interacting phonon modes.

### 1.3 Vibrational Properties

In order to describe a solid in terms of the vibrations of atoms, it is possible to think of the system as a monoatomic chain of particles connected by virtual springs of constant  $g$  equally spaced in distance  $a$ , as in an one dimensional model. The force on the  $n^{th}$  particle is [48]

$$F_n = -\frac{\partial U}{\partial x_n}.$$

In this picture, each particle oscillates around its equilibrium position with one degree of freedom, and the potential energy of the system is given by

$$U = \sum \frac{g}{2} (\Delta x_i)^2 = \sum \frac{g}{2} (x_i - x_i^{eq})^2.$$

Considering that the equilibrium position of a particle in such a monoatomic chain is  $x_n^{eq} = na$ ,

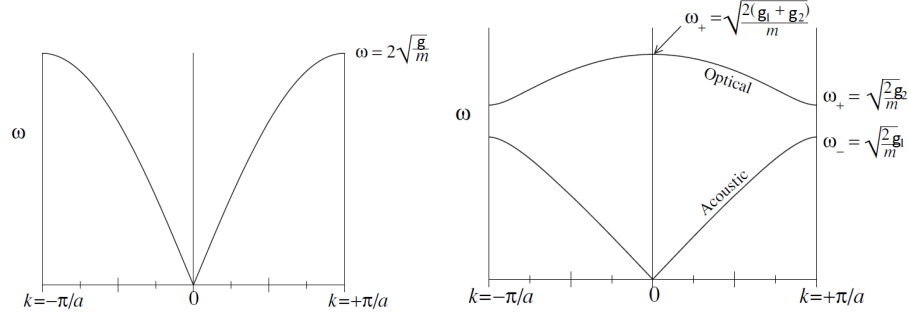


Figure 1.2: a) Dispersion relation between frequency and momentum. b) Dispersion relation for a two-spring system, originating two phonon modes: optical and acoustic (see main text). Both pictures adapted from [48].

a multiple of the distances of the masses at rest, the equation of motion for the  $n^{\text{th}}$  particle can be written

$$m\ddot{x}_n = g[(\Delta x_{n-1} - \Delta x_n) + (\Delta x_{n+1} - \Delta x_n)]$$

$$m\ddot{x}_n = g[(x_{n-1} - (n-1)a - x_n + na) + (x_{n+1} - (n+1)a - x_n + na)]$$

$$m\ddot{x}_n = g(x_{n-1} - 2x_n + x_{n+1})$$

to which we can propose a wavelike solution for the normal modes,

$$x_n = Ae^{i\omega t - ikx_n^{eq}} = Ae^{i\omega t - ikna}.$$

By supplanting this solution in the newtonian equation of motion, we can solve to find

$$\omega^2 = 2\frac{g}{m}(1 - \cos ka) = 4\frac{g}{m}\sin^2\left(\frac{ka}{2}\right)$$

$$\omega = 2\sqrt{\frac{g}{m}}\left|\sin\left(\frac{ka}{2}\right)\right|$$

This relation between the frequency  $\omega$  and the wavevector  $k$  is known as the dispersion relation and is displayed in Figure 1.2 (a).

Now, taking periodic boundary conditions (for an infinite solid),  $x_n = x_{N+n}$ , we get

$$e^{i\omega t - ikna} = e^{i\omega t - ik(N+n)a}$$

so obviously  $e^{ikNa} = 1$ . Therefore, the values of  $k$  are restricted to

$$k = \frac{2\pi r}{Na} = \frac{2\pi r}{L}$$

where  $L$  is the size of the chain and  $r$  is an integer referring to a normal mode. Of course, there will be as many normal modes as degrees of freedom in the system, in this case  $N$  modes.

Nevertheless, we can treat these particles as quantum harmonic oscillators, describing the energy of the atom by  $E_n = \hbar\omega(n + \frac{1}{2})$ , or, writing in terms of the Bosons state occupation number  $n(\beta\hbar\omega) = \frac{1}{e^{\beta\hbar\omega} - 1}$ ,

$$E_n(k) = \hbar\omega(k)[n(\beta\hbar\omega(k)) + \frac{1}{2}].$$

Reminding that  $\beta = \frac{1}{k_B T}$ , for a given temperature we have for each  $n$  a discrete vibrational mode with frequency  $\omega(k)$  dubbed phonon. In other words, we can define a phonon as a discrete quantum of vibration [48] for a given state  $n$  and momentum  $k$ .

For a large number  $N$  of atoms in the solid, with many possible  $k$  modes, one can describe the total energy of the system as an integral instead of a sum, as in

$$U = \frac{Na}{2\pi} \int_{-\pi/a}^{\pi/a} \hbar\omega(k) [n(\beta\hbar\omega(k)) + \frac{1}{2}] dk,$$

with corresponding density of states

$$D(\omega) = \frac{Na}{\pi} \left[ \frac{dk}{d\omega} \right].$$

The above mentioned model is nonetheless quite limited to describe real systems, as usually there is more than one type of atom (mass) in the material, or the geometry of the solid inserts different values for spring constants, rendering new degrees of freedom. These scenarios would give rise to wealthier dispersion relations, with more than one phonon mode available. Following a similar description as given above, for instance, for two different spring constants in the 1-D system, but omitted here for simplification, we would find two corresponding normal modes (branches) in the dispersion relation [48]:

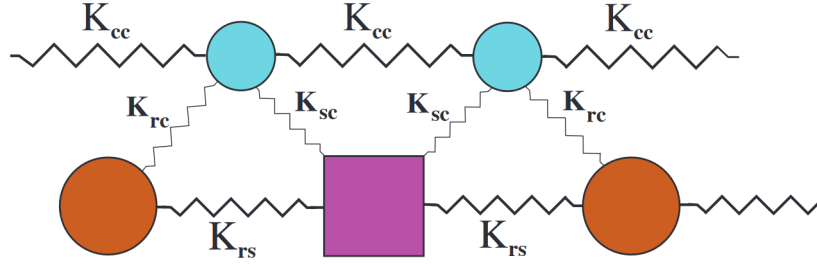


Figure 1.3: 1D model adopted in the present work for discussion of the phonon models present in the lattice. Picture taken from [7].  $K_{cc}$  accounts for the effective spring constant between the Fe atoms in the cage,  $K_{sc}$  for the spring constant between the Fe atom and Sb square ring,  $K_{rc}$  between Fe and the filler atom, and  $K_{rs}$  between filler atom and Sb square ring.

$$\omega_{\pm} = \sqrt{\frac{g_1 + g_2}{m} \pm \frac{1}{m} \sqrt{(g_1 + g_2)^2 - 4g_1g_2 \sin^2\left(\frac{ka}{2}\right)}}$$

which is better portrayed in Figure 1.2 (b).

Observe that one phonon mode presents linear dispersion as  $k \rightarrow 0$  and is known as the acoustic mode, whereas the other, at higher energies, is known as the optical mode. Usually, the former is associated with collective lattice vibrations, and dominates the phonon density of states at lower energies, whilst the latter modes are related to individual atoms vibrating in the lattice, causing a larger interatomic displacement and thus are more significant at higher temperatures [18].

For this work in particular, we have adopted an effective one-dimensional model of the vibrating elements in the unit cell projected into the [100] direction, introduced by Keiber *et al.* [22, 6]. It considers three elements in the lattice, namely the  $R$  filler (or rattler), the Sb square ring and the Fe metal cage, which denotes solely the Fe cubic lattice. The coupled character of the vibrational dynamics is given by connecting the elements by four distinct spring constants for each  $R$  filled skutterudite: a rattler-square ring ( $K_{rs}^R$ ), a rattler-metal cage ( $K_{rc}^R$ ), a metal cage-metal cage ( $K_{cc}^R$ ) and a metal cage-square ring ( $K_{sc}^R$ ), depicted in Figure 1.3.

Nonetheless, one should keep in mind that this is only a qualitative model, resulting in the phonon dispersion projected in the [100] plane, and does not reflect the total phonon dispersion of the system. Given the presence of four different spring constants, it results in four different (one acoustic, and three optical) phonon modes. The solution for this model is explained in detail in Appendix A, and the results are presented in section 3.1.1.

## 1.4 Bonding Properties

Density Functional Theory (DFT) is a method that uses the local or nonlocal electronic density of a system to calculate other components of the electronic structure, such as binding energies and bond lengths, or ground/excited states of a system [8]. It is an approximation to the actual very intricate many-body problem (interacting electrons in a system), with potentials due to the presence of the nuclei, coulombic interactions between particles, hopping interactions and so on. The DFT method is based on a first guess about the local/nonlocal electronic density, moving to iterating variables of the chosen functional until converging to a result, which shall coincide with the minimum energy of the system, in a self-consistent process.

In a nutshell, the system that should be described consists of electrons moving in an external potential due to the presence of nuclei, where the total energy of the system is

$$H = T + U + V_{ext}$$

in which  $H$  is the Hamiltonian,  $T$  is the kinetic energy present in the system,  $U$  is the internal potential energy and  $V_{ext}$  the external potential energy. According to the theory, these quantities only depend on the electronic density  $\rho(\vec{r}) = \int \Psi^*(\vec{r})\Psi(\vec{r})d\vec{r}$ , being  $\Psi(\vec{r})$  the multielectronic wave function, so

$$E[\rho(\vec{r})] = T[\rho(\vec{r})] + U[\rho(\vec{r})] + V_{ext}[\rho(\vec{r})].$$

Here, the internal potential term includes the Hartree term, that accounts for electron-electron interactions, and the exchange-correlation energy,

$$U[\rho(\vec{r})] = V_H[\rho(\vec{r})] + E_{xc}[\rho(\vec{r})].$$

The latter one is actually unknown and the most challenging to define in the computations.

This type of quantum chemistry calculation was employed in this work in order to unveil the bonding character between atoms, namely the main atomic orbital (AO) contributions of the filler atom in the overall molecular orbital (MO) of the unit cell. They were performed in collaboration with a group member, so the following description is limited to the main features of the calculation.

The type of chosen functional was the BP86, known for its good accuracy for treating

complexes, within the generalized gradient approximation (GGA) for the exchange-correlation potential. A sub-cell consistent of filler and cage containing 45 atoms was treated at quantum level, embedded in a supercell of 339 atoms [12], with their charges ascribed in agreement with a Zintl phase [31]. These systems are segregated from each other by two atomic layers characterized as capped effective core potentials (cECPs) [12]. This division is necessary to avoid spurious electron leakage, where the classically described point charges of the supercell induce the polarization of the quantum treated electronic waves. All atomic positions were obtained from experimental crystallographic data.

Furthermore, we have decided not to include spin-orbit coupling, since it presented negligible effects in the assessed orbital constitution, although it did affect the final energy of the system. The calculations were implemented using the ORCA 5.0 package [37, 38].

## 1.5 Elastic Properties

The elastic properties of solids can be described by the isothermal equation of state given by the Birch-Murnaghan model [5], that returns the pressure to which the material is subject in function of the unit cell volume:

$$P(V) = \frac{3}{2}B_0 \left[ \left( \frac{V}{V_0} \right)^{-7/3} - \left( \frac{V}{V_0} \right)^{-5/3} \right] \left\{ 1 + \frac{3}{4} (B'_0 - 4) \left[ \left( \frac{V}{V_0} \right)^{-2/3} - 1 \right] \right\}$$

where  $B_0$  and  $B'_0$  are respectively the bulk modulus and its first derivative with respect to pressure,  $V_0$  is the volume of the unit cell at room conditions, and  $V$  is the volume variable.

The bulk modulus parameter can be defined as:

$$B_0 = -V \left( \frac{\partial P}{\partial V} \right)_{T=cte}.$$

Rearranging terms, we can consider a small increment in pressure  $dP = -B_0 \frac{dV}{V}$ . As though, materials with large  $B_0$  demand larger pressure variations in order to cause any impact in its volume, which means that the bulk modulus reflects the rigidity, or incompressibility of the material.

Likewise, we can define the compressibility parameter as the inverse of the bulk modulus

$$\beta = \frac{1}{B_0} = -\frac{1}{V} \left( \frac{\partial V}{\partial P} \right)_{T=cte}.$$

In short, the Birch-Murnaghan model reflects the non-linear deformation suffered by solids under stress/strain, which happens because the elastic constants themselves are *not* actually constant, as stated by Hooke's Law, but instead rely on the initial stress, and hence on pressure when we consider infinitesimal variations [36]. This fact derives from the classical theory of crystal elasticity, where the pressure is related to the Helmholtz free energy by  $P = - \left( \frac{\partial F}{\partial V} \right)_{T=cte}$ , where  $F = \frac{1}{2} \left[ \left( \frac{V}{V_0} \right)^{-2/3} - 1 \right]$  is expanded in form of a series [5].



# Chapter 2

## Materials and Methods

This chapter is dedicated to explaining the technical aspects of sample synthesis and the physical theory behind the techniques that were employed in the concretion of this work.

### 2.1 Samples

The samples were synthesized using the Solid State synthering method [27] in collaboration with the Max Planck Institute for the Physics and Chemistry of Solids. The synthesis is made in two steps, first producing the binary antimonides of the guest atoms,  $RSb$ , and then reacting the stoichiometric mixture of  $RSb$ ,  $Sb$  and  $FeSb_2$  for one week at 400 °C. High quality polycrystalline samples were obtained for  $RFe_4Sb_{12}$  ( $R = Na, K, Ca, Sr, Ba$ ) skutterudites.

X-ray diffraction experiments at ambient conditions were performed in order to verify the phase purity and crystallographic quality of the samples. This first result is shown in Figure 2.1, for each  $R$  filled skutterudite, where they are compared to the simulated diffraction pattern for their corresponding phase profile. The peaks highlighted in blue around 29° refer to a residual Sb phase (about 2%, quantity that we obtained via Rietveld refinement), provenient from the synthesis process. The statistical parameters obtained from the refinement are presented in Table 2.1.

	$R = Na$	$R = K$	$R = Ca$	$R = Sr$	$R = Ba$
$R_p$	5.85%	5.37%	4.64%	6.07%	4.74%
$R_{wp}$	8.41%	7.55%	6.83%	9.49%	6.72%
$\chi^2$	2.78	1.65	1.61	3.56	2.93

Table 2.1: Rietveld refinement parameters for the skutterudite samples collected at ambient pressure.

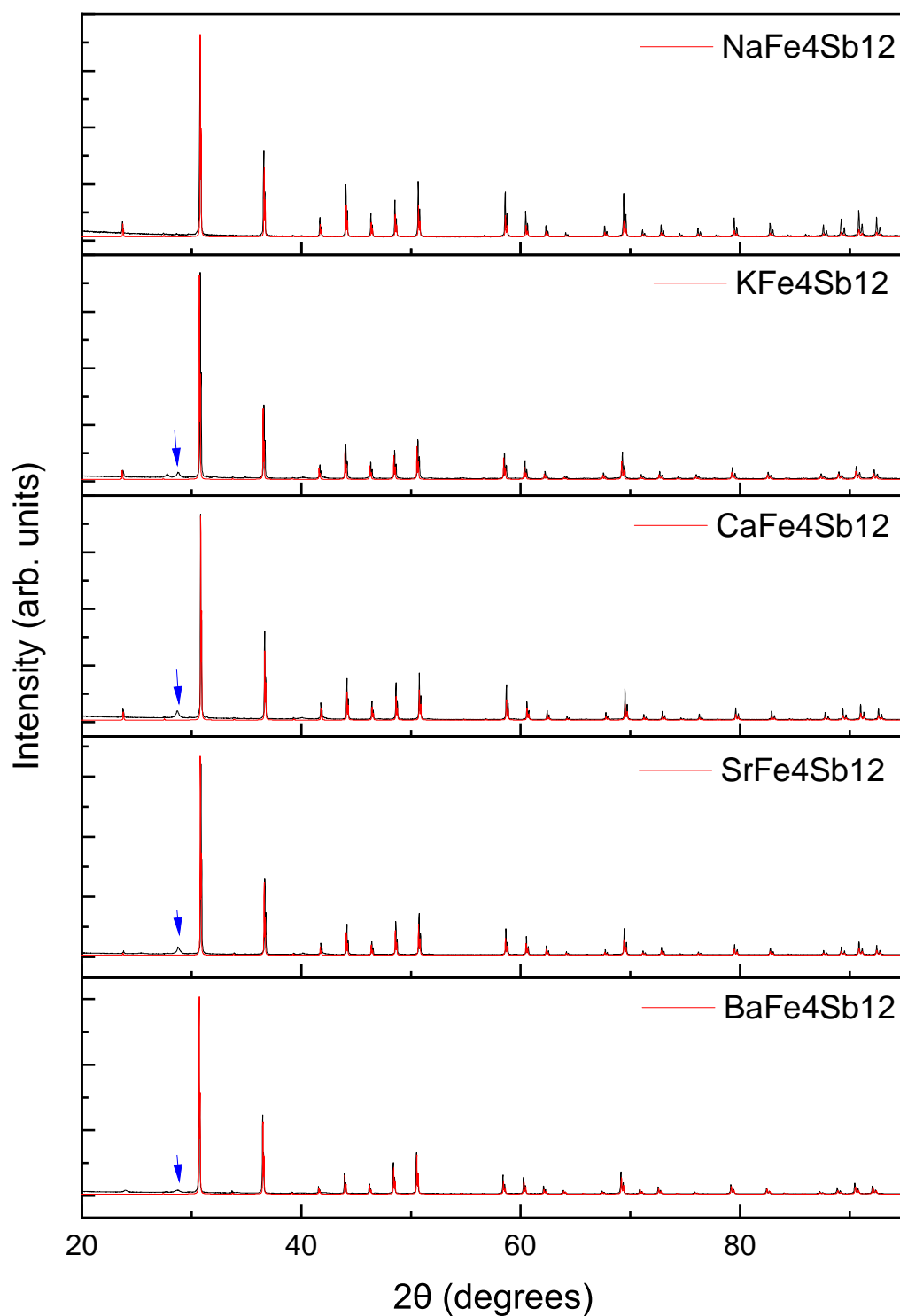


Figure 2.1: XRD powder data obtained for all the skutterudite samples at ambient pressure and temperature.

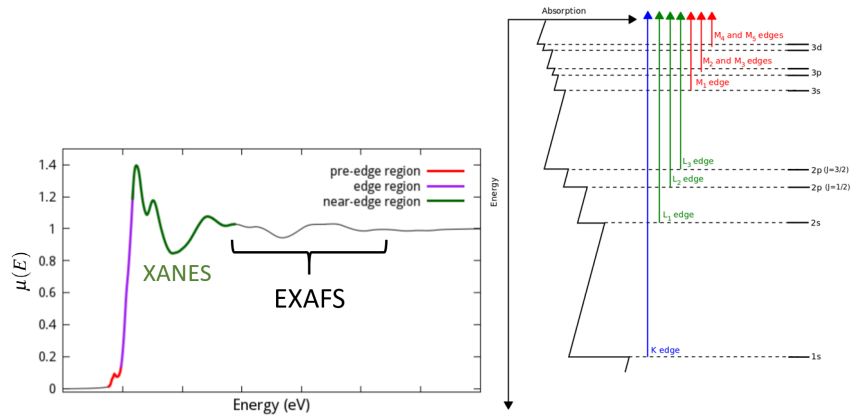


Figure 2.2: a) A typical XAS spectrum, b) Labels of absorption edges according to the origin of the core photoelectron.

## 2.2 X-ray Absorption Spectroscopy

X-ray absorption spectroscopy (XAS) is based on the photoelectric effect, where a photon is absorbed by a core electron ( $1s$  or  $2p$  level) of a given atom in the material. Then, this electron either can be excited to the Lowest Unoccupied Molecular Orbital (LUMO), or to the continuum, giving rise to a sharp absorption mark, known as the absorption edge of the spectrum. This phenomenon grants kinetic energy to the photoelectron, causing it to scatter among the neighboring atoms [56].

A typical absorption spectrum is the sum of these two effects (absorption and scattering), so the spectrum can be analysed in parts in order to extract different types of information about the sample. XANES (X-ray Absorption Near Edge Spectroscopy) refers to the pre-edge and near-edge portion of the spectrum, and EXAFS (Extended X-ray Fine Structure) ascribes to the oscillating part in higher energies (see Figure 2.2 (a)). The characteristic rippling of EXAFS concerns to the interference between the wave function of the emitted electron with the scattered electrons from the atoms that surround the absorbing element.

However, one should keep in mind that what is actually being detected is usually the fluorescence photon originated in the decay of outer shell electrons when fulfilling the core hole created. When fulfilling a hole in the  $1s$  shell, we say that it is the  $K$ -edge that is being measured, the  $L$ -edge when fulfilling the  $2s$  shell, and so forth (Figure 2.2 (b)).

The absorption coefficient  $\mu(E)$  is given by the Lambert-Beer law, and reflects the probability of a photon to be absorbed. In transmission detection geometry,

$$I_t = I_0 e^{-\mu(E).x}$$

$$\mu(E) = \frac{1}{x} \ln \frac{I_0}{I_t}$$

where  $I_t$  is the intensity of the transmitted beam,  $I_0$  is the intensity of the incident beam and  $x$  is the sample thickness.

An alternative way to display the EXAFS spectrum, above the absorption edge, is in terms of the mentioned oscillations due to the scattering of the photoelectron in the neighboring atoms,

$$\chi(E) = \frac{\mu(E) - \mu_0(E)}{\Delta\mu_0(E)}$$

where  $\mu_0(E)$  is a background function regarding the absorption of a lone atom and  $\Delta\mu_0(E)$  the sharp rise at the absorption edge. Alternatively,  $\chi$  can be plotted in function of the wave number of the electron, since it holds the relation to energy

$$k = \sqrt{\frac{2m(E - E_0)}{\hbar^2}}.$$

The EXAFS equation  $\chi(k)$  will then emerge as a sophisticated function, that can ultimately be described as the transition between two quantum states, according to Fermi's Golden Rule [39]:

$$\mu(E) \propto |\langle f | \mathcal{H} | i \rangle|^2$$

where  $\mathcal{H}$  is the interaction term, that should be intricate, but proportional to the vector potential, according to quantum radiation theory. The initial state is basically the core electron plus an X-ray, whilst the final state consists of a core hole and a photoelectron, which is affected by the neighboring atoms. Thus, we can write it as the sum of contributions from the "bare atom" and the neighbors,  $|f\rangle = |f_0\rangle + |\Delta f\rangle$ , as to find

$$\mu(E) \propto |\langle f_0 | \mathcal{H} | i \rangle|^2 [1 + \langle \Delta f | \mathcal{H} | i \rangle \frac{\langle f_0 | \mathcal{H} | i \rangle^*}{|\langle f_0 | \mathcal{H} | i \rangle|^2} + \text{ComplexConjugate}]$$

Therefore, we can say that  $\chi(E)$  is proportional to the amplitude of the scattered photoelectron at the site of the absorbing atom [39]:

$$\chi(E) \propto \langle \Delta f | \mathcal{H} | i \rangle = \int dr \delta(r) e^{ikr} \Psi_{scatt}(r) = \Psi_{scatt}(0)$$

Considering that this wave-function can be written in terms of a damped spherical wave, that scatters elastically and inelastically,  $\Psi(k, r) = \frac{e^{ikr} e^{-2r/\lambda(k)}}{kr}$ , from the neighboring atoms at distances  $R_j$ , and inserting terms related to scattering properties and disorder of the system, we will finally get to the deep-seated EXAFS equation:

$$\chi(k) = \sum \frac{N_j e^{-2k^2 \sigma_j^2} e^{-2R_j/\lambda(k)} f_j(k)}{kR_j^2} \sin[2kR_j + \delta_j(k)]$$

where  $N$  is the coordination number of the neighbor species,  $k$  is the wave-number,  $\lambda$  is the mean-free-path of the photo-electron,  $\sigma$  the mean-square displacement of the distance  $R$ ,  $f$  and  $\delta$  concern the scattering properties of the atoms and are thus proportional to the atomic number.

It is important to notice that XAS is an element-specific technique: the energy of the incident beam is tunable to the excitation energy of the core electron, unique for each atomic species, residing in the X-ray range. That is why this type of experiment requires the use of synchrotron radiation, which presents high and tunable energy in the incident beam.

With XAS it is possible to probe the local structure of the element being studied. XANES spectra reports the electronic structure, and one can determine the oxidation state of the absorption atom by the edge position, and through the pre-edge structure it is possible to get information on what prohibited transitions are happening and thus what are the hybridizations involved in the system. As concerns EXAFS, one can probe the distance between atoms, the number and type of atoms in the coordination sphere, besides extracting information on the disorder of the system.

### 2.2.1 XAS Experimental Conditions

EXAFS experiments were performed on the XAFS2 [13] beamline of the Brazilian Synchrotron Laboratory (CNPEM-LNLS), where we have probed the  $K$ -edge of Fe for all skutterudite samples, in the energy range 6900 – 7900 eV.

A helium flow cryostat was used for the low temperature experiments, in the temperature range  $6 < T < 300$  K, and the temperature control was performed by a Lakeshore controller. In this setup, the flux of He gas has direct contact with the sample, cooling it down. The  $R = K$ , Ca and Ba skutterudite samples were investigated in detail, while just a few temperature points were collected for the  $R = Na$  and Sr samples. The experiment was planned this way in order to probe charge and mass effects, which could be accomplished by the investigation of the  $R = K$ , Ca and Ba samples.

The K and Ca materials were measured in fluorescence and transmission modes, while the data for the Ba sample were collected only in fluorescence mode. During the experiment, an Fe foil was measured at room temperature as a reference. High statistical measurements were obtained in all regions of the XAS spectra.

Sample preparation included powdering and sieving the synthesized polycrystals, before taking it to the ultrasound in an ethanol solution, in order to homogenize the distribution of varied sized particles. Then, this suspension is filtered into a membrane and dried in the stove, and finally fixed with gum. The attachment of kapton tape allows one to freely manipulate the sample during the experiments, since it is transparent to X-rays. It is important to ensure that this final sample is not too thick, in order to avoid over-absorption effects in the XAS measurements, which happens when the absorbed X-rays cause fluorescence, thus damping the EXAFS oscillations [39].

## 2.3 X-ray Diffraction

Knowing the structure of a given material is fundamental to understanding its physical and chemical properties. X-ray diffraction (XRD) is known for revealing the crystallographic characteristics of the materials, such as the lattice parameters, phase composition and space group to which belongs the crystal, providing valuable information about its structure.

The technique is based on the incidence of light over a crystalline sample, which will cause scattering of the beam by the atoms that compose the material. As they are organized in periodic positions, the wavefunctions of the scattered photons interfere constructively or destructively, resulting in an interference pattern. Actually, this periodic arrangement gives rise to virtual planes throughout the crystal in various directions, so it is possible to describe this phenomenon using the Bragg's Law [45],

$$n\lambda = 2d \sin \theta$$

where  $\lambda$  is the wavelength of the incident beam,  $\theta$  is the angle of incidence,  $d$  is the distance between these planes and  $n$  is the order of diffraction. It is important to notice that  $\lambda$  must be of the same magnitude of the interatomic distances, so light can interact with matter. Therefore, for a fixed energy of radiation, the constructive peaks occur at certain values of  $\theta$ , which are relative to a specific family of planes. These are labeled according to the positions where they intercept

the unit cell, using the Miller indexes  $hkl$  for a 3D lattice, so we can write

$$n\lambda = 2d_{hkl} \sin \theta.$$

In this project we have performed powder XRD experiments, which means that the polycrystals are randomly oriented in the sample, such that the resultant peaks are a sum of contributions of all the possible planes present in the three dimensional crystal.

The reason why XRD is so effective for characterization is because the positions  $\theta$  of the peaks in the diffractogram are, as given by the Bragg's Law, a product of the inter-plane distances, while their intensity reflect the atomic positions and respective electronic densities. This is actually a consequence of Fermi's Golden Rule applied to the scattering process, where the scattering potential of an atom is given by

$$V_{kk'} = \langle \mathbf{k}' | V | \mathbf{k} \rangle = \int d\mathbf{r} \frac{e^{-i\mathbf{k}' \cdot \mathbf{r}}}{\sqrt{L^3}} V(\mathbf{r}) \frac{e^{-i\mathbf{k} \cdot \mathbf{r}}}{\sqrt{L^3}}$$

$$V_{kk'} = \frac{1}{L^3} \int d\mathbf{r} e^{-i(\mathbf{k}' - \mathbf{k}) \cdot \mathbf{r}} V(\mathbf{r})$$

$$V_{kk'} = \frac{1}{L^3} \int d\mathbf{r} e^{-i(\mathbf{G}) \cdot \mathbf{r}} V(\mathbf{r}).$$

We know that  $\langle k' |$  and  $|k \rangle$  correspond to the final and initial states, which are respectively the scattered and incident plane waves, and  $\mathbf{G} = \mathbf{k}' - \mathbf{k}$  is the lattice vector in the reciprocal space. The integral term is known as the Structure Factor, that accounts for the unit cells that define the lattice, and the constituent particles in the basis of the crystal,  $\alpha$ :

$$S(\vec{G}) = \sum \int d\vec{r} e^{i\vec{G} \cdot (\vec{r} + \vec{y}_\alpha)} V_\alpha(\vec{r}) = \sum e^{i\vec{G} \cdot \vec{y}_\alpha} f_\alpha(\vec{G})$$

Where, assuming that the scattering potential is a sum over the contributions of all the atoms present in the system, we have defined the form factor as

$$f_\alpha(\vec{G}) = \int d\vec{r} e^{i\vec{G} \cdot \vec{r}} V_\alpha \vec{r}.$$

The Structure Factor can be alternatively described as the fourier transform of the electron density of the system [48]:

$$F(hkl) = \int dr \rho(xyz) e^{2\pi i(hx+ky+lz)}$$

or, in terms of the form factors,

$$F(hkl) = \sum f_i \rho(xyz) e^{2\pi i(hx_i+ky_i+lz_i)}.$$

### 2.3.1 XRD Experimental Conditions

Pressure dependent XRD experiments were executed at the XDS beamline of the Brazilian Synchrotron Laboratory (CNPEM-LNLS) [10]. Hard X-rays of 20 keV in energy were employed in order to overcome the difficulties implied by the use of the pressure cell, that presents small scattering aperture window and strong absorption of lower energy X-rays.

On top of that, the characterization XRD experiments that testify the quality of the samples were carried out at ambient conditions at the Crystallography Laboratory at IFUSP, using a D8 diffractometer by Bruker. These results were already shown in Figure 2.1.

### 2.3.2 Diamond Anvil Cell

The X-ray diffraction experiments were performed for a range of pressures in order to explore the compression properties of the materials and to check upon structural changes that might appear. The experiments thus required the use of a Diamond Anvil Cell (DAC), where the samples are compressed between two diamonds.

The principle is to place between them the gasket, which is basically a sample holder (a small disk with a hole in the center), where the sample and a micrometric ruby sphere are allocated (see Figure 2.3). This ruby is used to constantly monitor pressure inside the DAC, through its fluorescence line excited with a laser and captured by a Raman detector. The hydrostaticity is ensured by immersing the sample in a pressure transmitting medium, which can be a liquid, gas or even solid, depending on the desired pressures to achieve. For this set of experiments, we have used a mixture of 1:4 methanol-ethanol.

The diameter of the diamond culet and the material of the gasket are too dimensioned according to the experimental conditions (pressure and energy range). For instance, the gasket can be stainless steel as employed here, the harder rhenium for higher pressures, or berilium for radial incidence of light, provided this material is transparent to X-rays. As for the culet,



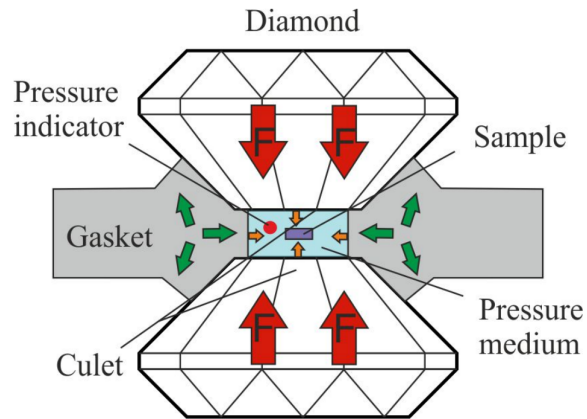


Figure 2.3: Scheme of a Diamond Anvill Cell, with its elements stated on the picture [54].

the smaller the radius, the higher pressures one can achieve, and it is possible to even explore different geometries in order to do that. O'Bannon *et al.* [40] brilliantly show in their review the types and sizes of culet that attend given experimental pressures (see Figure 2.4).

Mounting the DAC can be a very delicate process. Many of the procedures involved are made using a stereomicroscope, given the micrometric scale of the elements being handled. It is necessary to first glue the chosen diamonds to the rock and seat, pieces attached to the cylinder and piston of the cell, respectively. These pieces are responsible for the alignment of the diamonds, both the angular alignment (rock) and in the  $xy$  plane (seat). Also, the material of which they are made is WC, which presents intermediate hardness between diamond and stainless steel, that composes the body of the cell.

Naturally, the next step is to perform the alignment of the diamond culets, critical to applying uniform pressure and ensuring that the diamonds will not break during the experiment. For the same reason, all the pieces of the cell and mainly both diamonds must be neatly cleaned with alcohol or ketone.

Following, the gasket can be indented and drilled. The former process consists of mechanically imprinting the shape of the previously aligned diamonds on the gasket, until its thickness corresponds to  $\sim 1/6$  of the diamonds' culet. It is nonetheless the hole in its center that is actually the sample holder, with diameter  $\sim 1/3$  of the indentation's, and the drilling can be made via electric current or laser.

Finally, the cell is apt to be loaded with sample, ruby and pressure media. Once the DAC is closed, a stainless steel membrane is attached to the piston, and by its careful inflation (with nitrogen or helium gases), the two pieces are pressed against each other.

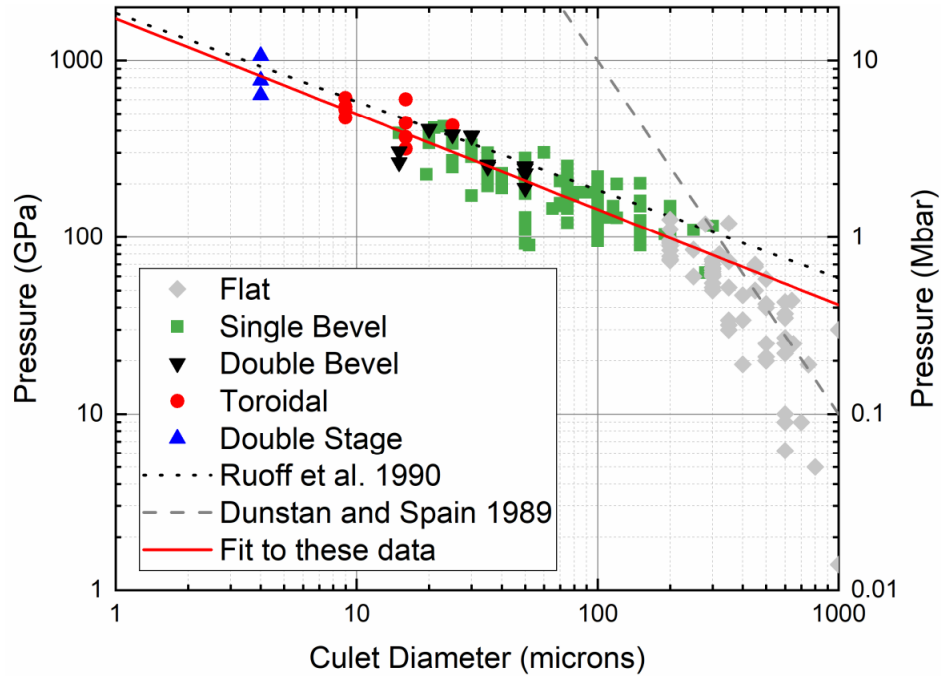


Figure 2.4: Diameter size and geometry of culets to endure given pressures. Picture taken from [40].

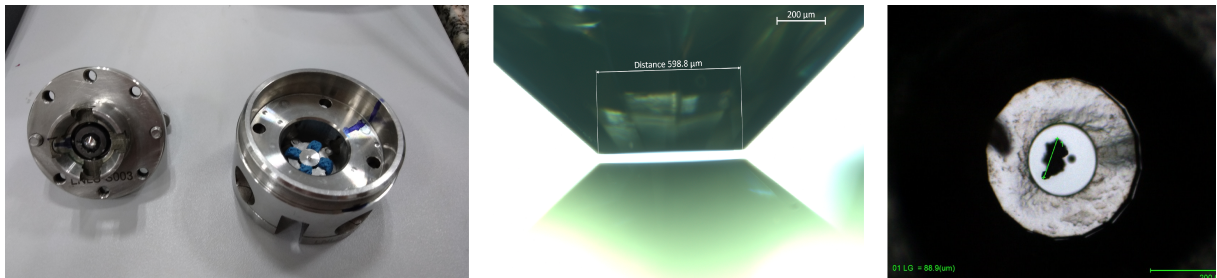


Figure 2.5: DAC mounting process. a) Piston and body of the open pressure cell. b) Alignment of the diamonds. c) Cell loaded with sample and ruby sphere.

## 2.4 Synchrotron Radiation

By solving Maxwell's equations within a multipole expansion, in the relativistic limit, we get the result that accelerating charges produce electromagnetic radiating fields [15]:

$$\vec{E}(\hat{r}, t) = \frac{\mu_0}{4\pi r} [\hat{r} \times (\hat{r} \times \ddot{\vec{p}})]$$

and

$$\vec{B}(\hat{r}, t) = -\frac{\mu_0}{4\pi rc} [\hat{r} \times \ddot{\vec{p}}]$$

where  $\vec{E}$  and  $\vec{B}$  are, of course, the electric and magnetic fields,  $\vec{r}$  is an arbitrary measuring position vector and  $\ddot{\vec{p}}$  stands for the acceleration of the electric dipole for a given charge distribution.

The radiation is characterized by the propagation of energy through space in function of time, and the power of radiation is given by the integration of the Poynting vector:

$$P(r) = \oint \vec{S} \cdot d\vec{a} = \frac{1}{\mu_0} \oint (\vec{E} \times \vec{B}) \cdot d\vec{a} = \frac{\mu_0 \ddot{p}^2}{6\pi c}.$$

Nevertheless, the flow of the radiating energy is transverse to the perpendicular electric and magnetic fields. Bearing this concepts in mind, we can expect that accelerating electric charged particles in a circular trajectory will produce radiation, which propagates in the tangent direction.

This is the very principle of synchrotron light sources, which are a specific type of particle accelerators. By the centripet acceleration of a highly colimated electron beam in a cyclic path, with velocities close to the velocity of light  $c$ , we obtain radiation in a vast range of energies. Higher energies, like X-rays, are the mostly craved, since they interact with matter in smaller scales and thus allow very powerful experiments, impossible to reproduce in more modest laboratories, that provide information on the local and electronic structure of the samples.

In order to achieve high energy and brilliance, the circular tunnel must be kept in vacuum and stable temperature, avoinding collision and trajectory deviation, and its radius must have dozens of metres. In these accelerators, dipole magnets are used to bend the electron trajectory through the influence of their fields, quadrupole magnets for focusing the beam and sextupole magnets controlling non-linear dynamics and correcting chromatic anomalies.

The main elements that constitute the synchrotron accelerator are the electron injector, the

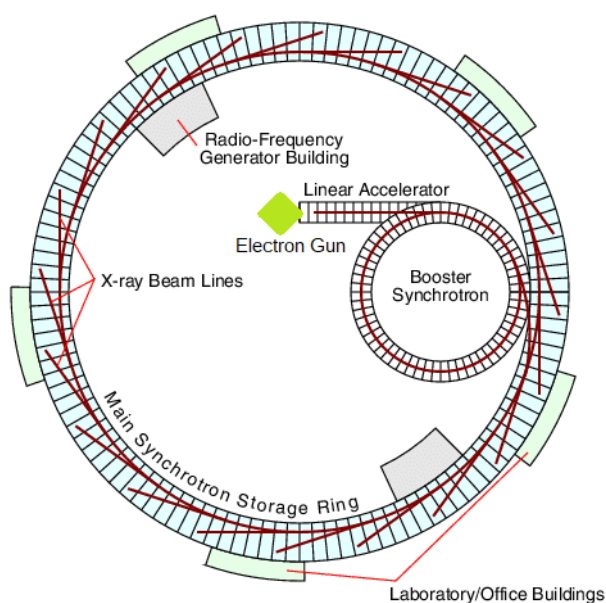


Figure 2.6: Scheme for the synchrotron accelerator. Adapted from < <http://pd.chem.ucl.ac.uk/pdnn/inst2/work.htm> >, access in July/2022 [41].

storage ring and the beamlines, represented in Figure 2.6. The injector is actually the joint of electron gun, linear accelerator and booster synchrotron, and is responsible for inserting the beam of accelerated electrons in the main ring. In the storage ring, they will have their trajectories constantly deflected, causing the centripetal acceleration, and thus emitting radiation. The electrons will also be subject to the other magnets, that guide and focus the beam, and to a radiofrequency system, required to replenish the kinetic energy of the particles. Finally, the beamlines are positioned in tangents around the electron tunnel in order to capture the emitted light, where optical and experimental sets process the radiation according to the techniques to which the beamline is dedicated.

The XAS experiments conducted in this work were performed in the XAFS2 beamline at the LNLS (National Laboratory of Synchrotron Light, from the initials in portuguese). This beamline was focused in spectroscopy experiments for hard X-rays (3.5 – 17 keV), equipped with a 15-element Ge detector and a cryostat [13]. As for the XDS beamline of the same facility, where the XRD experiments were performed, was dedicated to X-ray diffraction and spectroscopy for hard X-rays (5 – 30 keV). It included collimating and focusing mirrors and a double crystal Si monochromator [28].

# Chapter 3

## Results and Discussion

In the following chapter we present the results obtained for the temperature dependent EXAFS experiments, and pressure dependent XRD experiments, discussing the implications to the vibrational and structural properties of the skutterudites. To these, we still add a section on DFT calculations, disclosing the bonding character of the systems and supporting the entire analysis.

### 3.1 EXAFS Analysis and Vibrational Properties

As we have already mentioned, the extended part of the X-ray absorption spectrum reflects the quality of the local structure of a given compound. Figure 3.1 shows the temperature dependent data collected for the samples of  $RFe_4Sb_{12}$  where  $R = K, Ca$  and  $Ba$ , in the range  $6 < T < 300$  K for the  $KFe_4Sb_{12}$  sample and  $10 < T < 300$  K for the  $CaFe_4Sb_{12}$  and  $BaFe_4Sb_{12}$  samples. The Fourier transformed data is plotted in the real space in a range of  $5 \text{ \AA}$  from the absorber. These three materials were selected for a more thorough analysis since they capture the charge and mass effects that the guest atom brings about in the material.

Note that the EXAFS profile of  $R = Ca$  presents less pronounced peaks, mainly in the region between  $3 - 4 \text{ \AA}$ . The fitting statistics for this dataset could be improved by the inclusion of a third cumulant parameter, which is indicative of some degree of anharmonicity in the system [19], but we decided not to include this term in order to keep a standard method regarding the data treatment.

The interpretation of XAS experiments is supported by the multiple scattering theory implemented by the *FEFF* code [2, 43]. The code adopts a local density approximation to construct the photoelectron scattering process of a particle in the neighbouring atoms of the absorber. The

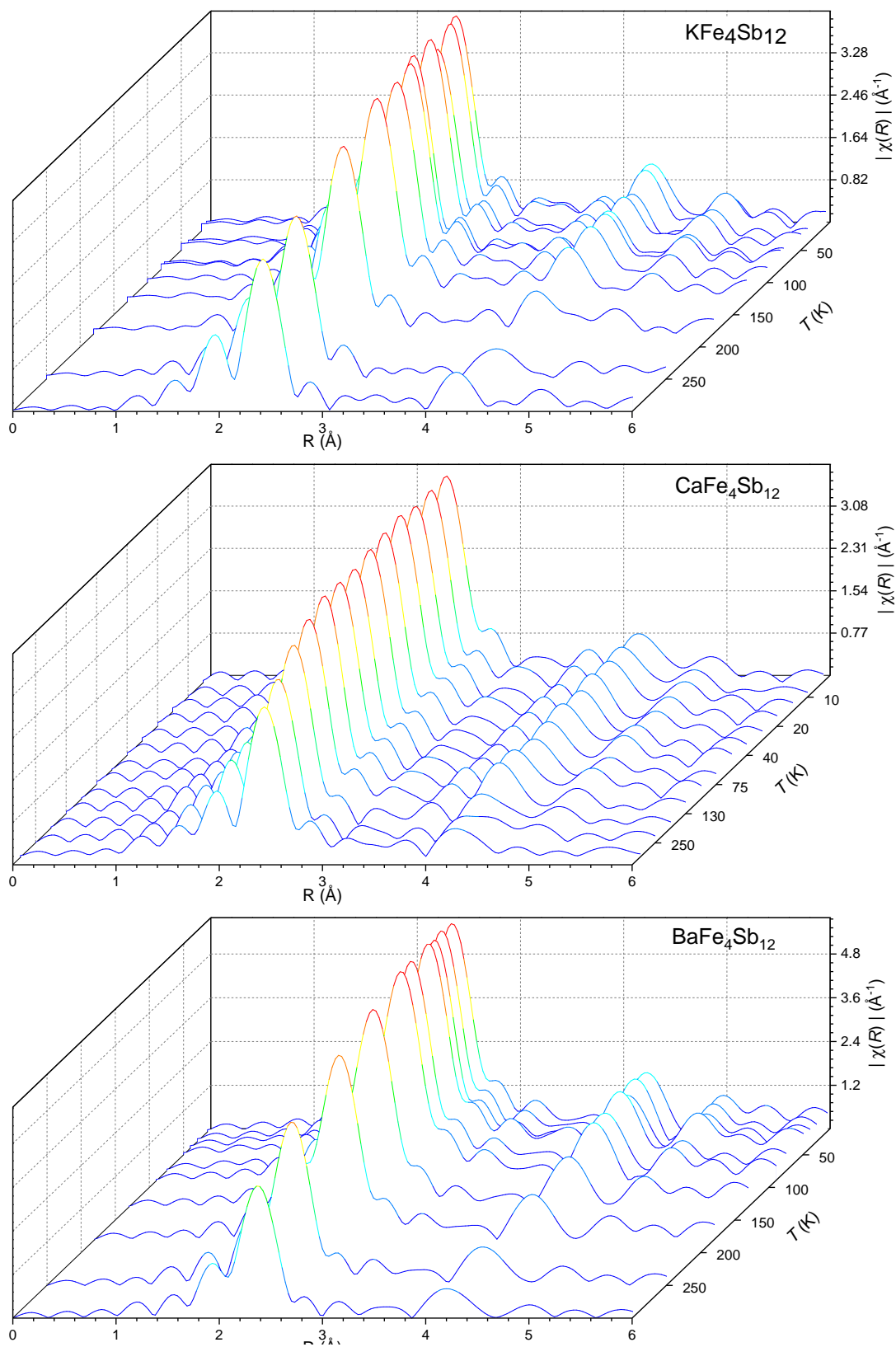


Figure 3.1: Temperature dependent X-ray absorption spectra for the  $R = \text{K}$ ,  $\text{Ca}$  and  $\text{Ba}$  samples.

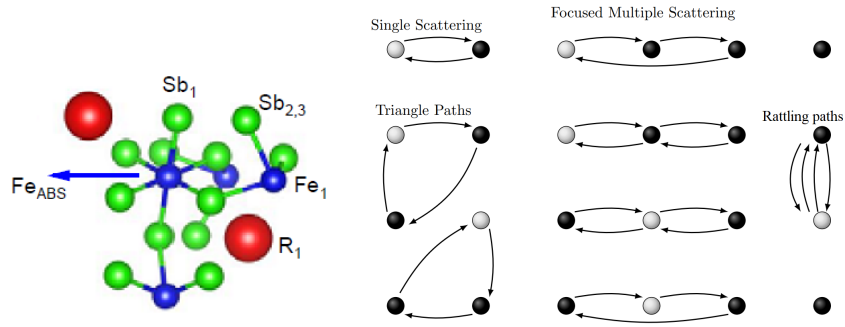


Figure 3.2: a) Local structure scheme of the chemical environment of the Fe absorber atom in the R filled skutterudites. Red spheres represent the  $R$  filler, green spheres the Sb and in blue the Fe atoms, being the absorber indicated in the figure. b) Examples of scattering paths for the photoelectron that may contribute to the EXAFS spectrum (adapted from [39]).

experimental spectra were fitted against these calculations for scattering paths up to  $5 \text{ \AA}$  with the aid of the graphical software Artemis, belonging to the Demeter package of XAS data analysis [42]. Figure 3.2 (a) shows the atoms around the absorbing Fe that were included in the fitting, among single and multiple scattering paths, and examples of these paths can be found in Figure 3.2 (b).

The EXAFS  $S_0^2$  parameter (the path amplitudes) was obtained from *Ab initio* calculations implemented by the *FEFF* 8.4 code, aiming to decrease the number of parameters in the fitting. The *Ab initio* calculations were performed for clusters of 226 atoms, adopting the Hedin-Lundqvist pseudopotential to account for the exchange interaction in a previous work [34]. All the data sets and respective fittings, including the ones for  $R = \text{Na}$  and  $\text{Sr}$  with fewer temperature points, are represented in Figures 3.3, 3.4, 3.5, 3.6 and 3.7. The residual subtraction of data and calculation is shown in green, and we can see the good accuracy of the fitting.

It is through the temperature dependent experiments that we can extract the Debye-Waller (DW) parameters, indicative of the disorder of the system, within the Einstein or Debye model. The former acknowledges both scatterer and absorber as particles connected by an independent quantum spring, whilst the latter considers an effective spring constant regarding the forces between all the atom pairs. In fact, it ascribes the DW parameter to the Debye temperature ( $\theta_D$ ) of the system, reminiscent of the energy of its acoustic phonon. The fundamental difference between both models relies on how the vibrations of the system are treated. That is why we judged the Debye model more appropriate for the paths between Fe and its scatterers, except for the  $R$  filler scatterer, where the scenario of a rather uncoupled rattler is conceivable. In this case, the Einstein model was adopted, containing the static disorder  $\sigma_0^2$  (the low-temperature

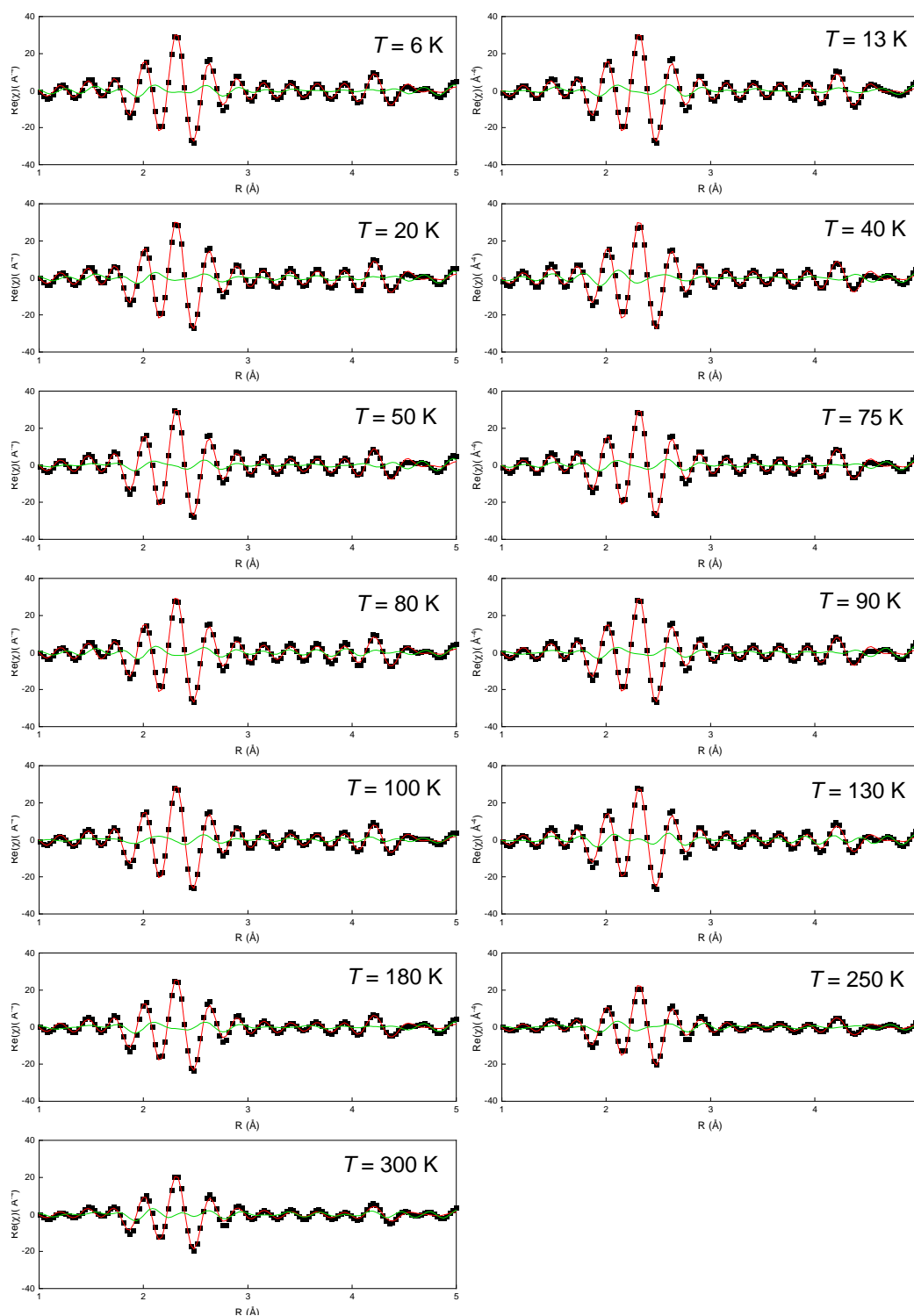


Figure 3.3: Real part of EXAFS for  $R = K$  (black squares) and respective fitting (red lines), for all the temperature dependent spectra collected. The green lines show the subtraction between data and fitting.



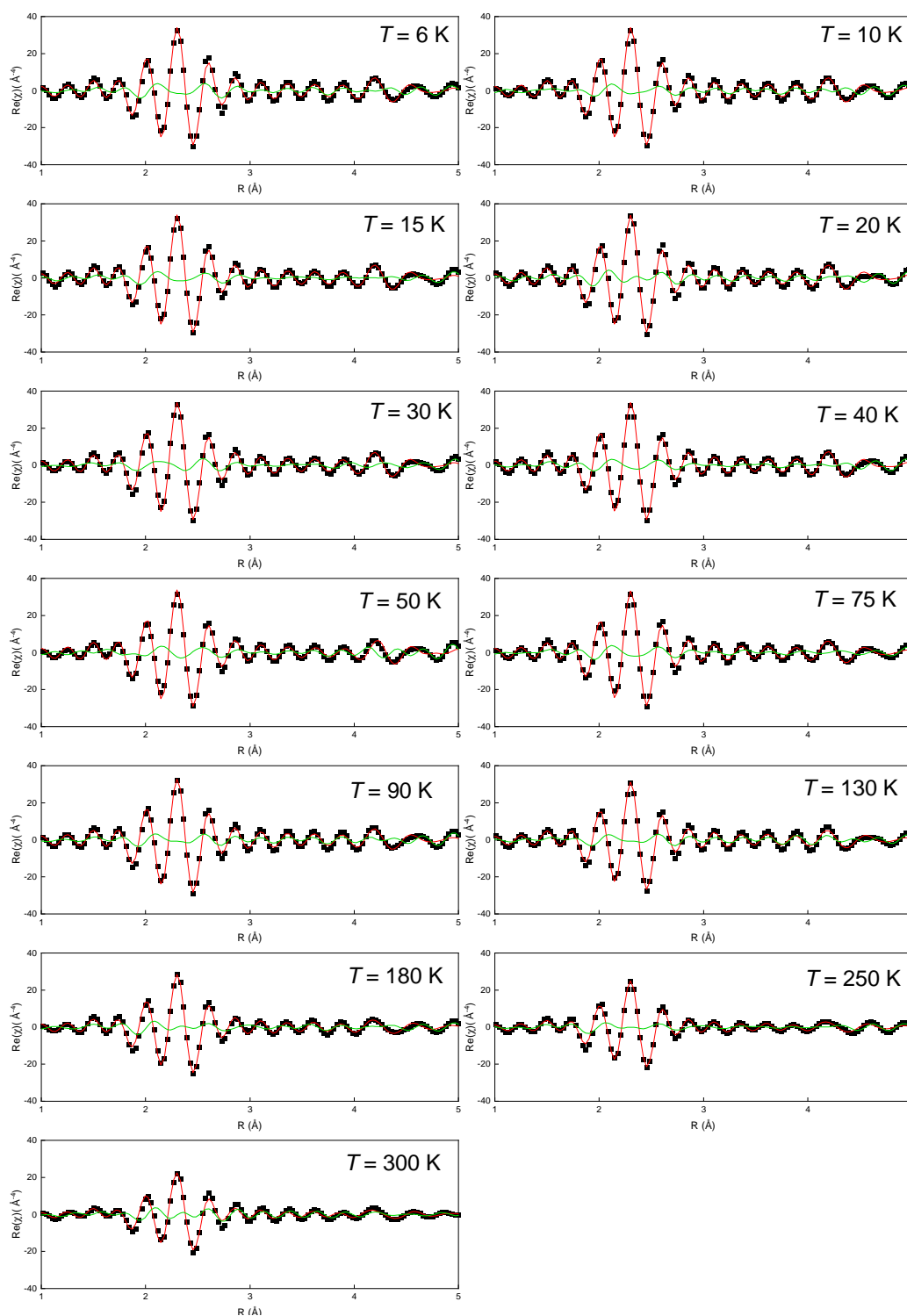


Figure 3.4: Real part of EXAFS for  $R = \text{Ca}$  (black squares) and respective fitting (red lines), for all the temperature dependent spectra collected. The green lines show the subtraction between data and fitting.

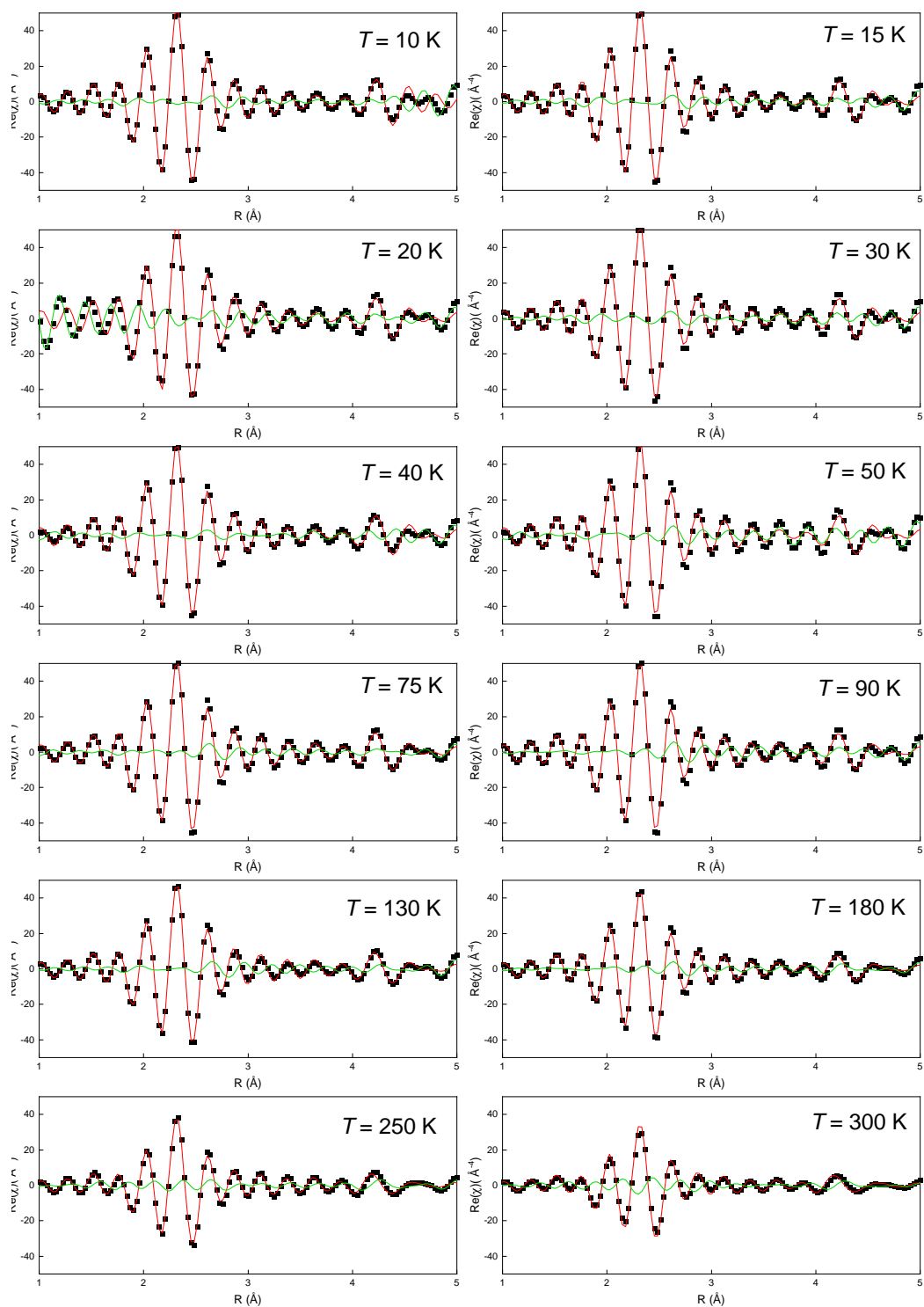


Figure 3.5: Real part of EXAFS for  $R = \text{Ba}$  (black squares) and respective fitting (red lines), for all the temperature dependent spectra collected. The green lines show the subtraction between data and fitting.

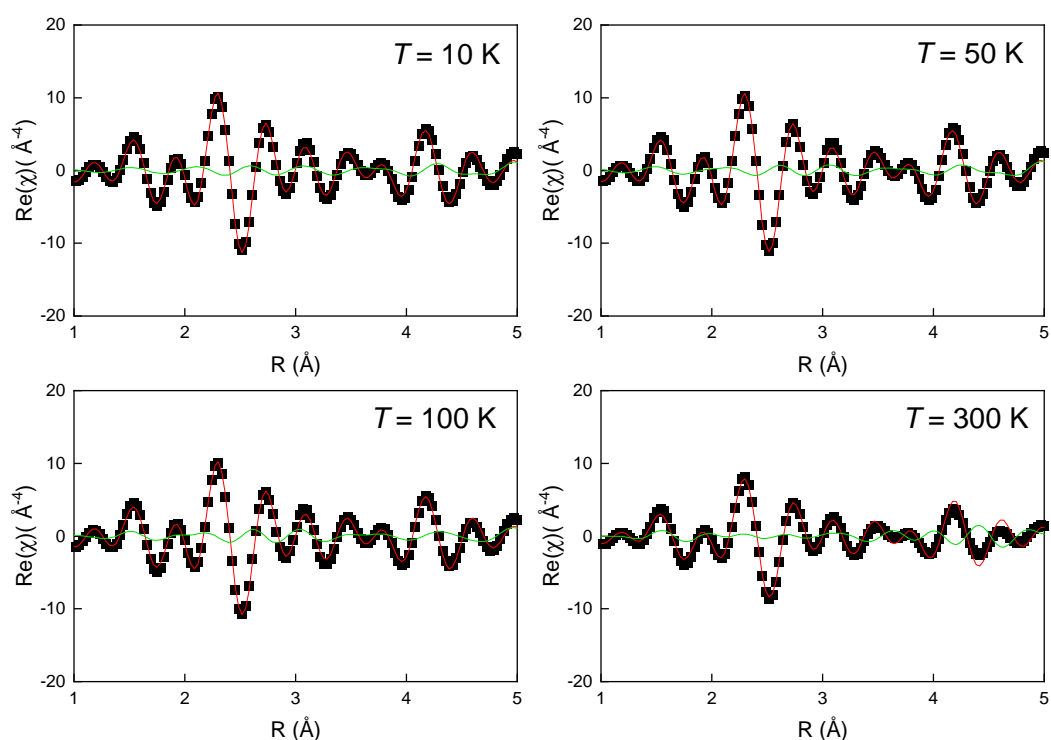


Figure 3.6: Real part of EXAFS for  $R = \text{Na}$  (black squares) and respective fitting (red lines), for all the temperature dependent spectra collected. The green lines show the subtraction between data and fitting.

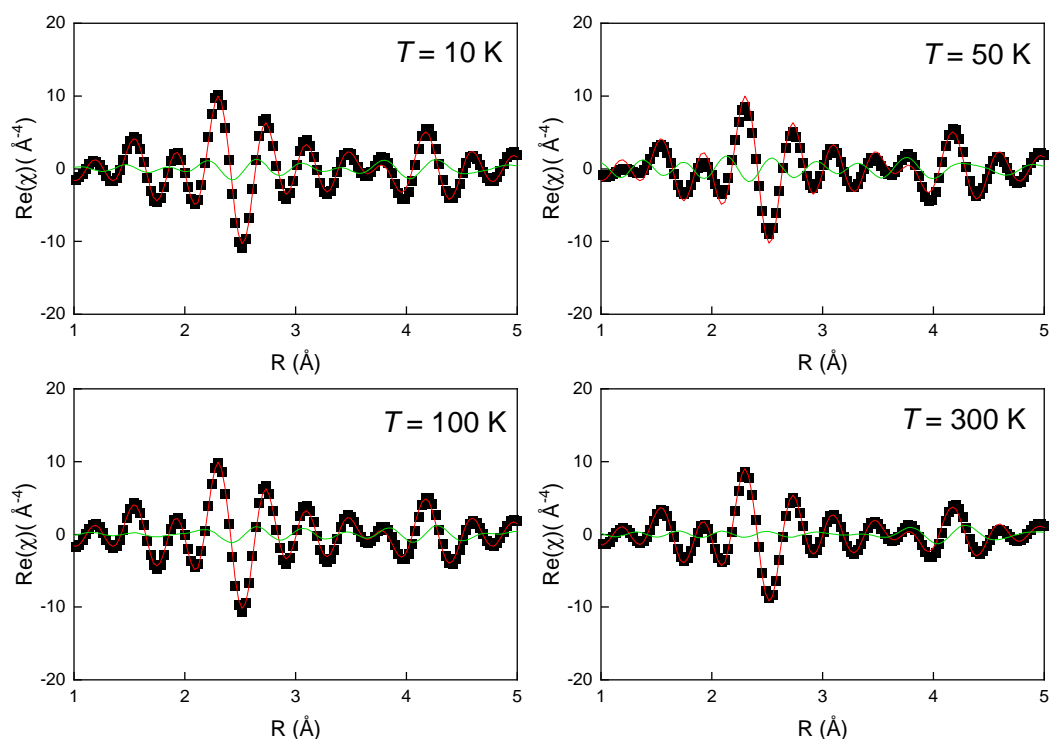


Figure 3.7: Real part of EXAFS for  $R = \text{Sr}$  (black squares) and respective fitting (red lines), for all the temperature dependent spectra collected. The green lines show the subtraction between data and fitting.

values of  $\sigma^2$ ) and  $\theta_E$ , the Einstein temperature. Within this approach, the expression for the DW parameter,  $\sigma_{Fe-R}^2$ , reads [22]:

$$\sigma_{Fe-R}^2(T) = \sigma_{0,Fe-R}^2 + \frac{\hbar^2}{2\mu k_B \theta_E^{Fe-R}} \coth\left(\frac{\theta_E^{Fe-R}}{2T}\right)$$

where  $\mu$  is the  $Fe - R$  pair reduced mass,  $\hbar$  is the reduced Planck's constant and  $k_B$  is Boltzmann's constant. By the same token, one can define the DW parameter for the Debye model as [7]

$$\sigma_{Fe-R}^2(T) = \frac{3\hbar}{2M_R} \int \frac{\omega}{\omega_D^3} C_{ij} \coth\left(\frac{\hbar\omega}{2k_B T}\right) d\omega$$

where  $M_R$  accounts for the mass of the pair of atoms,  $\omega_D$  is the Debye frequency, and  $C_{ij} = 1 - \frac{\sin\gamma}{\gamma}$  with  $\gamma = \frac{k_D \omega r_{ij}}{\omega_D}$  is a motion correlation parameter (since the model implies such coupling between atoms, and where  $k_D$  is the Debye wavenumber).

The  $\sigma_{Fe-Y}^2$  parameters for each single-scattering path of the samples are presented in Figure 3.8, where  $Y$  denotes the scattering element. The same parameter  $\sigma_{Fe-Sb_{2,3}}^2$  was adopted between  $Fe$  and the second and third Sb nearest neighbours,  $Sb_2$  and  $Sb_3$ , since their distance to the absorber is very similar and thus bear basically the same disorder. Here we only present the values of single scattering paths because they are the main contributors to the XAS spectra, and because all the  $\sigma^2$  parameters of multiple-scattering paths included in the fitting process were modeled in function of the single scattering ones.

Observe that the panels of Figure 3.8 do not share the same scale, and that the DW disorder parameter found for the  $Fe - Ba$  path is much smaller than for the corresponding lighter fillers,  $Fe - K$  and  $Fe - Ca$ . At the same time, the DW parameter found for the other paths are of the same magnitude.

The Einstein or Debye temperatures obtained from the model for each path,  $\theta_E^{Fe-R}$  and  $\theta_D^{Fe-Y}$  respectively, reflect the energy scales of the system and are connected to the rigidity of the bondings. The results are compiled in Table 3.1. From the obtained values, one can see that the bonds in the cage are relatively hard, and between Fe and Sb, are almost  $R$  independent, although there seems to be a softening for de  $R = Ca$  case, more pronounced in the  $\theta_E^{Fe-Sb_{2,3}}$ . As for the  $Fe - Fe$  bondings, it is much higher in the case of the  $R = Ba$  compound, fact that should be discussed further ahead (section 3.3) in view of the superior stability of this system. Now, the values for the  $Fe - R$  clearly show that the bonding is weaker between cage and rattler, but

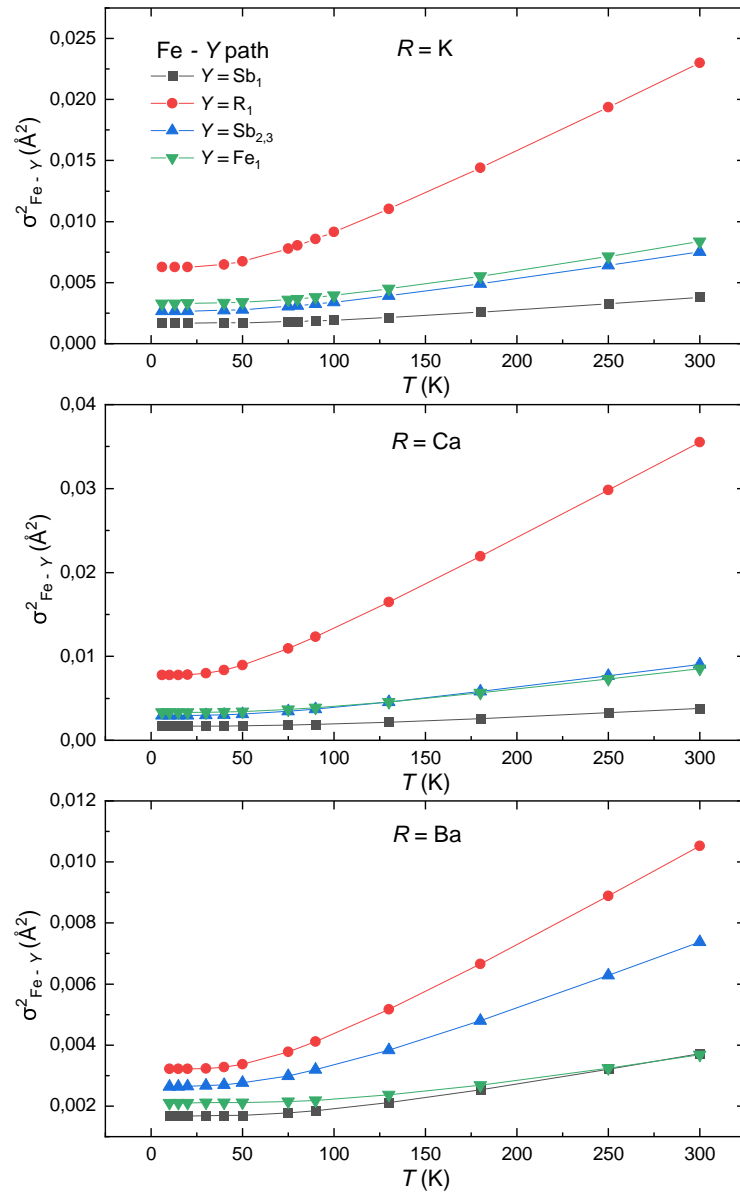


Figure 3.8: Debye-Waller parameters in function of  $T$  for the single-scattering paths of the  $R = \text{K}$ ,  $\text{Ca}$  and  $\text{Ba}$  samples, treated within the Einstein model for the  $\text{Fe}-R$  path and Debye model for the remaining  $\text{Fe}-Y$  scattering paths.

Table 3.1: The  $\theta$  (either  $\theta_D^{R,Fe-Y}$  or  $\theta_E^{Fe-R}$ ) parameters obtained from the analysis of the correlated Debye-Waller parameters.

	$R = K$	$R = Ca$	$R = Ba$
Path	$\theta$ (K)	$\theta$ (K)	$\theta$ (K)
Fe - Sb <sub>1</sub>	422 ± 15	419 ± 14	426 ± 17
Fe - R	168 ± 61	134 ± 51	190 ± 43
Fe - Sb <sub>2,3</sub>	356 ± 26	323 ± 23	360 ± 15
Fe - Fe <sub>1</sub>	395 ± 75	390 ± 77	620 ± 80

Table 3.2:  $K_{eff}$  parameters obtained from the analysis of the correlated Debye-Waller parameters.

	$R = K$	$R = Ca$	$R = Ba$
Path	$K_{eff}$ (eV/Å <sup>2</sup> )	$K_{eff}$ (eV/Å <sup>2</sup> )	$K_{eff}$ (eV/Å <sup>2</sup> )
Fe - Sb <sub>1</sub>	8.13	8.13	8.45
Fe - R	1.15	0.74	2.55
Fe - Sb <sub>2,3</sub>	3.85	3.12	3.92
Fe - Fe <sub>1</sub>	3.56	3.45	9.79

comparing through the materials, the Ba atom seems to be more strongly bounded to the cage.

That brings us to the effective  $\theta$  spring constants associated to these parameters, which can be extracted from the inverse slope of the curves in Figure 3.8 at the high temperature limit, regardless of the model adopted (Einstein or Debye) [6], as

$$K_{eff} = k_B \frac{\Delta T}{\Delta(\sigma^2)}.$$

Since  $K_{eff}^{Fe-Y}$  is proportional to  $\sigma_{Fe-Y}^2$ , their values are not linearly dependent on the obtained  $\theta^{Fe-Y}$  and they also take into account the reduced mass of the atoms being considered. Therefore, this makes of  $K_{eff}$  a better parameter to discuss the vibrational aspects of the system. Their values are computed in Table 3.2.

As one can see, the trends of bonding stiffness discussed above are confirmed, and even put into evidence: the softening of  $Fe - Sb_{2,3}$  bonding, the extremely rigid bonding between  $Fe - Fe$  in the  $R = Ba$  material and the fairly coupled Ba atom to the rest of the structure, with spring constant comparable to the ones between pairs in the cage framework. The latter results are in accordance with those obtained for  $CeRu_4As_{12}$  [7, 22] and  $LaPt_4Ge_{12}$  [9], examples of heavy-filler filled skutterudites, and they shed light on the distinction of the vibrational behaviour for skutterudites filled with heavy-weight guest atoms. We can say that the vibrations of heavy fillers are more strongly related to the vibrations of the cage, while the lighter fillers are relatively

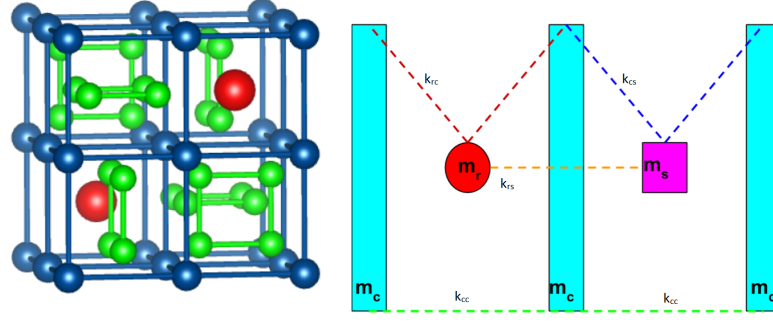


Figure 3.9: a) Representation of the skutterudite unit cell applied to the 1D model for phonon dispersion. In blue, the Fe atoms belonging to the cage, in red, the  $R$  fillers and in green the Sb atoms, forming a square ring that vibrates inside the metallic structure. b) One dimensional model of the skutterudite unit cell, containing three different masses (rattler, square Sb ring and Fe) and four different spring constants, between each pair of vibrating element. Figure adapted from [22].

uncoupled to the rest of the system. This reinforces the rattling picture we had proposed for the filler atom in the case of the light-weighted ones.

It is important, however, to assign that the vibrational dynamics illustrated here concerns not only the mass relation between the  $R$  filler and cage, but also the potential energy of the whole system, as we are dealing with restoring forces in a quantum oscillator [23].

These conclusions lead us to the calculation of the phonon modes involved in the system, as discussed in the next section.

### 3.1.1 Phonon Model

With reference to section 1.3, we can calculate the phonon dispersion based on the effective spring constants involved in the system. Actually, we arbitrate new values from the experimentally acquired ones, respecting the relative strenght of the bondings and the proportions between the assessed materials. For that, it is interesting to picture the skutterudite unit cell in an alternative manner, containing the three vibrating elements *rattler*, with mass  $m_r$ , Sb *square ring*, with mass  $m_s$ , and the Fe atom, represented as  $m_c$  for composing the metallic *cage*. This view of the material is represented in Figure 3.9 (a), and accounts for the square ring as a vibrating element coupled to the filler [22].

As mentioned in section 1.3, the one dimensional model can be based on the one introduced by Keiber *et al.* [22] for analogous skutterudites, where they establish four different spring constants, as pictured in Figure 3.9 (b): between rattler and cage,  $k_{rc}$  which is analogous to the experimental  $K_{eff}^{Fe-R}$ , between two cage atoms,  $k_{cc}$  analogous to  $K_{eff}^{Fe-Fe}$ , between cage and

square ring,  $k_{cs}$  proportional to  $K_{eff}^{Fe-Sb}$  and set in our model to  $1.8 \text{ eV/\AA}^2$  for all the materials, and finally between rattler and square ring,  $k_{rs}$ , that has no parallel in our EXAFS experiments and were thus based on the same work by Keiber [22] for a range of values depicted in Figure 3.10. Also, we have adopted  $k_{cc}^{K,Ca} = 10 \text{ eV/\AA}^2$  and  $k_{cc}^{Ba} = 25 \text{ eV/\AA}^2$ , given the proportion of the experimental values  $K_{eff}^{Ba,Fe-Fe} / K_{eff}^{R,Fe-Fe} \approx 2.8$  for  $R = \text{Ca}$  or  $\text{K}$ . We highlight that the experimental  $K_{eff}$  obtained for each atom pair cannot be directly applied to the model because it accounts for contributions from all surrounding spring constants, so we can only use them as a guidance.

The main aspects that will define the final phonon dispersion extracted from this model are, of course, the mass relation between filler and cage, and the spring constants between them,  $k_{rc}$  for each  $R$  filled material. The suggested results for a few proposed  $k_{rc}$  and  $k_{rs}$  values are shown in Figure 3.10, where the proposed values are indicated.

In the first panel, we see the phonon modes attributed to both the light-filler materials, namely  $R = \text{K}$  and  $\text{Ca}$ , where the difference in mass relation between cation and cage is negligible, and the spring constant  $k_{rc}$  would be equally small for both of them. We can see that it leads to a small gap between the acoustic mode (in red) and the first optical mode (in green), and a very flat second mode (in orange). The latter means a heavy, non dispersive phonon mode, or else, a mode with group velocity near zero for many values of  $q$ ! This localized phonon mode is in total accordance with the Einstein oscillator scenario, where the guest atom is seen as a rattler inside the cage. It is important to underline, however, that the vibrational modes are not entirely independent from the host cage [24], and the low thermal conductivity  $\kappa_{latt}$  must derive from the presence of low-velocity phonons. These are capable of scattering other phonons through the lattice, as one possible mechanism, but notice that the acoustic mode is also little dispersive, which supports low  $\kappa_{latt}$  [11]. Moreover, given the ratio of the experimental values  $K_{eff}^{Fe-Ca} / K_{eff}^{Fe-K} \approx 2/3$ , we suggest that Figures 3.10  $a - c$  refer to the  $R = \text{K}$  material and Figures 3.10  $g - i$  refer to the  $R = \text{Ca}$  material. Finally, we can see that for stronger values of  $k_{rs}$ , the second mode becomes more dispersive and assumes higher values of frequency, interacting with the third phonon mode (in blue) to avoid crossing.

As for the second panel, referring to the heavy filler case ( $R = \text{Ba}$ ), we see a smaller gap between the first optical mode and the acoustic mode, resultant of a smaller ratio between masses of filler and cage. The larger spring constant  $k_{cc}$  implicates a narrower region wherein the second optical mode is flat, indicative of a less localized phonon, which means that the



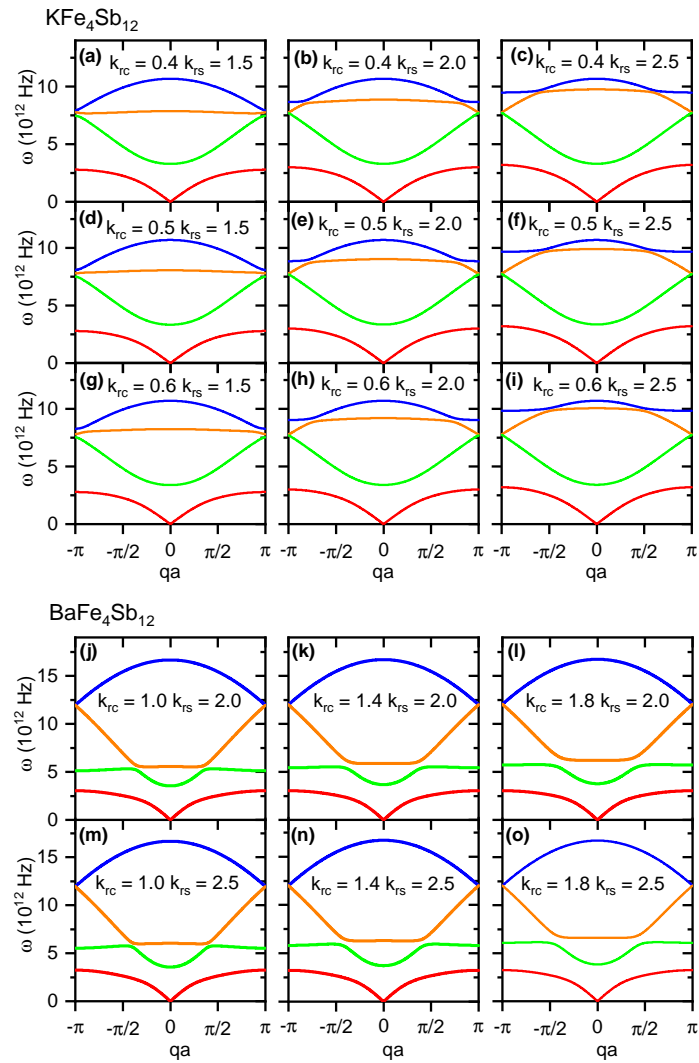


Figure 3.10: Phonon dispersion obtained from the 1D model for vibrational behaviour of the filled skutterudites. The first panel refers to the light cation filled materials ( $R = \text{K}, \text{Ca}$ ), while the second one represents the dispersion obtained for the heavy filler ( $R = \text{Ba}$ ) filled material.

filler's vibrational behaviour is comparatively coupled to the cage's. Here, the second mode is instead interacting with the first mode, causing it to flatten for  $q > |\frac{\pi}{2}|$ . The third mode is now non-interactive, and its frequency was considerably raised due to the high  $k_{cc}$ . As we have mentioned, despite the dispersion of the optical modes changed reasonably from the light-filled material to the heavy-filled one, we see a fairly dispersionless acoustic mode in both of them, which is determinant to a low lattice thermal conductivity, as we have seen in section 1.2 [11].

Ultimately, we clearly see that for the light fillers filled materials ( $R = K$  and  $Ca$ ), where the spring constants are also weaker, there is the presence of an Einstein phonon mode, qualified for participating in scattering mechanisms. At the same time, the heavy filler filled material, with rather strongly coupled guest atom, show more dispersive phonon modes, implying that rattling can be associated to the bonding properties of the system. These results are in accordance with the expected [51].

## 3.2 XRD Analysis and Elastic Properties

The XRD experiments were performed under varied pressures, at the CNPEM-LNLS synchrotron facility, aiming to probe the elastic behaviour of the materials. The results after background removal are presented in Figure 3.11, where we have also plotted in red the calculated peak profile, taking into account the reduction in lattice parameter as an effect of pressure. The data were analyzed using the open software GSAS-II [52].

Contrary to the previous XRD experiments performed at room conditions for sample characterization, the Rietveld refinement for this data set was unattainable, given that the high pressure severely spoils the quality of the diffractograms. Even so, the position of the peaks is considered reliable to obtain other information about the crystal, such as the lattice parameters.

There is a clear broadening of the peaks with increasing pressure, that can be assigned to a partial amorphization of the sample, or at least an increase in the structural disorder of the system. It starts around 12 GPa for the alkali filled materials ( $R = Na, K$ ), but seems to resist at least until  $\sim 13.5$  GPa for the alkaline earth ones ( $R = Ca, Sr, Ba$ ). For the Ba compound, there are distinguishable peaks up to 18.1 GPa! This relative structure stabilization for the 2A-filled skutterudites can be assigned to the extra positive charge that the cation donates to the cage structure [17] and will also be further discussed in section 3.3.

Admittedly, we see the emergence of new peaks for the  $R = K, Sr$  and  $Ba$  compounds starting

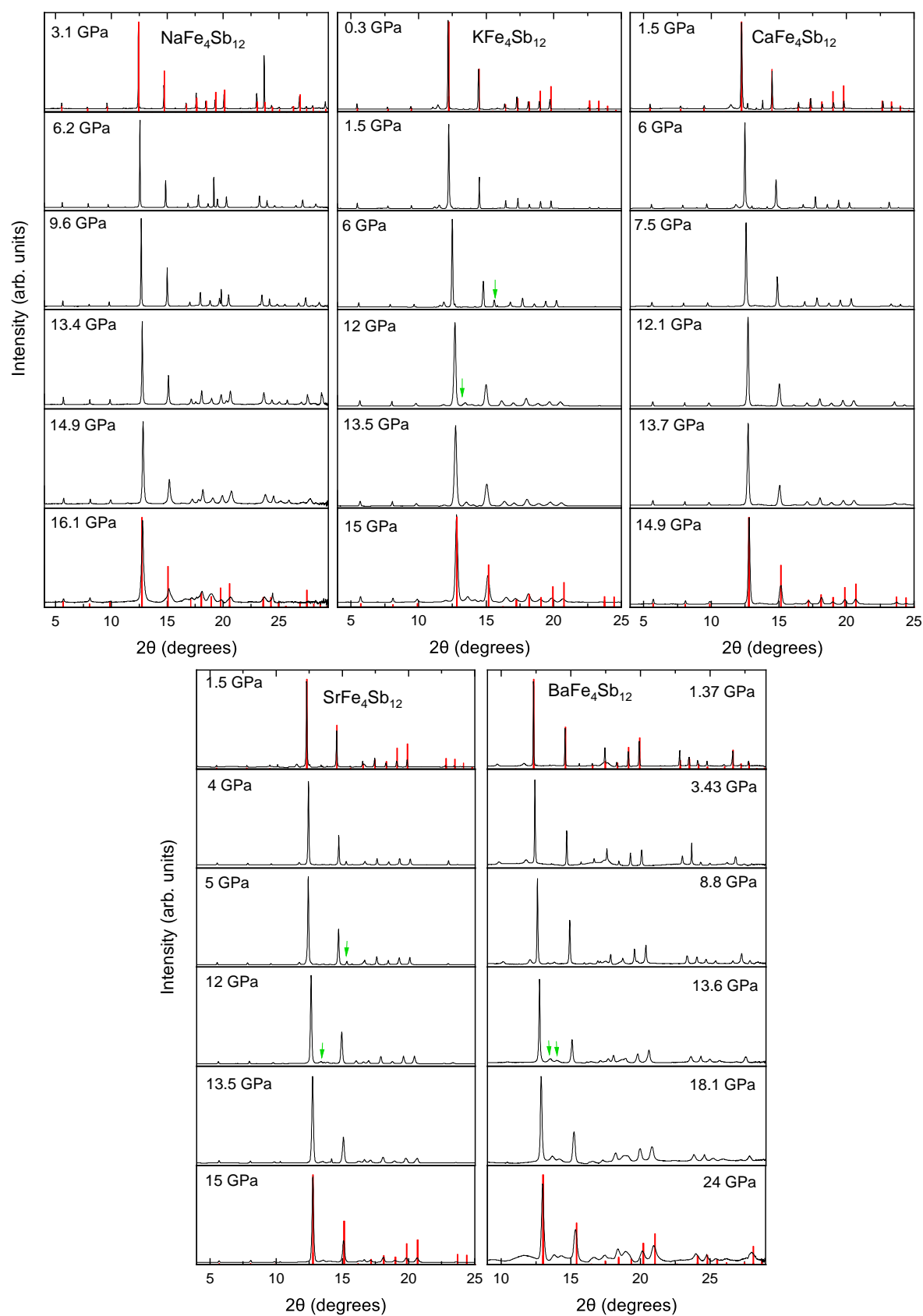


Figure 3.11: Pressure dependent diffractograms for all the skutterudite samples. In red are highlighted the Bragg diffraction peaks for the corresponding material and pressure.

Table 3.3: Unit cell volume at room conditions and bulk modulus, extracted from the Birch-Murnaghan model for all  $RFe_4Sb_{12}$  samples.

$R =$	Na	K	Ca	Sr	Ba
$V_0(\text{\AA}^3)$	$768.3 \pm 0.7$	$787.8 \pm 0.2$	$778.7 \pm 0.5$	$777.6 \pm 0.5$	$772.0 \pm 0.3$
$B_0(\text{GPa})$	$94 \pm 0.7$	$77 \pm 0.5$	$87 \pm 0.6$	$91 \pm 0.6$	$99 \pm 0.3$

from  $P \sim 5$  GPa, indicated by green arrows. These are attributed to the appearance or stabilization of secondary phases in the sample at higher pressures, like the residual Sb or binary compounds, and not to a poor background subtraction. In order to ascertain this, we show the raw data plus background in the left panels of Figure 3.12, and again the diffractograms after background subtraction in the right panels for all the samples at the pressure of  $\sim 13.5$  GPa. We point out that the experimental data were collected both in ascending and descending pressures, and at the occasion of returning to room conditions these peaks ceased to exist once again.

By fitting the peak positions given by the XRD experiment, we can extract the lattice parameter of the cubic unit cell and thus calculate its volume in function of pressure. These results are shown in Figure 3.13 (a), and in Figure 3.13 (c) we see the fittings to the Birch-Murnaghan model (referring to section 1.5), that instead returns the dependence of pressure in function of volume. We have kept the bulk modulus derivative  $B'_0 = 4$  in a simplified version of the model, as has been adopted before [44, 47] for other skutterudites and seeing that it resulted in a more accurate fit. This is allowed for this specific range of pressure, which is low in comparison to the bulk moduli values, and only for cubic symmetry.

The Birch-Murnaghan model is applied here so as to obtain the bulk moduli of the materials, consequently reflecting their compressibility  $\beta$ , that has been drawn in Figure 3.13 (d). The parameters provided from the fitting are shown in Table 3.3.

The  $V_0$  is here recaptured from the experimental obtained values, with less than 1% in difference, which indicates the suitability of the model. The  $B_0$  parameters, expressing the rigidity of the unit cell (better yet, the rigidity of the cage), are in accordance with calculated ones for the alkaline earth materials [25], but in the mentioned work it is nearly  $R$  independent, around 80 GPa, whilst our results range from 87 to 99 GPa for the alkaline earth materials. These values are also consistent with the ones obtained for  $CeFe_4Sb_{12}$  [29].

The first hypothesis raised was that the compressibility parameter  $\beta$  would be connected to the size of the filling atom inside the cage: the larger the cation radius, the less compressible the material would be. In order to further investigate that, we calculated a qualitative parameter,

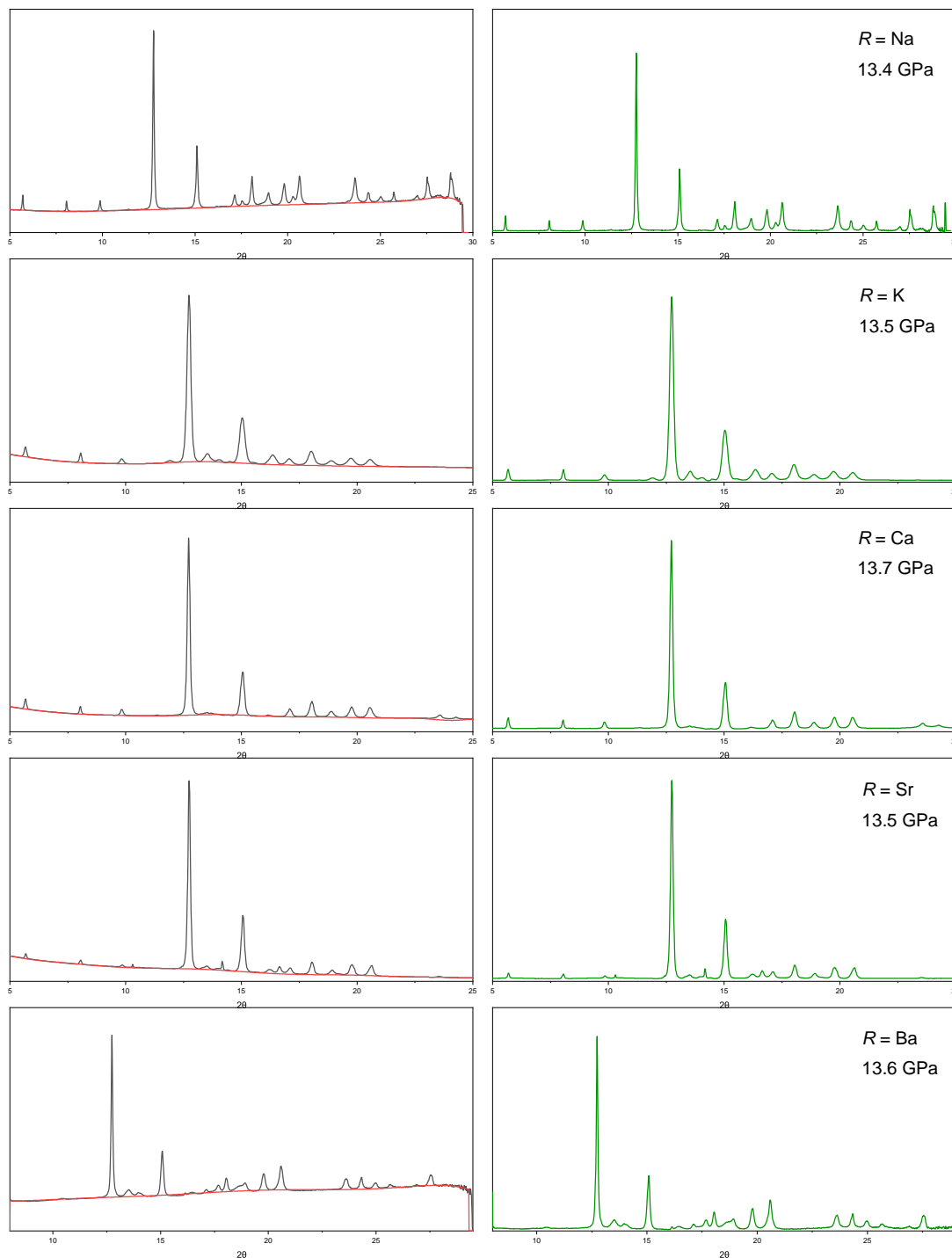


Figure 3.12: Background removal procedure for XRD data at higher pressures.

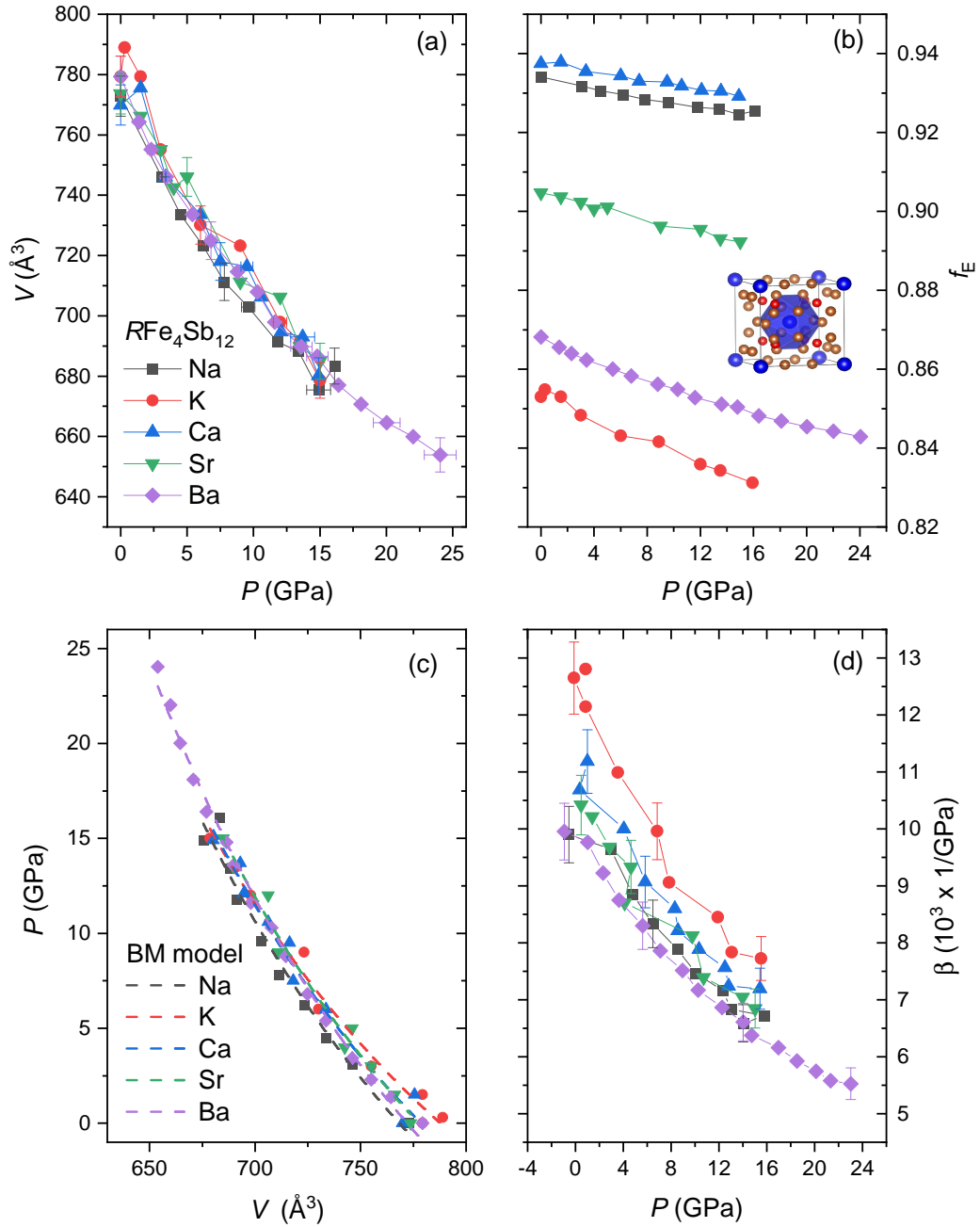


Figure 3.13: (a) The unit cell volume  $V$  as function of  $P$ . (b) The cage empty volume fraction  $f_E$  as a function of  $P$ . (c) The  $P$  as a function of  $V$  data and their respective fittings to the Birch-Murnaghan model. (d) The compressibility  $\beta$  as a function of  $P$  for all samples.

namely the cage's empty volume fraction, given by  $f_E = 1 - \frac{V_R}{V_C}$ , where  $V_R$  is the  $R$  filler cationic volume and  $V_C$  is the Sb icosahedral cage inner volume, represented on the inset of Figure 3.13 (b). The  $P$  dependent  $V_C$  were calculated with support of the Vesta software [33].

With Figure 3.13 (b) in mind, showing the  $f_E$  parameter, one would expect to find the same tendency for the compressibility  $\beta$  in panel (d). However, this order is not obeyed across the series, and there is even an inversion of this trend for the alkali filled materials: the K sample, despite having the smallest empty volume fraction, has proven to be the most compressible compound!

This intriguing result was a turning point to disregard the geometrical  $f_E$  parameter as the responsible for the elastic properties of skutterudites, and turned our attention to the relevant bonding properties of the materials. Considering that Sr and Ba atoms present virtual  $d$  orbitals relatively extended in space and also accessible energetically, as they lie close to the Fermi surface, we wondered if they were taking part in the filler-cage bonding, which would of course mean some degree of covalent character, as has been proposed before for  $LaFe_4Sb_{12}$  [16]. Therefore, we explore this hypothesis through quantum chemistry calculations in the next section.

### 3.3 DFT Calculations and Bonding Properties

Through the aforementioned DFT calculations (see section 1.4), we could probe the bonding character between the cation and the cage, across the alkaline earth series. They were performed in collaboration with other members of the group and its results were largely discussed by all members collaborating in this project. Nevertheless, here we restrict the description of these calculations to satisfy the understanding of bonding properties, leaving out unnecessary details.

Our results show that there is a high contribution of the  $4d$  and  $5d$  atomic orbitals (AOs), for Sr and Ba atoms respectively, in the system's molecular orbital (MO), defining the  $Fe_8Sb_{36} - R^{2+}$  units as honorary complexes. The prevailing bonding to the cage system is, as expected due to electron affinity, with the Sb  $5p$  orbitals. Nonetheless, the contribution from the Ca  $3d$  states in this bonding is negligible, and its main contribution comes from Ca populated  $3p$  states. The final orbital composition analysis was performed adopting the Ros-Schuit partition method via the Multifwn program [30].

In table 3.4, we put into evidence the main character of the cation AO contribution to the

MO, for energies bordering the Fermi surface, region responsible for chemical bonding. The electronic states related to the filler-cage bonding were classified according to the irreducible representations of the filler symmetry point group  $T_h$  [50].

Table 3.4: The highest filler derived superposing AOs to the formation of the MOs in the filler-cage bonding. The nature of the AOs and the symmetry character of the MOs are indicated.

		Room Pressure		$\sim 13.6$ GPa	
$R$	AOs character	Orbital Cont. (%)	$E - E_F$ (eV)	Orbital Cont. (%)	$E - E_F$ (eV)
Ca	$3p_x (t_u)$	30.77	-3.23	30.82	-3.46
Sr	$4d_{xy}, 4d_{xz}, 4d_{yz} (t_g)$	11.84	-1.70	15.37	-1.82
Ba	$5d_{xy}, 5d_{xz}, 5d_{yz} (t_g)$	19.54	-1.60	28.00	-1.68

As there are several combinations for all AOs involved in the filler-cage bonding, a better inspection is made by plotting the orbital and element specific contribution to the Density of States (DOS) and the Overlap Population Density of States (OPDOS). The latter gives the amount of superposition between orbitals (in green) in Figure 3.14, where the main orbital presence is apparent. We focus our analysis on these highest contributing MOs.

Calculations were performed both for room pressure and higher pressure, about 13.6 GPa, for a better discussion of the experimental results. The main difference in the input is the reduced cage volume, which was set according to the experimentally obtained lattice parameters. From the values in table 3.4, one can establish that the contribution of the virtual  $d$  orbitals for  $R = \text{Sr}$  and  $\text{Ba}$  are indeed significant to the MO conformation. What is more, we see for these fillers an indisputable enhancement of the  $d$  character with applied pressure, particularly to the  $\text{Ba}$  case, with an increase of 43%. This means that pressure is acting as a bonding stabilizing parameter, which causes the interatomic distances to contract and thus turning the material even more rigid.

This result not only explains the hardness, expressed by the bulk modulus, of alkaline earth filled skutterudites, but also the relative stability of their structure under pressure, as pointed in the occasion of the XRD analysis. Moreover, it justifies the stronger spring constant  $K_{eff}^{Fe-Ba}$  obtained from the EXAFS experiments and also the outstanding large  $K_{eff}^{Fe-Fe}$  found for the  $\text{Ba}$  compound, given the stark stabilization that the  $d$  orbitals promote in the system as a hole. Conversely, the same effect is not expected for the alkali filled cases, since they present very localized  $p$  orbitals, either bonding or antibonding, in the vicinity of the Fermi energy. Even so, we can firmly state that the  $f_E$  is not an ideal parameter to forecast elastic behaviour, and that such features are instead connected to specific bonding properties of each material.

The contour plots of the aforementioned MOs are depicted in Figure 3.15. The left panels



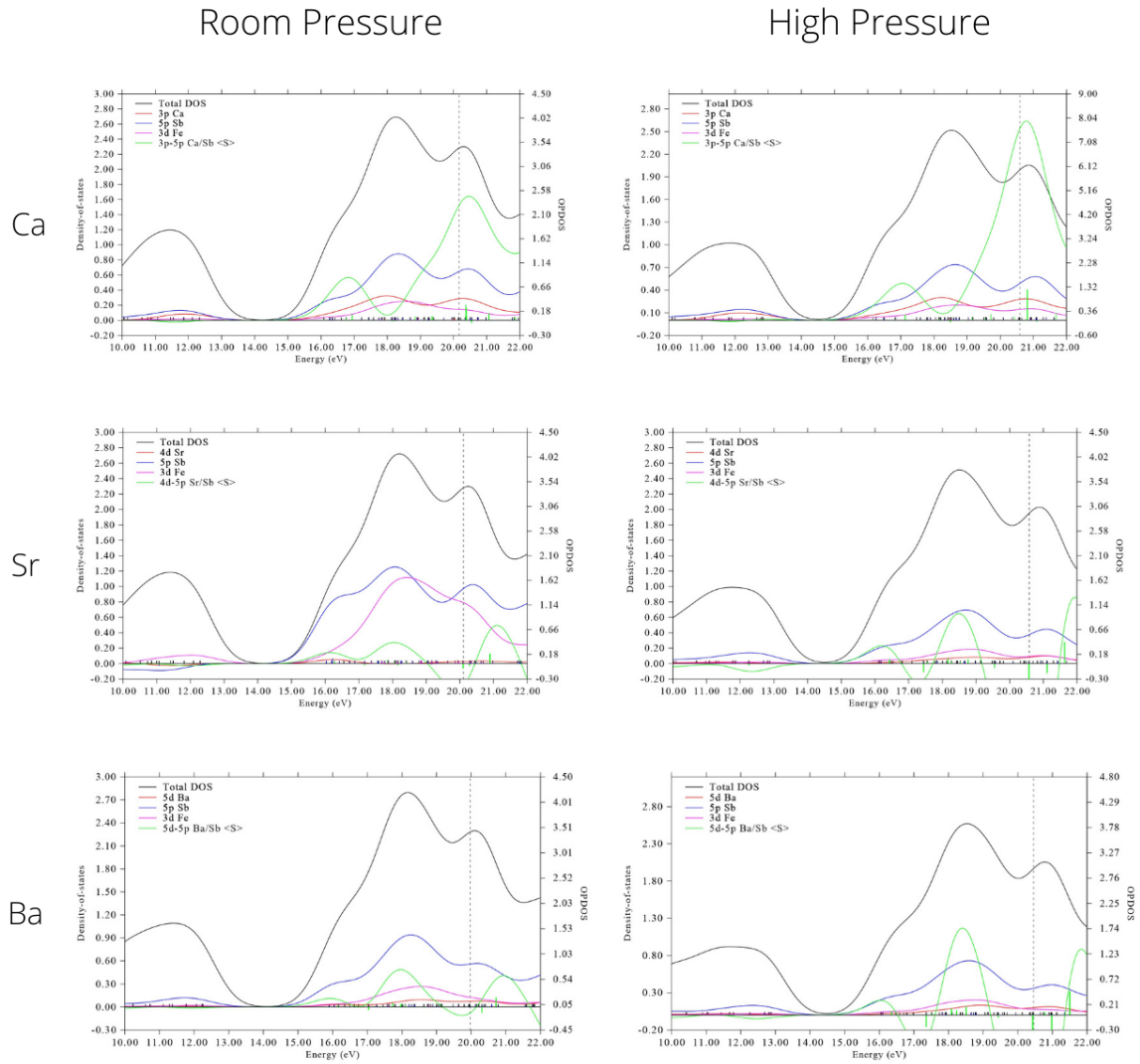


Figure 3.14: Total DOS and OPDOS for the AOs in the vicinity of  $E_F$  taking part in the Ca  $3p$ - $5p$  Sb, Sr  $4d$ - $5p$  Sb and Ba  $5d$ - $5p$  Sr bonding MOs. In each panel, the left axis describes the DOS for all orbitals while the right axis shows the OPDOS.

show the calculated data for room pressure and the panels in the right for high pressures. In the pictures, the  $R$  filler is centered and it gets clear the strong  $d$  character of MOs for Sr and Ba materials, with well defined four lobes of  $d_{xy}$  orbitals, as much as is evident the  $p$  character for the Ca filled skutterudite, with two lobes (the attentive reader will be aware of the presence of  $n - 1$  nodes for a  $np$  or  $nd$  orbital).

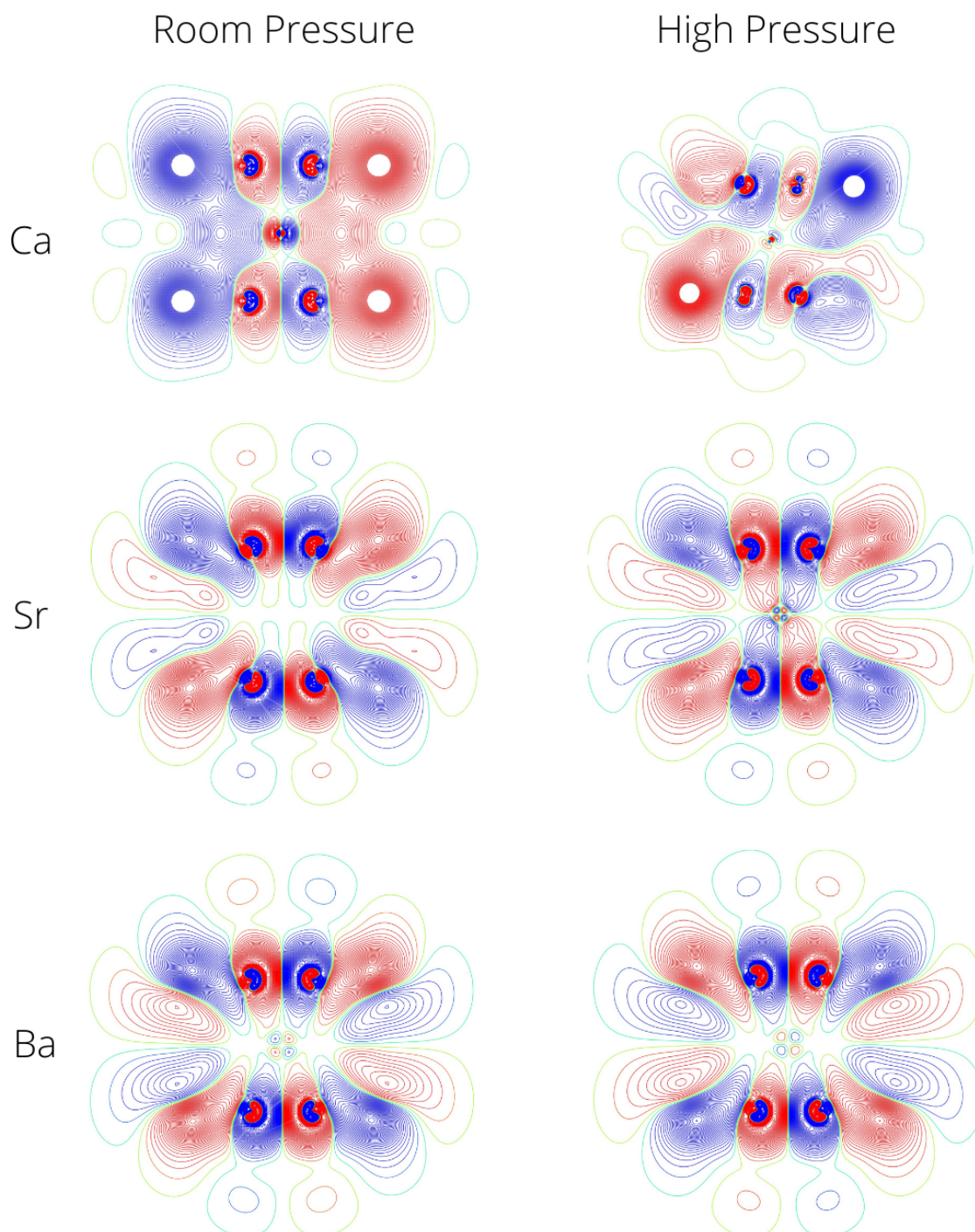


Figure 3.15: Contour plots for the MOs describing the filler-cage bonding in the  $(x, y)$  plane in the cases of the Ca, Sr and Ba filled materials as indicated, for low and high pressures. The figures are formed by 120 contours in the isovalue interval indicated in the color scale in the left side of the figure. Ligand Orbitals are plotted via the Gabedit program [1].

# Chapter 4

## Summary and Conclusions

Aiming to obtain a thorough understanding of the  $R\text{Fe}_4\text{Sb}_{12}$  ( $R = \text{Na}, \text{K}, \text{Ca}, \text{Sr}$  and  $\text{Ba}$ ) skutterudites' vibrational and structural properties, we have performed respectively temperature dependent EXAFS and pressure dependent XRD experiments.

Using the Debye-Waller parameters obtained in the EXAFS analysis, it was possible to extract the effective spring constants involved in the system. At this point it was already clear that the light-weight filler atoms beared a rather uncoupled relation to the cage framework, suggesting an independent vibrational dynamics, reminiscent of the Einstein oscillator scenario. Meanwhile, the heavy-filler ( $R = \text{Ba}$ ) material presented a much harder spring constant between filler and cage atoms, indicating that their vibrations would be relatively coupled. This strenghtening of the bonds could also be responsible for the strong spring constant between atoms of the cage.

By reflecting these results to an 1D newtonian model, we were able to draw a qualitative picture of the phonon dispersion for the vibrating elements of the system. We found a very flat optical phonon mode for light filler materials, typical of a rattling scenario, which possibly scatter phonons propagating throughout the lattice thus reducing the thermal conduction of the material. In comparison, the heavy filler material presented more dispersive phonon modes, indicating that the rattling picture does not describe well this particular system.

As regards the elastic properties of the skutterudites, the XRD experiments showed an increasing disorder of the systems with applied pressure, marked by broadening of Bragg peaks, mainly for the alkali filled materials. This implies a comparative stabilization of the alkaline earth materials, stemming from the extra positive charge that they insert in the structure.

From these results, we derived the bulk modulus through the fitting to the Birch-Murnaghan thermodynamic equation of estate, and consequently could calculate the compressibility parameter for each  $R$  filled skutterudite, in increasing order:  $\beta_{\text{Ba}} < \beta_{\text{Na}} < \beta_{\text{Sr}} < \beta_{\text{Ca}} < \beta_{\text{K}}$ . This trend

contempted the logic of proportion between compressibility and fraction of empty volume in the cell, motivating the investigation of the bonding properties of the system.

Accordingly, we have performed DFT calculations to unveil the character of the main  $R$  atomic orbitals contributing in the net molecular orbital of the system for the alkaline earth materials. As expected, we found a strong character of the virtual  $d$  orbitals participating in the bonding between rattler and cage for the  $R = \text{Sr}$  and  $\text{Ba}$  cases, and almost none for the  $\text{Ca}$  one. This implied that these orbitals not only participate in the bonding, but also enhance the stabilization of the structure, justifying the strong  $K_{eff}$  found for the  $\text{Ba}$  skutterudite and the accomplished resistance to pressure as seen from the XRD experiments for the alkaline earth materials. Furthermore, it is evident that a simple geometrical parameter is insufficient to explaining the elastic behaviour of materials, which are instead connected to specific bonding properties.

On the whole, the vibrational, elastic and bonding properties of the  $R\text{Fe}_4\text{Sb}_{12}$  skutterudites were extensively studied. This work disclosed the mechanisms responsible for their favourable thermoelectricity, related to the phonon modes of the system, and also the chemistry behind the structure stabilization, which dictates their elastic properties. These are intimately related to the choice of the  $R$  filler atom, which presents specific bonding conditions with respect to the rest of the cage framework.

In this sense, it has been proposed by Yang [55] that the insertion of more than one filler species in the skutterudite structure would result in better thermoelectric properties, due to the presence of multiple localized phonon modes causing the scattering of other phonons. Despite that in the mentioned work the suggestion was to mix atoms from different chemical groups in order to introduce different resonant frequencies, we further propose that the mixing of light and heavy fillers would suffice for this purpose. Thence, broadly speaking, our results can be extended to studies concerning similar systems, and even provide the resources to guide the design of new materials.

# Bibliography

- [1] Abdul-Rahman Allouche. Gabedit-a graphical user interface for computational chemistry softwares. *JOURNAL OF COMPUTATIONAL CHEMISTRY*, 32(1):174–182, JAN 15 2011.
- [2] A. L. Ankudinov, B. Ravel, J. J. Rehr, and S. D. Conradson. Real-space multiple-scattering calculation and interpretation of x-ray-absorption near-edge structure. *Physical Review B*, 58(12):7565–7576, September 1998.
- [3] Dinesh K. Aswal, Ranita Basu, and Ajay Singh. Key issues in development of thermoelectric power generators: High figure-of-merit materials and their highly conducting interfaces with metallic interconnects. *Energy Conversion and Management*, 114:50–67, 2016.
- [4] Davide Beretta, Neophytos Neophytou, James M. Hodges, Mercouri G. Kanatzidis, Dario Narducci, Marisol Martin- Gonzalez, Matt Beekman, Benjamin Balke, Giacomo Cerretti, Wolfgang Tremel, Alexandra Zevalkink, Anna I. Hofmann, Christian MÄCeller, Bernhard DÄ¶rling, Mariano Campoy-Quiles, and Mario Caironi. Thermoelectrics: From history, a window to the future. *Materials Science and Engineering: R: Reports*, 138:100501, 2019.
- [5] Francis Birch. Finite Elastic Strain of Cubic Crystals. *Physical Review*, 71(11):809–824, June 1947.
- [6] F. Bridges, B. Car, L. Sutton, M. Hoffman-Stapleton, T. Keiber, R. E. Baumbach, M. B. Maple, Z. Henkie, and R. Wawryk. Complex vibrations in arsenide skutterudites and oxyskutterudites. *Physical Review B*, 91(1):014109, January 2015.
- [7] Frank Bridges. The local structure of skutterudites: A view from inside the unit cell. *Modern Physics Letters B*, 30(5):1630001, February 2016.
- [8] Kieron Burke and Lucas O Wagner. Dft in a nutshell. *International Journal of Quantum Chemistry*, 113(2):96–101, 2013.
- [9] M. R. Cantarino, R. Lora-Serrano, R. Gumeniuk, W. Schnelle, J. Sichelschmidt, A. Leithe-Jasper, Yu. Grin, and F. A. Garcia. Electronic and vibrational properties of the superconducting  $\text{LaPt}_4\text{Ge}_{12}$  skutterudite. *in preparation*, February 2022.
- [10] A. M. G. Carvalho, D. H. C. Araújo, H. F. Canova, C. B. Rodella, D. H. Barrett, S. L. Cuffini, R. N. Costa, and R. S. Nunes. X-ray powder diffraction at the XRD1 beamline at LNLS. *Journal of Synchrotron Radiation*, 23(6):1501–1506, Nov 2016.
- [11] Mogens Christensen, Asger B Abrahamsen, Niels B Christensen, Fanni Juranyi, Niels H Andersen, Kim Lefmann, Jakob Andreasson, Christian RH Bahl, and Bo B Iversen. Avoided crossing of rattler modes in thermoelectric materials. *Nature materials*, 7(10):811–815, 2008.

- [12] Anneke Dittmer, R<sup>3</sup>bert Izsk, Frank Neese, and Dimitrios Maganas. Accurate Band Gap Prediction of 9303 – 9315, July 2019.
- [13] S. J. A. Figueroa, J. C. Mauricio, J. Murari, D. B. Beniz, J. R. Piton, H. H. Slepicka, M. Falcão de Sousa, A. M. Espíndola, and A. P. S. Levinsky. Upgrades to the XAFS2 beamline control system and to the endstation at the LNLS. *Journal of Physics: Conference Series*, 712(1):012022, 2016.
- [14] A. Gippius, M. Baenitz, E. Morozova, A. Leithe-Jasper, W. Schnelle, A. Shevelkov, E. Alkaev, A. Rabis, J. Mydosh, Yu. Grin, and F. Steglich. Crossover between itinerant ferromagnetism and antiferromagnetic fluctuations in filled skutterudites mfe4sb12 (m=na, ba, la) as determined by nmr. *Journal of Magnetism and Magnetic Materials*, 300(1):e403–e406, 2006. The third Moscow International Symposium on Magnetism 2005.
- [15] David J Griffiths. Introduction to electrodynamics, 2005.
- [16] Andrew P. Grosvenor, Ronald G. Cavell, and Arthur Mar. X-ray photoelectron spectroscopy study of the skutterudites LaFe<sub>4</sub>Sb<sub>12</sub>, CeFe<sub>4</sub>Sb<sub>12</sub>, CoSb<sub>3</sub>, and CoP<sub>3</sub>. *Phys. Rev. B*, 74:125102, Sep 2006.
- [17] Roman Gumeniuk, Horst Borrmann, Alim Ormeci, Helge Rosner, Walter Schnelle, Michael Nicklas, Yuri Grin, and Andreas Leithe-Jasper. Filled platinum germanium skutterudites MPt<sub>4</sub>Ge<sub>12</sub> (M = Sr, Ba, La-Nd, Sm, Eu): crystal structure and chemical bonding. *Zeitschrift Fur Kristallographie-Crystalline Materials*, 225(11):531–543, 2010.
- [18] Raphaël P. Hermann, Fernande Grandjean, and Gary J. Long. Einstein oscillators that impede thermal transport. *American Journal of Physics*, 73(2):110–118, January 2005.
- [19] Yanyun Hu, James R. Salvador, Ning Chen, Ahmet Alatas, and Young-June Kim. Anharmonicity in partially filled skutterudites YbxCo<sub>4</sub>Sb<sub>12</sub>. *Journal of Applied Physics*, 130(18):185105, November 2021.
- [20] Oliver Janka and Susan M Kauzlarich. Zintl compounds. *Encyclopedia of Inorganic and Bioinorganic Chemistry*, pages 1–14, 2011.
- [21] W. Jeitschko and D. Braun. LaFe<sub>4</sub>P<sub>12</sub> with filled CoAs<sub>3</sub>-type structure and isotypic lanthanoid-transition metal polyphosphides. *Acta Crystallographica Section B: Structural Crystallography and Crystal Chemistry*, 33(11):3401–3406, 1977.
- [22] Trevor Keiber and Frank Bridges. Modeling correlated motion in filled skutterudites. *Physical Review B*, 92(13):134111, October 2015.
- [23] Michael Marek Koza, Lucia Capogna, Andreas Leithe-Jasper, Helge Rosner, Walter Schnelle, Hannu Mutka, Mark Robert Johnson, Clemens Ritter, and Yuri Grin. Vibrational dynamics of filled skutterudites M<sub>1-x</sub>Fe<sub>4</sub>Sb<sub>12</sub> (M = Ca, Sr, Ba, and Yb). *Physical Review B*, 81(17):174302, May 2010.
- [24] Michael Marek Koza, Mark Robert Johnson, Romain Viennois, Hannu Mutka, Luc Girard, and Didier Ravot. Breakdown of phonon glass paradigm in La- and Ce-filled Fe<sub>4</sub>Sb<sub>12</sub> skutterudites. *Nat Mater*, 7(10):805–810, October 2008.

- [25] Michael Marek Koza, Andreas Leithe-Jasper, Helge Rosner, Walter Schnelle, Hannu Mutka, Mark Robert Johnson, Michael Krisch, Lucia Capogna, and Yuri Grin. Vibrational dynamics of the filled skutterudites  $M_{1-x}Fe_4Sb_{12}$  ( $M = Ca, Sr, Ba, \text{ and } Yb$ ): Temperature response, dispersion relation, and material properties. *Physical Review B*, 84(1):014306, July 2011.
- [26] A. Leithe-Jasper, W. Schnelle, H. Rosner, M. Baenitz, A. Rabis, A. A. Gippius, E. N. Morozova, H. Borrmann, U. Burkhardt, R. Ramlau, U. Schwarz, J. A. Mydosh, Y. Grin, V. Ksenofontov, and S. Reiman. Weak itinerant ferromagnetism and electronic and crystal structures of alkali-metal iron antimonides:  $NaFe_4Sb_{12}$  and  $KFe_4Sb_{12}$ . *Physical Review B*, 70(21):214418, December 2004.
- [27] A. Leithe-Jasper, W. Schnelle, H. Rosner, N. Senthilkumaran, A. Rabis, M. Baenitz, A. Gippius, E. Morozova, J. A. Mydosh, and Y. Grin. Ferromagnetic ordering in alkali-metal iron antimonides:  $NaFe_4Sb_{12}$  and  $KFe_4Sb_{12}$ . *Physical Review Letters*, 91(3):037208, July 2003.
- [28] F. A. Lima, M. E. Saleta, R. J. S. Pagliuca, M. A. Eleotério, R. D. Reis, J. Fonseca JÃºnior, B. Meyer, E. M. Bittar, N. M. Souza-Neto, and E. Granado. XDS: a flexible beamline for X-ray diffraction and spectroscopy at the Brazilian synchrotron. *Journal of Synchrotron Radiation*, 23(6):1538–1549, November 2016.
- [29] Wei Liu, Qing Jie, Qiang Li, Zhiqiang Chen, and Baosheng Li. Synchrotron x-ray study of filled skutterudites  $cefe_4sb_{12}$  and  $ce_{0.8}fe_3cosb_{12}$ . *Physica B: Condensed Matter*, 406(1):52–55, 2011.
- [30] Tian Lu and Feiwu Chen. Multiwfn: A multifunctional wavefunction analyzer. *JOURNAL OF COMPUTATIONAL CHEMISTRY*, 33(5):580–592, FEB 15 2012.
- [31] Huixia Luo, Jason W. Krizan, Lukas Muechler, Neel Haldolaarachchige, Tomasz Klimczuk, Weiwei Xie, Michael K. Fuccillo, Claudia Felser, and Robert J. Cava. A large family of filled skutterudites stabilized by electron count. *Nature Communications*, 6, March 2015.
- [32] Jun Mao, Zihang Liu, Jiawei Zhou, Hangtian Zhu, Qian Zhang, Gang Chen, and Zhifeng Ren. Advances in thermoelectrics. *Advances in Physics*, 67(2):69–147, 2018.
- [33] K. Momma and F. Izumi. VESTA: a three-dimensional visualization system for electronic and structural analysis. *Journal of Applied Crystallography*, 41(3):653–658, June 2008.
- [34] Bassim Mounssef, Marli R. Cantarino, Eduardo M. Bittar, Tarsis M. Germano, Andreas Leithe-Jasper, and Fernando A. Garcia. Hard x-ray spectroscopy of the itinerant magnets  $RFe_4Sb_{12}$  ( $R=Na, K, Ca, Sr, Ba$ ). *Physical Review B*, 99(3):035152, January 2019.
- [35] Ulrich Muller. *Inorganic structural chemistry*. John Wiley & Sons, 2007.
- [36] F. D. Murnaghan. The compressibility of media under extreme pressures. *Proceedings of the National Academy of Sciences*, 30(9):244–247, 1944.
- [37] Frank Neese. The ORCA program system. *WIREs Computational Molecular Science*, 2(1):73–78, 2012. \_eprint: <https://onlinelibrary.wiley.com/doi/pdf/10.1002/wcms.81>.
- [38] Frank Neese, Frank Wennmohs, Ute Becker, and Christoph Riplinger. The ORCA quantum chemistry program package. *The Journal of Chemical Physics*, 152(22):224108, June 2020.



- [39] Matthew Newville. Fundamentals of XAFS. *Reviews in Mineralogy and Geochemistry*, 78(1):33–74, 01 2014.
- [40] Earl F OâBannon III, Zsolt Jenei, Hyunchae Cynn, Magnus J Lipp, and Jason R Jeffries. Contributed review: Culet diameter and the achievable pressure of a diamond anvil cell: Implications for the upper pressure limit of a diamond anvil cell. *Review of Scientific Instruments*, 89(11):111501, 2018.
- [41] Simon Jacques Martin Vickers Paul Barnes, Jeremy Karl Cockcroft. "how do synchrotrons work?". <http://pd.chem.ucl.ac.uk/pdnn/inst2/work.htm>, 2006. [Online; accessed 20-June-2022].
- [42] B. Ravel and M. Newville. ATHENA, ARTEMIS, HEPHAESTUS: data analysis for X-ray absorption spectroscopy using IFEFFIT. *Journal of Synchrotron Radiation*, 12(Pt 4):537–541, July 2005.
- [43] J. J. Rehr and R. C. Albers. Theoretical approaches to x-ray absorption fine structure. *Reviews of Modern Physics*, 72(3):621–654, July 2000.
- [44] João Elias F. S. Rodrigues, Javier Gainza, Federico Serrano-SÃ¡nchez, Mateus M. Ferrer, Guilherme S. L. Fabris, Julio R. Sambrano, Norbert M. Nemes, José L. Martínez, Catalin Popescu, and José A. Alonso. Unveiling the Structural Behavior under Pressure of Filled  $M_0.5Co_4Sb_{12}$  ( $M = K, Sr, La, Ce,$  and  $Yb$ ) Thermoelectric Skutterudites. *Inorganic Chemistry*, 60(10):7413–7421, May 2021.
- [45] Donald E Sands. *Introduction to crystallography*. Courier Corporation, 1993.
- [46] W. Schnelle, A. Leithe-Jasper, H. Rosner, R. Cardoso-Gil, R. Gumeniuk, D. Trots, J. A. Mydosh, and Yu. Grin. Magnetic, thermal, and electronic properties of iron-antimony filled skutterudites  $M Fe_4 Sb_{12}$  ( $M=Na,K,Ca,Sr,Ba,La,Yb$ ). *Physical Review B*, 77(9):094421, March 2008.
- [47] Ichimin Shirotani, Takashi Noro, Junichi Hayashi, Chihiro Sekine, Ram Giri, and Takumi Kikegawa. X-ray study with synchrotron radiation for p- and sb-based skutterudite compounds at high pressures. *Journal of Physics: Condensed Matter*, 16(43):7853–7862, oct 2004.
- [48] Steven H Simon. *The Oxford solid state basics*. OUP Oxford, 2013.
- [49] G. J Snyder and E. S Toberer. Complex thermoelectric materials. *Nature materials*, 7(2):105–114, 2008.
- [50] K Takegahara, H Harima, and A Yanase. Crystal electric fields for cubic point groups. *JOURNAL OF THE PHYSICAL SOCIETY OF JAPAN*, 70(5):1190–1193, MAY 2001.
- [51] Eric S. Toberer, Alex Zevalkink, and G. Jeffrey Snyder. Phonon engineering through crystal chemistry. *J. Mater. Chem.*, 21(40):15843–15852, 2011. Publisher: The Royal Society of Chemistry.
- [52] B. H. Toby and R. B. Von Dreele. GSAS-II: the genesis of a modern open-source all purpose crystallography software package. *Journal of Applied Crystallography*, 46(2):544–549, April 2013.

- [53] H. M. T̃Et̃Enc̃, ErtuÇşrul Karaca, and G. P. Srivastava. Electron-phonon superconductivity in the filled skutterudites LaRu<sub>4</sub>P<sub>12</sub>, LaRu<sub>4</sub>As<sub>12</sub>, and LaPt<sub>4</sub>Ge<sub>12</sub>. *Physical Review B*, 95(21):214514, June 2017.
- [54] Naemi Waeselmann. *Structural transformations in complex perovskite-type relaxor and relaxor-based ferroelectrics at high pressures and temperatures*. PhD thesis, 05 2012.
- [55] J Yang, W Zhang, SQ Bai, Z Mei, and LD Chen. Dual-frequency resonant phonon scattering in ba x r y co<sub>4</sub> sb<sub>12</sub> (r= la, ce, and sr). *Applied Physics Letters*, 90(19):192111, 2007.
- [56] Junko Yano and Vittal K. Yachandra. X-ray absorption spectroscopy. *Photosynthesis Research*, 102(2-3):241–254, December 2009.
- [57] Zhuang-Hao Zheng, Xiao-Lei Shi, Dong-Wei Ao, Wei-Di Liu, Yue-Xing Chen, Fu Li, Shuo Chen, Xiao-Qing Tian, Xin-Ru Li, Jing-Yi Duan, Hong-Li Ma, Xiang-Hua Zhang, Guang-Xing Liang, Ping Fan, and Zhi-Gang Chen. Rational band engineering and structural manipulations inducing high thermoelectric performance in n-type cosb<sub>3</sub> thin films. *Nano Energy*, 81:105683, 2021.

# Appendix A

## Keiber-Bridges model of correlated rattling motion

Here we explain in detail the calculation of the Keiber-Bridges model of correlated rattling motion in order to obtain an effective phonon dispersion associated to the system.

The model to the rattling dynamics in skutterudites considers three distinct elements: the rattler, the pnictogen square ring (in our case the Sb square ring) and the cage, which in this context denotes solely the metal cubic lattice. The elements are connected by four distinct spring constants (for instance, a rattler-square ring spring constant  $k_{RS}$ ) and the system dynamics is treated at a classical level. The corresponding dynamic matrix is then diagonalized to find the four phonon dispersion modes, depicted in the main text. The modes thus obtained can be compared to the phonon dispersion along the [100] as calculated in Ref. [53] by more sophisticated methods. The order of magnitude of the modes frequencies and some qualitative features, such as the presence of avoided crossings and band gaps, are reproduced by the qualitative spring model.

The dynamics of the classical objects is obtained by solving the classical equations of motion. For each element we write:

$$m_c \frac{d^2 u_{1\beta}}{dt^2} = -K_{cc}(u_{1\beta} - u_{3\beta}) - K_{cc}(u_{1\beta} - u_{3[\beta-1]}) - K_{rc}(u_{1\beta} - u_{2\beta}) - K_{sc}(u_{1\beta} - u_{4[\beta-1]})$$

$$m_r \frac{d^2 u_{2\beta}}{dt^2} = -K_{rc}(u_{2\beta} - u_{1\beta}) - K_{rc}(u_{2\beta} - u_{3\beta}) - K_{rs}(u_{2\beta} - u_{4\beta}) - K_{rs}(u_{2\beta} - u_{4[\beta-1]})$$

$$m_c \frac{d^2 u_{3\beta}}{dt^2} = -K_{cc}(u_{3\beta} - u_{1\beta}) - K_{cc}(u_{3\beta} - u_{1[\beta+1]}) - K_{rc}(u_{3\beta} - u_{2\beta}) - K_{sc}(u_{3\beta} - u_{4\beta})$$

$$m_s \frac{d^2 u_{4\beta}}{dt^2} = -K_{sc}(u_{4\beta} - u_{3\beta}) - K_{sc}(u_{4\beta} - u_{1[\beta+1]}) - K_{rs}(u_{4\beta} - u_{2\beta}) - K_{rs}(u_{4\beta} - u_{2[\beta+1]})$$

The above set of equations is then solved by the following Ansatz:

$$u_{\alpha\beta} = \frac{z_{\alpha}(q)}{\sqrt{m_{\alpha}}} \exp i[-\omega t + qa\beta + qa(\alpha-1)/4]$$

in detail we have:

$$\begin{cases} u_{1\beta} &= \frac{z_1(q)}{\sqrt{m_c}} \exp i[-\omega t + qa\beta] \\ u_{2\beta} &= \frac{z_2(q)}{\sqrt{m_r}} \exp i[-\omega t + qa\beta + qa/4] \\ u_{3\beta} &= \frac{z_3(q)}{\sqrt{m_c}} \exp i[-\omega t + qa\beta + qa2/4] \\ u_{4\beta} &= \frac{z_4(q)}{\sqrt{m_s}} \exp i[-\omega t + qa\beta + qa3/4] \end{cases}$$

$$\frac{d^2 u_{\alpha\beta}}{dt^2} = -\omega^2 \frac{z_\alpha(q)}{\sqrt{m_\alpha}} \exp i[-\omega t + qa\beta + qa(\alpha-1)/4]$$

in even more detail, considering each equation, we have:

$$\begin{aligned} m_c \frac{d^2 u_{1\beta}}{dt^2} &= -m_c \omega^2 \frac{z_1(q)}{\sqrt{m_c}} \exp i[-\omega t + qa\beta] = \\ &= -K_{cc} \left( \frac{z_1(q)}{\sqrt{m_c}} \exp i[-\omega t + qa\beta] - \frac{z_3(q)}{\sqrt{m_c}} \exp i[-\omega t + qa\beta + qa2/4] \right) - \\ &-K_{cc} \left( \frac{z_1(q)}{\sqrt{m_c}} \exp i[-\omega t + qa\beta] - \frac{z_3(q)}{\sqrt{m_c}} \exp i[-\omega t + qa(\beta-1) + qa2/4] \right) - \\ &-K_{rc} \left( \frac{z_1(q)}{\sqrt{m_c}} \exp i[-\omega t + qa\beta] - \frac{z_2(q)}{\sqrt{m_r}} \exp i[-\omega t + qa\beta + qa/4] \right) - \\ &-K_{sc} \left( \frac{z_1(q)}{\sqrt{m_c}} \exp i[-\omega t + qa\beta] - \frac{z_4(q)}{\sqrt{m_s}} \exp i[-\omega t + qa(\beta-1) + qa3/4] \right) \end{aligned}$$

we thus divide all the expression by the factor:

$$\sqrt{m_c} \exp i[-\omega t + qa\beta]$$

and reach the following:

$$\begin{aligned} -\omega^2 z_1(q) &= -K_{cc} \left( \frac{z_1(q)}{\sqrt{m_c m_c}} - \frac{z_3(q)}{\sqrt{m_c m_c}} \exp i\left[\frac{qa}{2}\right] \right) - K_{cc} \left( \frac{z_1(q)}{\sqrt{m_c m_c}} - \frac{z_3(q)}{\sqrt{m_c m_c}} \exp i\left[-\frac{qa}{2}\right] \right) - \\ &-K_{rc} \left( \frac{z_1(q)}{\sqrt{m_c m_c}} - \frac{z_2(q)}{\sqrt{m_r m_c}} \exp i\left[\frac{qa}{4}\right] \right) - K_{sc} \left( \frac{z_1(q)}{\sqrt{m_c m_c}} - \frac{z_4(q)}{\sqrt{m_s m_c}} \exp i\left[-\frac{qa}{4}\right] \right) \end{aligned}$$

Now, the second equation:

$$\begin{aligned} m_r \frac{d^2 u_{2\beta}}{dt^2} &= -\sqrt{m_r} \omega^2 z_2(q) \exp i[-\omega t + qa\beta + qa/4] = \\ &= -K_{rc} \left( \frac{z_2(q)}{\sqrt{m_r}} \exp i[-\omega t + qa\beta + qa/4] - \frac{z_1(q)}{\sqrt{m_c}} \exp i[-\omega t + qa\beta] \right) - \\ &-K_{rc} \left( \frac{z_2(q)}{\sqrt{m_r}} \exp i[-\omega t + qa\beta + qa/4] - \frac{z_3(q)}{\sqrt{m_c}} \exp i[-\omega t + qa\beta + qa2/4] \right) - \\ &-K_{rs} \left( \frac{z_2(q)}{\sqrt{m_r}} \exp i[-\omega t + qa\beta + qa/4] - \frac{z_4(q)}{\sqrt{m_s}} \exp i[-\omega t + qa\beta + qa3/4] \right) - \end{aligned}$$

$$-K_{rs}\left(\frac{z_2(q)}{\sqrt{m_r}} \exp i[-\omega t + qa\beta + qa/4] - \frac{z_4(q)}{\sqrt{m_s}} \exp i[-\omega t + qa(\beta - 1) + qa3/4]\right)$$

and dividing all the expression by the factor:

$$\sqrt{m_r} \exp i[-\omega t + qa\beta + qa/4]$$

we have:

$$\begin{aligned} -\omega^2 z_2(q) = & -K_{rc}\left(\frac{z_2(q)}{\sqrt{m_r m_r}} - \frac{z_1(q)}{\sqrt{m_c}} \exp i\left[-\frac{qa}{4}\right]\right) - K_{rc}\left(\frac{z_2(q)}{\sqrt{m_r m_r}} - \frac{z_3(q)}{\sqrt{m_c m_r}} \exp i\left[\frac{qa}{4}\right]\right) - \\ & -K_{rs}\left(\frac{z_2(q)}{\sqrt{m_r m_r}} - \frac{z_4(q)}{\sqrt{m_s m_r}} \exp i\left[\frac{qa}{2}\right]\right) - K_{rs}\left(\frac{z_2(q)}{\sqrt{m_r m_r}} - \frac{z_4(q)}{\sqrt{m_s m_r}} \exp i\left[-\frac{qa}{2}\right]\right) \end{aligned}$$

The third equation now writes:

$$\begin{aligned} m_c \frac{d^2 u_{3\beta}}{dt^2} = & -\sqrt{m_c} \omega^2 z_3(q) \exp i[-\omega t + qa\beta + qa2/4] = \\ = & -K_{cc}\left(\frac{z_3(q)}{\sqrt{m_c}} \exp i[-\omega t + qa\beta + qa2/4] - \frac{z_1(q)}{\sqrt{m_c}} \exp i[-\omega t + qa\beta]\right) - \\ & -K_{cc}\left(\frac{z_3(q)}{\sqrt{m_c}} \exp i[-\omega t + qa\beta + qa2/4] - \frac{z_1(q)}{\sqrt{m_c}} \exp i[-\omega t + qa(\beta + 1)]\right) - \\ & -K_{rc}\left(\frac{z_3(q)}{\sqrt{m_c}} \exp i[-\omega t + qa\beta + qa2/4] - \frac{z_2(q)}{\sqrt{m_r}} \exp i[-\omega t + qa\beta + qa/4]\right) - \\ & -K_{sc}\left(\frac{z_3(q)}{\sqrt{m_c}} \exp i[-\omega t + qa\beta + qa2/4] - \frac{z_4(q)}{\sqrt{m_s}} \exp i[-\omega t + qa\beta + qa3/4]\right) \end{aligned}$$

dividing by the factor

$$\sqrt{m_c} \exp i[-\omega t + qa\beta + qa2/4]$$

we have:

$$\begin{aligned} -\omega^2 z_3(q) = & -K_{cc}\left(\frac{z_3(q)}{\sqrt{m_c m_c}} - \frac{z_1(q)}{\sqrt{m_c m_c}} \exp i\left[-\frac{qa}{2}\right]\right) - K_{cc}\left(\frac{z_3(q)}{\sqrt{m_c m_c}} - \frac{z_1(q)}{\sqrt{m_c m_c}} \exp i\left[\frac{qa}{2}\right]\right) - \\ & -K_{rc}\left(\frac{z_3(q)}{\sqrt{m_c m_c}} - \frac{z_2(q)}{\sqrt{m_r m_c}} \exp i\left[-\frac{qa}{4}\right]\right) - K_{sc}\left(\frac{z_3(q)}{\sqrt{m_c m_c}} - \frac{z_4(q)}{\sqrt{m_s m_c}} \exp i\left[\frac{qa}{4}\right]\right) \end{aligned}$$

Finally, the fourth equation:

$$\begin{aligned} m_s \frac{d^2 u_{4\beta}}{dt^2} = & -\omega^2 \sqrt{m_s} z_4(q) \exp i[-\omega t + qa\beta + qa3/4] = \\ = & -K_{sc}\left(\frac{z_4(q)}{\sqrt{m_s}} \exp i[-\omega t + qa\beta + qa3/4] - \frac{z_3(q)}{\sqrt{m_c}} \exp i[-\omega t + qa\beta + qa2/4]\right) - \end{aligned}$$

$$\begin{aligned}
 & -K_{sc} \left( \frac{z_4(q)}{\sqrt{m_s}} \exp i[-\omega t + qa\beta + qa3/4] - \frac{z_1(q)}{\sqrt{m_c}} \exp i[-\omega t + qa(\beta + 1)] \right) - \\
 & -K_{rs} \left( \frac{z_4(q)}{\sqrt{m_s}} \exp i[-\omega t + qa\beta + qa3/4] - \frac{z_2(q)}{\sqrt{m_r}} \exp i[-\omega t + qa\beta + qa/4] \right) - \\
 & -K_{rs} \left( \frac{z_4(q)}{\sqrt{m_s}} \exp i[-\omega t + qa\beta + qa3/4] - \frac{z_2(q)}{\sqrt{m_r}} \exp i[-\omega t + qa(\beta + 1) + qa/4] \right)
 \end{aligned}$$

by dividing all the expression by the factor:

$$\sqrt{m_s} \exp i[-\omega t + qa\beta + qa3/4]$$

we get:

$$\begin{aligned}
 -\omega^2 z_4(q) = & -K_{sc} \left( \frac{z_4(q)}{\sqrt{m_s m_s}} - \frac{z_3(q)}{\sqrt{m_c m_s}} \exp i\left[-\frac{qa}{4}\right] \right) - K_{sc} \left( \frac{z_4(q)}{\sqrt{m_s m_s}} - \frac{z_1(q)}{\sqrt{m_c m_s}} \exp i\left[\frac{qa}{4}\right] \right) - \\
 & -K_{rs} \left( \frac{z_4(q)}{\sqrt{m_s m_s}} - \frac{z_2(q)}{\sqrt{m_r m_s}} \exp i\left[-\frac{qa}{2}\right] \right) - K_{rs} \left( \frac{z_4(q)}{\sqrt{m_s m_s}} - \frac{z_2(q)}{\sqrt{m_r m_s}} \exp i\left[\frac{qa}{2}\right] \right)
 \end{aligned}$$

And the resulting dynamic matrix is:

$$\left( \begin{array}{cccc}
 \frac{-2K_{cc} - K_{rc} - K_{sc}}{m_c} & \frac{K_{rc}}{\sqrt{m_r m_c}} \exp i\left[\frac{qa}{4}\right] & \frac{2K_{cc}}{m_c} \cos(qa/2) & \frac{K_{sc}}{\sqrt{m_s m_c}} \exp i\left[-\frac{qa}{4}\right] \\
 \frac{K_{rc}}{\sqrt{m_c m_r}} \exp i\left[-\frac{qa}{4}\right] & \frac{-2K_{rc} - 2K_{rs}}{m_r} & \frac{K_{rc}}{\sqrt{m_c m_r}} \exp i\left[\frac{qa}{4}\right] & \frac{2K_{rs}}{\sqrt{m_s m_r}} \cos(qa/2) \\
 \frac{2K_{cc}}{m_c} \cos(qa/2) & \frac{K_{rc}}{\sqrt{m_r m_c}} \exp i\left[-\frac{qa}{4}\right] & \frac{-2K_{cc} - K_{rc} - K_{sc}}{m_c} & \frac{K_{sc}}{\sqrt{m_s m_c}} \exp i\left[\frac{qa}{4}\right] \\
 \frac{K_{sc}}{\sqrt{m_c m_s}} \exp i\left[\frac{qa}{4}\right] & \frac{2K_{rs}}{\sqrt{m_r m_s}} \cos(qa/2) & \frac{K_{sc}}{\sqrt{m_c m_s}} \exp i\left[-\frac{qa}{4}\right] & \frac{-2K_{sc} - 2K_{rs}}{m_s}
 \end{array} \right)$$

which confirms the dynamic matrix obtained in Ref. [22]. From this point we can proceed to the diagonalization of the matrix to obtain  $-\omega^2$  as a function of  $q$ .

In our work, we have adopted  $K_{cc}^{K(Ca)} = 10 \text{ eV/\AA}^2$  and  $K_{cc}^{Ba} = 25 \text{ eV/\AA}^2$ , based on proportion of obtained  $K_{eff}^{R,Fe-Fe}$  parameters, and  $K_{cs} = 1.8 \text{ eV/\AA}^2$  for all samples, based on the  $K_{eff}^{R,Fe-Sb}$  parameter. The  $K_{sc}^R$  spring constants were evaluated for a range of parameters based on previous works [22, 7]. In order to get similar results to Keiber's [22], we divide the modes by 4, which is the number of elements in the unit cell.

# Appendix B

## Scientific Outputs

### B.1 Papers

#### Accepted paper - Physical Review Materials

“Vibrational and Structural Properties of  $RFe_4Sb_{12}$  (R = Na, K, Ca, Sr, Ba) Filled Skutterudites”

**Authors:** J. G. de Abrantes, M. R. Cantarino, W. R. da Silva Neto, V. V. Freire, A. G. Figueiredo, T. M. Germano, B. Mounsef Jr., E. M. Bittar, A. Leithe-Jasper, F. A. Garcia.

Summarizes the work of this master’s dissertation. The preview version can be found as an annex in the following pages.

### B.2 Events

#### Oral Presentation

“Vibrational and Structural Properties of  $RFe_4Sb_{12}$  (R = Na, K, Ca, Sr, Ba) Filled Skkuterudites”

**Event:** EOSBF 2022 (Encontro de Outono da Sociedade Brasileira de Física) of LNLS/CNPEM. São Paulo, SP.

# Vibrational and structural properties of the $R\text{Fe}_4\text{Sb}_{12}$ ( $R = \text{Na, K, Ca, Sr, Ba}$ ) filled skutterudites

Juliana G. de Abrantes<sup>1</sup>, Marli R. Cantarino<sup>1</sup>, Wagner R. da Silva Neto<sup>1,2</sup>, Victória V. Freire<sup>1</sup>, Alvaro G. Figueiredo<sup>1</sup>, Tarsis M. Germano<sup>1</sup>, Bassim Mounssef Jr.<sup>2</sup>, Eduardo M. Bittar<sup>3</sup>, Andreas Leithe-Jasper<sup>4</sup>, Fernando A. Garcia<sup>1</sup>

<sup>1</sup>*Instituto de Física, Universidade de São Paulo, 05508-090, São Paulo-SP, Brazil*

<sup>2</sup>*Instituto de Química, Universidade de São Paulo, 05508-090, São Paulo-SP, Brazil*

<sup>3</sup>*Centro Brasileiro de Pesquisas Físicas, Rio de Janeiro, RJ 22290-180, Brazil and*

<sup>4</sup>*Max Planck Institute for Chemical Physics of Solids, D-01187 Dresden, Germany.*

Vibrational and elastic properties of the  $R\text{Fe}_4\text{Sb}_{12}$  skutterudites are investigated by, respectively, temperature ( $T$ ) dependent extended X-ray absorption fine structure (EXAFS) and pressure ( $P$ ) dependent x-ray diffraction (XRD) experiments. The Fe  $K$ -edge EXAFS experiments of the  $R = \text{K, Ca}$  and  $\text{Ba}$  materials were performed in the  $T$ -interval  $06 < T < 300$  K and XRD experiments of the  $R = \text{Na, K, Ca, Sr}$  and  $\text{Ba}$  materials were performed in the  $P$ -interval  $1 \text{ atm} < P < 16$  GPa. From EXAFS, we obtained the correlated Debye-Waller parameters that were thus analyzed to extract effective spring constants connected with the Fe- $Y$  (where  $Y = \text{either } R, \text{ Fe or Sb}$ ) scattering paths. Our findings suggest that in the case of the light cations,  $R = \text{K or Ca}$ , the  $R$  atoms are relatively weakly coupled to the cage, in a scenario reminiscent to the Einstein oscillators. From the XRD experiments, we obtained the bulk modulus  $B_0$  for all  $R = \text{Na, K, Ca, Sr}$  and  $\text{Ba}$  materials, with values ranging from 77 GPa ( $R = \text{K}$ ) to  $R = 99$  GPa ( $R = \text{Ba}$ ) as well as the compressibility  $\beta$  as a function of  $P$ . The trend in  $\beta$  as a function of the  $R$  filler is discussed and is shown that it does not correlate with simple geometrical considerations but rather to the filler-cage bonding properties.

## I. INTRODUCTION

Filled skutterudites are materials with chemical formula  $RT_4X_{12}$  where the  $T_4X_{12}$  elements form a relatively rigid cage framework inside which the  $R$  elements are allocated [1]. In the simplest chemical bonding scenario, the cage is structured by strong  $T-X$  covalent bondings and the  $R$  fillers generically display a cationic character, donating electrons that further stabilize the  $T_4X_{12}$  cage. While it is well known that the description of bonding in filled skutterudites is more involved [2], this simple picture can be applied as a guide to discover new filled skutterudites [3] as well as to justify their unusual vibrational dynamics [4].

Concerning the latter topic, research on the filled skutterudites is indeed triggered mostly by the presence of an unusual vibrational dynamics that makes the filled skutterudites good candidates for thermoelectric applications [5–7]. In this regard, earlier contributions proposed that the  $R$  fillers behave as independent, non dispersive and low energy oscillators (or rattlers), that scatter the cage derived phonons, giving rise to a phonon glass, which impedes the thermal conduction and raises the material thermoelectric figure of merit  $ZT$  [8].

On one account, the phonon glass scenario provided a first approach to understand the skutterudites' vibrational dynamics. For instance, filling the cages with distinct fillers may cause the smaller  $R$  cations to display an unusual rattling behavior in the oversized cage, as observed [9, 10]. This scenario, however, was soon challenged [11] and it is now well understood that the separation between rattler and cage vibrational dynamics does not offer an adequate description of the filled skutterudite vibrational properties [12–14]. All this understanding is particularly true in the case of the  $R\text{Fe}_4\text{Sb}_{12}$  ( $R = \text{Na, K, Ca, Sr, Ba, La and Yb}$ ) skutterudites [15–20] and provides support for the design of more efficient antimony based skutterudite materials [21–23].

K, Ca, Sr, Ba, La and Yb) skutterudites [15–20] and provides support for the design of more efficient antimony based skutterudite materials [21–23].

On top of the good potential for thermoelectric applications, filled skutterudites are very flexible platforms, displaying a broad range of electronic, magnetic and thermal properties [24]. The  $R\text{Fe}_4\text{Sb}_{12}$  ( $R = \text{Na, K, Ca, Sr, Ba and La}$ ) materials, in particular, are itinerant magnets [15, 25–29] whose magnetic properties are dominated by a high density of states due to the mixing between the Fe derived  $3d$  states and Sb derived  $5p$  states forming heavy bands in the vicinity of the Fermi level [30, 31].

In this work, we focus on the vibrational and structural properties of the  $R\text{Fe}_4\text{Sb}_{12}$  ( $R = \text{Na, K, Ca, Sr}$  and  $\text{Ba}$ ) filled skutterudites as investigated, respectively, by temperature ( $T$ ) dependent extended x-ray absorption fine structure (EXAFS) and pressure ( $P$ ) dependent x-ray diffraction (XRD) experiments. EXAFS was soon recognized by Cao *et al* [32] as a suitable probe for the site-specific vibrational dynamics in skutterudites. Later contributions [33–35] developed the application of the technique to the correlated nature of the filler-cage vibrational dynamics. Here, we focus on the Fe  $K$ -edge EXAFS of the  $R = \text{K, Ca}$  and  $\text{Ba}$  samples. In our investigation, we find that the cage vibrational dynamics clearly depend on the filler type, corroborating the correlated nature of the filler-cage dynamics.

Our XRD experiments were carried out for pressures typically up to  $\approx 16$  GPa for all samples, except in the case of  $\text{BaFe}_4\text{Sb}_{12}$ , which was investigated up to 24 GPa. Overall, the  $P$ -dependence of all samples is well described by the Birch-Murnaghan model [36] from which we extract the bulk modulus  $B_0$  for each  $R$ . The  $B_0$  behavior as a function of  $R$  is discussed in the context of bonding specific properties of the  $R\text{Fe}_4\text{Sb}_{12}$  skutterudites. This



discussion is supported by quantum chemistry calculations. Moreover, starting at pressures about  $\approx 12$  GPa, the XRD results display broad reflections. This finding suggests that the  $R\text{Fe}_4\text{Sb}_{12}$  materials undergo a process of increasing lattice disorder triggered by pressure, which is reminiscent of the pressure-induced partial amorphization observed for other cage systems [37].

## II. METHODS

High-quality polycrystalline samples of  $R\text{Fe}_4\text{Sb}_{12}$  ( $R = \text{Na}, \text{K}, \text{Ca}, \text{Sr}, \text{Ba}$ ) skutterudites were synthesized by a solid-state sintering method [25]. Fe  $K$ -edge EXAFS experiments of the  $R = \text{K}, \text{Ca}$ , and  $\text{Ba}$  samples were performed at the XAFS2 [38] beamline of the Brazilian Synchrotron Light Source (CNPEM-LNLS). The spectra of the  $\text{K}$  and  $\text{Ca}$  filled materials were measured by both fluorescence and transmission modes, whereas the  $\text{Ba}$  filled material was measured only in the fluorescence mode. A complete temperature scan in the interval  $300 > T > 6$  K was obtained for the three samples. A Fe foil, kept at room temperature, was measured in the transmission mode as a reference throughout the experiments. A conventional He-flow cryostat was employed to achieve temperatures down to  $T = 6$  K.

The EXAFS data were analyzed by multiple scattering theory implemented by the FEFF code [39]. The graphical Demeter platform [40] was adopted to perform the fittings of a structural model including single and multiple scattering paths up to  $5 \text{ \AA}$  from the Fe absorber. To decrease the number of parameters in the fitting, the EXAFS  $S_0^2$  parameter (the path amplitudes) was obtained from *Ab initio* calculations implemented by the FEFF8.4 code. The *Ab initio* calculations were performed for clusters of 226 atoms, adopting the Hedin-Lundqvist pseudopotential to account for the exchange interaction [31].

The powder XRD experiments were performed at the XDS [41] beamline of the CNPEM-LNLS at room temperature. A diamond anvil cell (DAC) was employed during experiments to achieve pressures up to 24 GPa ( $R = \text{Ba}$ ), but typically up to 16 GPa ( $R = \text{Na}, \text{K}, \text{Ca}$ , and  $\text{Sr}$ ). A mixture of methanol and ethanol (in a 4 : 1 proportion) was adopted as a pressure media. The pressure was measured by monitoring the Raman fluorescence from a ruby standard mounted in the DAC together with the samples. In all measurements, the X-ray energy was set to 20 keV. The XRD powder profile fitting and background removal were performed with the GSAS-II software [42].

The filler-cage bonding properties of the  $R = \text{Ca}, \text{Sr}$  and  $\text{Ba}$  filled materials were calculated within the density functional theory (DFT) approximation, adopting the ORCA 5.0 program package [43, 44]. A supercell containing a total of 339 atoms was generated for the calculations which were implemented in an *embedded approach*, shown to predict local properties with good accuracy [45]. Here, a cell of 45 atoms containing one filler plus the cage atoms was treated at a quantum level. This cell was seg-

regated by 2 atomic layers of atoms described as capped effective core potentials (cECPs) to avoid spurious electron leakage [45]. The remaining atoms were simulated in a molecular mechanics approach, with their charges ascribed in agreement with the Zintl phase concept to constrain the 24 electron rule per  $\text{FeSb}_3$  unit [46] by means of a force field. All atomic positions were obtained from crystallographic data. For all atoms, the BP86 hybrid functionals and the Karlsruhe valence triple- $\zeta$  with one set of polarization functions were adopted as the basis set. Spin-orbit coupling effects were considered but no sizable effects were observed in the constitution of most relevant bonding MOs.

## III. RESULTS AND DISCUSSION

### A. EXAFS analysis and vibrational properties

Our EXAFS experiments focus on the Fe  $K$ -edge EXAFS of the  $R\text{Fe}_4\text{Sb}_{12}$  ( $R = \text{K}, \text{Ca}$  and  $\text{Ba}$ ) materials to understand how their vibrational properties evolve as a function of the filler. Among the  $R = \text{Na}, \text{K}, \text{Ca}, \text{Sr}$ , and  $\text{Ba}$  filled materials, the changing periodic properties concern the filler charge and the filler-cage mass/size relation. By selecting the  $\text{K}$  and  $\text{Ca}$  filled materials, we probe the effects of the filler charge, whereas the filler-cage mass relation is kept nearly constant. Choosing the  $\text{Ca}$  and  $\text{Ba}$  filled cases, the filler-cage mass/size relation is probed, whereas keeping the filler charge constant. Our choice of  $R$  thus suffices to capture the important trends of the vibrational dynamics of the  $R\text{Fe}_4\text{Sb}_{12}$  material.

In figures 1(a)–(c) we present three representations of the skutterudite structure. The  $R$  fillers, Fe atoms and Sb atoms are represented, respectively, by red, blue and green spheres. In figure 1(a), we show the typical conventional unit cell representation, where we highlight the  $\text{FeSb}_6$  octahedra. In figure 1(b), we centered the representation in a given Fe atom, which we call the absorber, and leave only the atoms that are about  $5 \text{ \AA}$  apart from this Fe atom. In figure 1(c), we show an alternative representation, where we show the filler, the square Sb ring and the Fe cage. This representation highlights the vibrating components of the effective 1D model for the correlated rattling dynamics in filled skutterudites [34, 35] which we will discuss below.

The Fourier transformed data for all  $T$  values are presented in figures 1(d), (e) and (f) for the  $R = \text{K}, \text{Ca}$  and  $\text{Ba}$  materials, respectively. Our EXAFS analysis is based upon single and multiple scattering paths within the cluster depicted in figure 1(b). This cluster includes all atoms within  $5 \text{ \AA}$  from the absorber. In this range, there are five Fe -  $Y$  single scattering paths, where  $Y$  is the scattering element. The second and third Sb nearest neighbors, denoted  $\text{Sb}_2$  and  $\text{Sb}_3$ , are too close to each other, and thus we adopt a single correlated Debye-Waller parameter  $\sigma_{\text{Fe-Sb}_{2,3}}^2$  to describe both paths. In total, four  $\sigma_{\text{Fe-Y}}^2$  are considered:  $\sigma_{\text{Fe-Sb}_1}^2$ ,  $\sigma_{\text{Fe-R}_1}^2$ ,  $\sigma_{\text{Fe-Sb}_{2,3}}^2$  and  $\sigma_{\text{Fe-Fe}_1}^2$ .

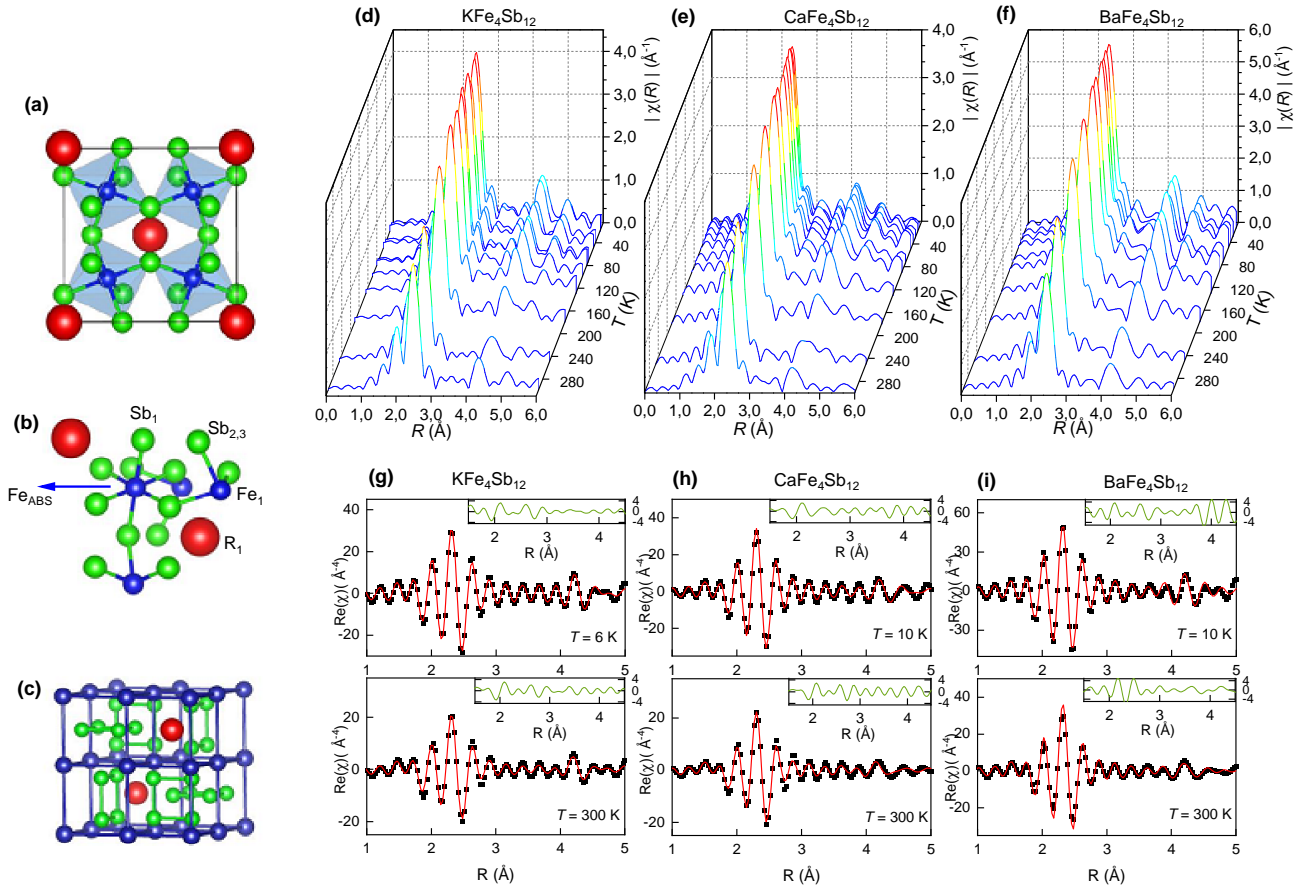


Figure 1. (a) – (c) Three representations of the ternary filled skutterudite structure (space group  $Im\bar{3}$ ): the  $R\text{Fe}_4\text{Sb}_{12}$  conventional unit cell highlighting the  $\text{FeSb}_3$  distorted octahedra; c) the structural elements considered in the EXAFS analysis; c) the vibrating elements of the 1D correlated rattling model (see text) [47]. In all cases, the  $R$ , Fe and Sb atoms are represented by, respectively, red, blue and green spheres. (d) – (f) Fourier transformed EXAFS spectra of the  $R = \text{K}$ , Ca and Ba materials in  $T$ -interval  $10 \text{ K} < T < 300 \text{ K}$ . (g) – (i) Low- $T$  (upper panel) and high- $T$  (lower panel) representative EXAFS data and data analysis (thick red line) for the  $R = \text{K}$ , Ca and Ba materials. In each panel, the inset shows the residuals of the presented fittings.

Single scattering paths dominate the EXAFS signal, but multiple scattering paths were included to improve the data refinement. The disorder parameters of the latter were modeled in terms of the single scattering path  $\sigma_{\text{Fe}-Y}^2$  parameters. In its turn, the  $T$ -dependence of the  $\sigma_{\text{Fe}-Y}^2$  parameters were modeled on the basis of the Debye model for correlated disorder for all Fe- $Y$  paths but the Fe- $R$  paths, which were analyzed under the Einstein model, as typical for filled skutterudite materials [32, 33]. Higher-order cumulants, which suggest the presence of anharmonic vibrations [48], were not adopted in our models. Representative fittings and residuals (for low and high  $T$  data) for the  $R = \text{K}$ , Ca and Ba cases are displayed in figures 1(g) – (i), showing that the structural model adopted in this paper offers a fair description of the data in all  $T$ -interval.

In figures 2(a) – (c) we show the correlated Debye-Waller parameters obtained from the EXAFS experi-

ments. Whereas the Fe- $\text{Sb}_1$  and Fe- $\text{Sb}_{2,3}$  bond disorder parameters are nearly  $R$ -independent, the difference between the Fe-Fe and Fe- $R$  disorder parameters is significant when the cases of the light and heavy fillers are compared. This concerns not only the temperature dependence of the parameters, which is set by the relevant energy scales (either the Debye or Einstein temperatures), but also the order of magnitude of the parameters. In particular, one should note the relatively small disorder of the Fe-Ba path in comparison with the Fe-K and Fe-Ca cases. To a more quantitative analysis, we turn to the obtained energy scales. From now on, we denote by  $\theta_D^{R,\text{Fe}-Y}$  the Debye temperature obtained for the Fe -  $Y$  path of the  $R$  filled sample and by  $\theta_E^{\text{Fe}-R}$  the analogous Einstein temperature. All results are compiled in table I.

The  $\theta_D^{R,\text{Fe}-\text{Sb}_1}$  parameters display a weak dependence

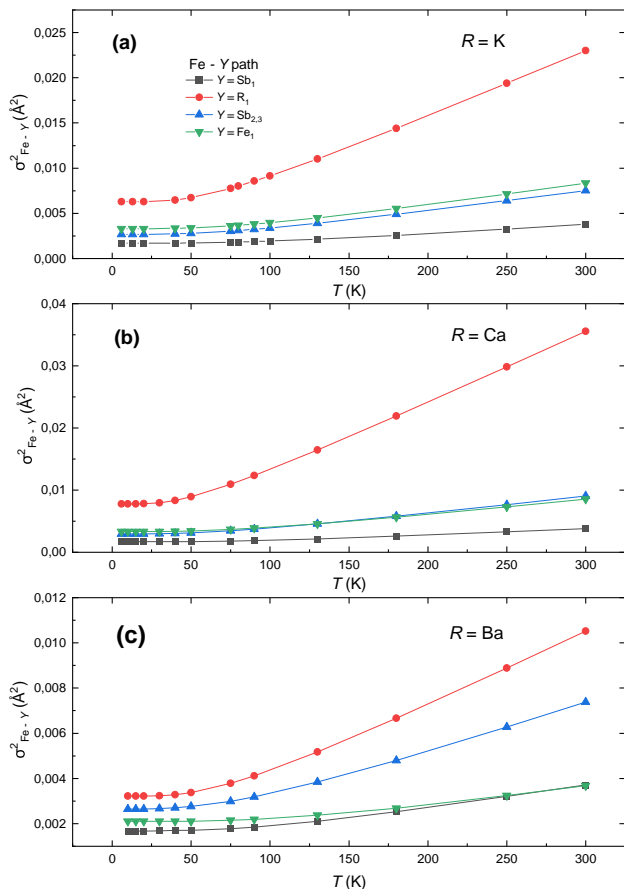


Figure 2. Temperature dependence of the correlated Debye-Waller parameters obtained from the Fe  $K$ -edge EXAFS analysis for the (a)  $K\text{Fe}_4\text{Sb}_{12}$ , (b)  $\text{CaFe}_4\text{Sb}_{12}$  and (c)  $\text{BaFe}_4\text{Sb}_{12}$  samples.

with  $R$  and compare well with those obtained in the early study by Cao *et al* [32] for the  $R = \text{Ce}$  and  $\text{La}$  cases ( $\approx 390$  K), suggesting that the Fe-Sb bondings are not much affected by the filler. The  $\theta_E^{\text{Fe}-R}$  here obtained, however, are significantly larger than those obtained by EXAFS of the  $R = \text{La}$  and  $\text{Ce}$  cases, but are closer to values determined from atomic displacement parameters (ADPs) for the  $R = \text{Ba}$  and  $\text{Ca}$  cases Schnelle *et al.* [15] (one should, of course, keep in mind the difference between the quantities obtained by EXAFS and ADPs). As for the overall trend in the data,  $\theta_E^{\text{Fe}-\text{Ba}} > \theta_E^{\text{Fe}-\text{K}} > \theta_E^{\text{Fe}-\text{Ca}}$ , similar results are obtained by heat capacity Schnelle *et al.* [15], even though the heat capacity results are more indicative of  $\theta_E^{\text{Fe}-\text{Ba}} > \theta_E^{\text{Fe}-\text{K}} \approx \theta_E^{\text{Fe}-\text{Ca}}$ . Concerning the  $\theta_D^{\text{Fe-Fe}}$  parameters, the values obtained in the  $R = \text{K}$  or  $\text{Ca}$  cases are similar to results for other skutterudites [32, 33, 35] whereas the Fe-Fe vibrations are particularly harder in the  $R = \text{Ba}$  case.

The high-temperature limit of the  $\sigma^2$  parameters of each single scattering path can be connected to an effective spring constant ( $K_{\text{eff}}^R$ ) as discussed in detail in

Refs. [33, 35]. We denote by  $K_{\text{eff}}^{R,\text{Fe}-Y}$  the effective spring constant for the Fe -  $Y$  path of the  $R$  filled sample. Effective spring constants describe better the vibrational properties than a direct comparison between the Debye (Einstein) temperatures since they take into account the reduced mass of the vibrating elements and the fact that the  $K_{\text{eff}}^{R,\text{Fe}-Y}$  are not linearly dependent on the Debye (Einstein) temperatures. The parameters are listed in table I.

Translated to  $K_{\text{eff}}^{R,\text{Fe}-Y}$ , the vibrational properties of Fe - Sb bondings for the  $R = \text{K}$ ,  $\text{Ca}$  and  $\text{Ba}$  filled materials are similar, with the difference being less than 5% between the parameters  $K_{\text{eff}}^{R,\text{Fe}-\text{Sb}_1}$ . It is also very similar to the vibrational properties of the Co - Sb bondings as investigated by EXAFS [49]. Inspection of the  $K_{\text{eff}}^{R,\text{Fe}-R}$  parameters, on the other hand, reveals a much larger variation as a function of  $R$ . Indeed,  $K_{\text{eff}}^{\text{Ba,Fe-Ba}}/K_{\text{eff}}^{\text{Ca,Fe-Ca}} \approx 3.5$ , stating a clear distinction between the cases of heavy and light fillers. It suggests a relative decoupling of the filler-cage vibrational dynamics in the case of the light-weight cations, a result that is in agreement with previous analysis of the  $R\text{Fe}_4\text{Sb}_{12}$  atomic displacement parameters (ADPs) [15]. It so appears that the light-weight cations may behave as “rattlers” which, however, are not totally independent of the cage vibrations. We note that the  $K_{\text{eff}}^{\text{Ba,Fe-Ba}}$  parameter compares well with the Ru - Ce and Pt - La cases, obtained from EXAFS experiments of  $\text{CeRu}_4\text{As}_{12}$  [34, 35] and  $\text{LaPt}_4\text{Ge}_{12}$  [50] respectively, which are other examples of heavy fillers filled skutterudites. These results, however, are not simply expressing the filler-cage mass relation, but rather the potential energies of the cations, as discussed by previous calculations of the  $R\text{Fe}_4\text{Sb}_{12}$  [16]. The Fe - Fe vibrations are evidenced by the analysis of the  $K_{\text{eff}}^{R,\text{Fe-Fe}}$  parameters to be distinctive harder in the case of the Ba filled samples, suggesting stronger Fe-Fe bonding in this case. We note that  $K_{\text{eff}}^{\text{Ba,Fe-Fe}}/K_{\text{eff}}^{R,\text{Fe-Fe}} \approx 2.8$  for both  $R = \text{K}$  or  $\text{Ca}$ .

The effective spring constants can be applied to the discussion of an effective 1D phonon model, introduced by Keiber *et al.* [33, 35], for the qualitative description of the correlated filler-cage motion in filled skutterudites. The model considers the three distinct elements illustrated in figure 1(c): the  $R$  filler (or rattler), the Sb square ring and the Fe metal cage, which denotes solely the Fe cubic lattice. The coupled character of the vibrational dynamics is given by connecting the elements by four distinct spring constants for each  $R$  filled skutterudite: a rattler-square ring ( $k_{\text{rs}}^R$ ), a rattler-metal cage ( $k_{\text{rc}}^R$ ), a metal cage-metal cage ( $k_{\text{cc}}^R$ ) and a metal cage-square ring ( $k_{\text{cs}}^R$ ). The system dynamics is treated at a classical level and the corresponding dynamic matrix is diagonalized to find four phonon dispersion modes  $\omega_j(q)$ , where  $q$  is the phonon wave-vector [35]. We shall discuss two aspects of the coupled vibrations that can be connected to our experimental results: *i*) the filler-cage mass relation; *ii*) the dependence of the  $k_{\text{rc}}^R$  constants on whether

Table I. The  $\theta$  (either  $\theta_D^{R,Fe-Y}$  or  $\theta_E^{Fe-R}$ ) and  $K_{\text{eff}}$  parameters obtained from the analysis of the correlated Debye-Waller parameters.

Fe $K$ -edge	KFe <sub>4</sub> Sb <sub>12</sub>		CaFe <sub>4</sub> Sb <sub>12</sub>		BaFe <sub>4</sub> Sb <sub>12</sub>	
Path	$\theta$ (K)	$K_{\text{eff}}$ (eV/Å <sup>2</sup> )	$\theta$ (K)	$K_{\text{eff}}$ (eV/Å <sup>2</sup> )	$\theta$ (K)	$K_{\text{eff}}$ (eV/Å <sup>2</sup> )
Fe - Sb <sub>1</sub>	422(15)	8.13	419(14)	8.13	426(17)	8.45
Fe - $R$	168(61)	1.15	134(51)	0.74	190(43)	2.55
Fe - Sb <sub>2,3</sub>	356(26)	3.85	323(23)	3.12	360(15)	3.92
Fe - Fe <sub>1</sub>	395(75)	3.56	390(77)	3.45	620(80)	9.79

$R$  is a light or heavy element (as suggested by the experimentally obtained  $K_{\text{eff}}^{R,Fe-R}$  parameters). Moreover, we shall fix the parameter  $k_{\text{cs}}^R = 1.8 \text{ eV/Å}^2$  for all samples, as suggested by the experimentally obtained  $K_{\text{eff}}^{R,Fe-Sb}$  and adopt  $k_{\text{cc}}^{\text{K(Ca)}} = 10 \text{ eV/Å}^2$  and  $k_{\text{cc}}^{\text{Ba}} = 25 \text{ eV/Å}^2$  based on the variation of the obtained  $K_{\text{eff}}^{R,Fe-Fe}$  parameters. Our experiments do not offer an estimate about the  $k_{\text{rs}}^R$  parameters and we choose to adopt a range of values in reference to previous works [34, 35].

One should keep in mind that there is no one-to-one correspondence between the  $K_{\text{eff}}^{R,Fe-Y}$  and spring constants of the 1D effective model. Rather, the  $K_{\text{eff}}^{R,Fe-Y}$  constants are adopted to get reasonable estimates to the spring constants, in particular to their relative values. Formally, the spring constants are a functional of the  $K_{\text{eff}}^{R,Fe-Y}$  and that there is a strong functional dependence between, for instance,  $K_{\text{eff}}^{R,Fe-Fe}$  and  $k_{\text{cc}}^R$  or  $K_{\text{eff}}^{R,Fe-R}$  and  $k_{\text{rc}}^R$ . Results of the phonon dispersion and the exact parameters adopted are displayed in figures 3(a)-(o) and in the figure caption.

In figures 3(a)-(i), the mass-relation between the  $R$  cations and the cage elements is that of the KFe<sub>4</sub>Sb<sub>12</sub> case (which, in view of the qualitative nature of the calculated dispersions, also describe the CaFe<sub>4</sub>Sb<sub>12</sub> case) and is one of the key properties determining the phonon dispersion. The other relevant parameter is indeed the relatively small rattler-cage spring constant. These two parameters determine, respectively, the wide separation between the acoustic and optical modes and the conspicuous flattening of the second optical mode (thick orange line). The latter implies a wide range of  $k$ -values for which the phonon group velocity is very close to zero, describing a rather localized phonon mode, reminiscent of the Einstein oscillators scenario. In view of the ratio  $K_{\text{eff}}^{\text{Ca,Fe-Ca}}/K_{\text{eff}}^{\text{K,Fe-K}} \approx 2/3$  (see table I) we propose that the CaFe<sub>4</sub>Sb<sub>12</sub> and KFe<sub>4</sub>Sb<sub>12</sub> vibrational dynamics are, respectively, described by figures 3(a)-(c) and 3(g)-(i). The range of values in the  $k_{\text{rs}}^R$  leaves the acoustic and first optical modes unchanged (red and green lines), while pushing the second optical mode (orange) up, causing this mode to interact with the third one (blue).

The mass relation of the BaFe<sub>4</sub>Sb<sub>12</sub> case is represented in figures 3(j)-(o). We now observe a smaller frequency gap between the acoustic and optical modes (due

to the filler-cage mass relation) and a much smaller region wherein the second optical mode is flat, due to the large rattler-cage coupling. Here, the parameter range is similar to the one adopted in the CeRu<sub>4</sub>As<sub>12</sub> [35] and LaPt<sub>4</sub>Ge<sub>12</sub> [50] cases, which allows us to pinpoint that the filler-cage mass relation is also responsible for a larger flattening of the optical mode, contributing to the phonon localization as recently proposed [51]. The value of the  $k_{\text{cc}}^{\text{Ba}}$  constant (reflecting the large  $K_{\text{eff}}^{\text{Ba,Fe-Fe}}$ ) is twice the value for the other heavy-filler filled skutterudites and it essentially increases the frequency of the higher energy (blue) optical mode. In comparison to the K (Ca) case, this shift of the third optical mode to a higher frequency causes the decoupling of this mode from the second optical mode, which in the Ba case turns out to interact mainly with the first optical mode.

## B. X-ray diffraction and elastic properties

We now turn to the  $P$  dependent XRD experiments. In figures 4(a) – (e) representative data of the XRD experiments, after removing the background, are presented for all samples. The main diffraction peaks of the skutterudite structure are marked in red as a reference. The powder profile was compared to the skutterudite crystal structure (the thick red lines in figures 4(a) – (e)) and the  $P$  dependence of the lattice parameters was extracted from the peak positions. The arrows are pointing to peaks that are not part of the skutterudite phase. These new peaks are likely due to the sample decomposition at high  $P$  or the pressure apparatus. We exclude any relevant secondary phase due to the high crystallographic quality of our samples at room conditions [52].

Our analysis of the XRD experiments are in figures 5(a) – (d). In figure 5(a), the unit cell volumes ( $V$ ) as a function of  $P$  of all samples are presented. It is tempting to associate the skutterudite elastic properties to the relation between the cage volume and the filler cationic size. We then compile in figure 5(b) a phenomenological parameter: the cage empty volume fraction  $f_E$ , that we define as  $f_E = 1 - V_R/V_C$ , where  $V_R$  is the  $R$  cationic volume and  $V_C$  is the Sb cage volume, as a function of  $P$ . The cage is represented in the inset of figure 5(b) as a reference.

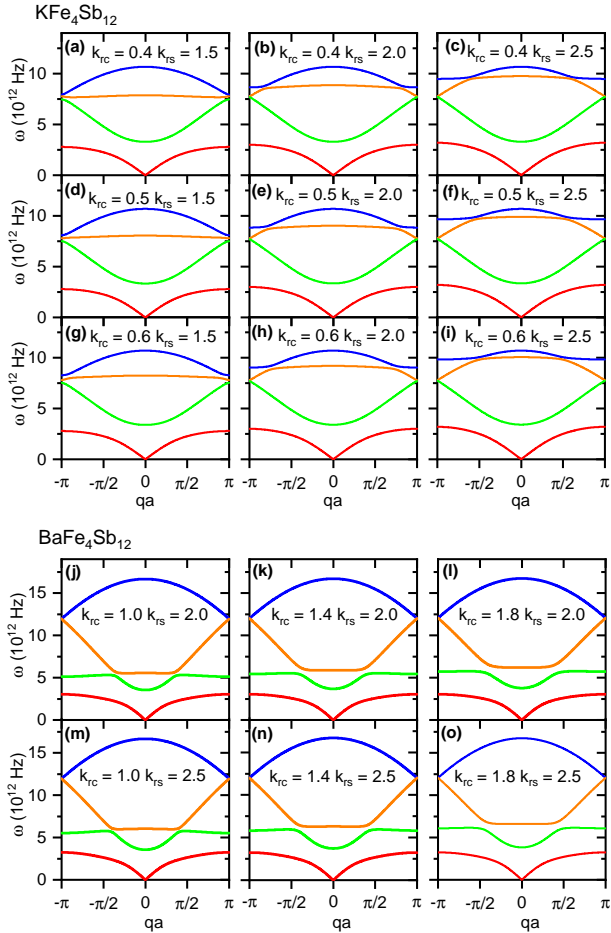


Figure 3. Effective 1D correlated rattling model for the  $R = \text{K}$  ( $\text{Ca}$ ) and  $\text{Ba}$  samples. In ascending frequency, we have the acoustic mode (red) and the first, (green), second (orange) and third (blue) optical phonon modes. The modes are displayed as function of  $qa$  where  $a$  is the material lattice constant and  $q$  is the phonon wave-vector. In panels (a) – (i), the mass relation between the vibrating elements is that of the  $R = \text{K}$  case and in panels (j) – (o), the mass relation between the vibrating elements is that of the  $R = \text{Ba}$  case. The adopted parameters are:  $k_{\text{cs}}^{\text{R}} = 1.8 \text{ eV}/\text{\AA}^2$  for all panels and  $k_{\text{cc}}^{\text{K}} = 10 \text{ eV}/\text{\AA}^2$ , in panels (a)–(i), and  $k_{\text{cc}}^{\text{Ba}} = 25 \text{ eV}/\text{\AA}^2$ , in panels (j)–(o), reflecting the different  $K_{\text{eff}}^{\text{R, Fe-Fe}}$  parameters. The  $k_{\text{rs}}^{\text{R}}$  and  $k_{\text{rc}}^{\text{R}}$  range of values are indicated in each panel.

The volume pressure dependence is investigated by fitting  $V \times P$  data to the Birch-Murnaghan (BM) model [36]:

$$P(V) = \frac{3}{2} B_0 \left[ \left( \frac{V}{V_0} \right)^{-\frac{7}{3}} - \left( \frac{V}{V_0} \right)^{-\frac{5}{3}} \right] \left\{ 1 + \frac{3}{4} (B_0' - 4) \left[ \left( \frac{V}{V_0} \right)^{-\frac{2}{3}} - 1 \right] \right\} \quad (1)$$

where  $V$  is the sample unit cell volume,  $V_0$  is the sample volume at room conditions,  $B_0$  is the bulk modulus and  $B_0'$  is the bulk modulus derivative. We keep  $B_0' = 4$

Table II. Parameters of the Birch-Murnaghan model for all  $R\text{Fe}_4\text{Sb}_{12}$  samples.

$R =$	Na	K	Ca	Sr	Ba
$V_0 (\text{\AA}^3)$	768.3(7)	787.8(2)	778.7(5)	777.6(5)	772.0(3)
$B_0 (\text{GPa})$	94(7)	77(5)	87(6)	91(6)	99(3)

GPa, as recently adopted to describe other skutterudites [53, 54] in this pressure range. Values obtained for  $V_0$  and  $B_0$  are compiled in table II. The  $V_0$  values obtained from the fitting deviate only about 1% from the experimentally determined from x-ray diffraction at room conditions suggesting the adequacy of our analysis. The  $V \times P$  data and their respective fitting are in figure 5(c).

The  $B_0$  values thus obtained range from 77 GPa ( $R = \text{K}$ ) to 99 GPa ( $R = \text{Ba}$ ). The values compare well with those obtained for other  $R\text{Fe}_4\text{Sb}_{12}$  based skutterudites, such as  $\text{EuFe}_4\text{Sb}_{12}$  [53] and  $\text{CeFe}_4\text{Sb}_{12}$  [55, 56]. The latter further suggests that  $B_0$  reflects the rigidity of the  $\text{Fe}_4\text{Sb}_{12}$  framework which, however, is not in total  $R$  independent. The experimentally obtained  $B_0$  parameters are in the range of the values previously obtained by calculations of the  $R = \text{Ca}$ ,  $\text{Sr}$  and  $\text{Ba}$  cases [17]. It is noteworthy, however, that the calculated values are nearly  $R$  independent and about 80 GPa. Our results also compare well with other  $\text{Sb}$ -based skutterudites, such as  $\text{CoSb}_3$  [54], in agreement with the understanding that the pnictogen square ring rigidity dominates the skutterudite elastic properties. Indeed, the wider variation in  $B_0$  is observed when the pnictogen is changed, with  $\text{P}$  forming characteristically rigid cages [55].

In possession of the  $B_0$  values, we then obtain the materials' compressibility  $\beta$  as a function of  $P$ . The results are displayed in figure 5(d). The compressibility data express well how the elastic properties depend on  $R$ : it is shown that the  $\text{K}$  and  $\text{Ca}$  filled materials have larger  $\beta$  while the  $\text{Ba}$  and  $\text{Na}$  filled materials have smaller  $\beta$ . It is a natural assumption to speculate that the higher  $f_E$  more compressible would be the material. If the whole data is inspected, this tendency is not obeyed. For instance, the  $\text{Ca}$  filled material, which has the largest  $f_E$ , is not the most compressible. If, however, we focus on either the  $R^{1+}$  or  $R^{2+}$  filled materials, an interesting picture emerges. Restricting the analysis to the case of the  $R^{1+}$  fillers, one notes that this simple picture does not work and  $\beta$  does not correlate with  $f_E$ , with the  $\text{K}$  filled material being the more compressible. Now, if one inspects the case  $R^{2+}$  fillers case, the experimentally obtained picture obeys the proposed trend, with the  $\text{Ca}$  filled material being the more compressible.

The case of the alkaline earth filled materials is distinct due to the presence of the heavy  $\text{Sr}$  and  $\text{Ba}$  fillers. Here,  $\text{Sr}$  and  $\text{Ba}$  virtual atomic  $4d$  and  $5d$  states, respectively, are more extended in real space as well as energetically accessible than the case of the  $\text{Ca}$  virtual  $3d$  states.

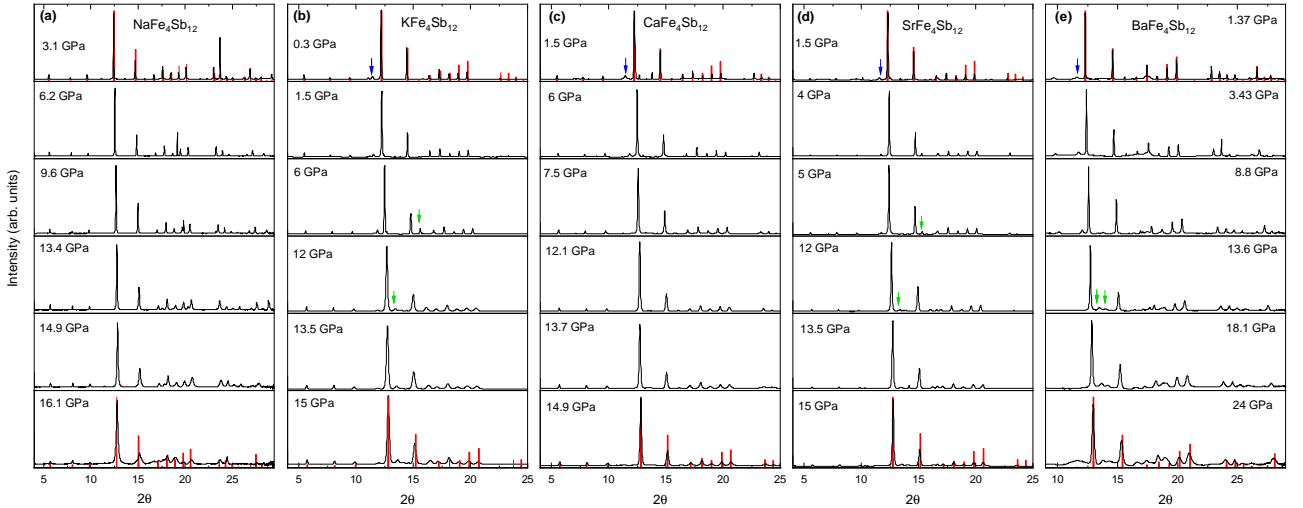


Figure 4. Representative  $P$  dependent XRD experiments for all  $R\text{Fe}_4\text{Sb}_{12}$  filled skutterudite, wherein we have: (a)  $R = \text{Na}$ ; (b)  $R = \text{K}$ ; (c)  $R = \text{Ca}$ ; (d)  $R = \text{Sr}$ ; and (e)  $R = \text{Ba}$ . The  $P$  is as indicated in the panels. The thick red lines represent the diffraction peaks of the skutterudite structure. The green arrows point to diffraction peaks not ascribed to the skutterudite phase. These peaks are not present at room conditions [52] and may be due to either the pressure apparatus or due to partial sample decomposition at high  $P$ .

Thus, the  $4d$  and  $5d$  states may take part in the filler-cage bonding which, in this scenario, is not completely ionic in character, as has been proposed for La filled skutterudites [57]. To verify this hypothesis, we performed DFT calculations of the filler-cage bonding properties.

We focus our analysis on the DFT results on the filler derived atomic orbitals (AOs) contribution for the molecular orbitals (MOs) with the highest superposition with the Sb-derived  $5p$  states, since these are precisely the MOs contributing the most to the filler-cage bonding. These MOs sit in the vicinity of the Fermi Level (see Ref. [52]). Our results show that whereas the  $4d$  and  $5d$  virtual AOs from Sr and Ba, respectively, take part in the formation of these MOs, Ca only contributes its  $3p$  states to the bonding MOs. In table III, we list the filler derived AOs contributing the most (largest superposing orbitals) to the formation of the filler-cage bonding MOs. The MOs symmetry classification is indicated and is made in terms of the irreducible representations of the  $T_h$  group, which is the point group symmetry of the  $R$  site [58, 59]. The results were obtained at room conditions and at high  $P$  ( $\approx 13.6$  GPa). The  $P$  effect was simulated by adopting the results from our XRD experiments.

As can be observed, pressure has nearly no effect on the bonding in the case of the Ca filler, whereas it further stabilizes and increases the  $d$  states participation in the Sr and Ba filled materials. This effect is particularly large in the case of Ba, for which an increase of more than  $\gtrsim 40\%$  of the  $5d$  orbital contribution to MOs enrolled in the filler-cage bonding is observed in the high  $P$  calculations. This result means that on top of geometrical considerations, one must consider that  $P$  induces further stabilization to the filler-cage bonding via the available

virtual  $nd$  states, rendering the material more rigid. Our findings thus suggest that the association between  $B_0$  (or  $\beta$ ) and  $f_E$  in the case of the  $R^{2+}$  fillers actually reflects a deeper understanding of the problem based upon the filler-cage bonding properties, in particular in the case of the heavy fillers. This mechanism could also be at work in the context of the partially filled  $M_y\text{Co}_4\text{Sb}_{12}$  skutterudites, for which it is observed that when  $M$  is a heavy filler, in particular in the cases of  $M = \text{La}$  and  $\text{Yb}$ , the material is more rigid [54]. Moreover, our calculations suggest an association between the participation of the Ba  $5d$  states in the filler-cage bonding and the relatively large value of the  $K_{\text{eff}}^{\text{Fe-Ba}}$  parameter.

A better visualization of the filler-cage bonding, in particular of the  $d$ -character of the MOs in the Sr and Ba case, can be observed in figure 6, wherein we depict the MOs related to the results listed in table III. The plots are contour plots of mentioned MOs and illustrate the real space charge distribution around the filler atom, which is located at the center of the figures. As it is clear, the plotted MOs are dominated by orbitals of  $d$ -character in the case of Sr and Ba filled material, whereas in the case of Ca filled material the presence of the  $3p$  lobe dominating the MOs is clearly distinguishable.

Lastly, we comment on the significant broadening of the diffraction peaks for high pressures that is observed. Starting at about 12 GPa in the  $R = \text{Na}$  and  $\text{K}$  cases and at higher  $P$  in the case of the alkaline earth filled skutterudites, the peaks' broadening amount to an increasing structural disorder induced by  $P$ . The alkaline earth filled materials are suggested to be relatively less susceptible to the disorder increase by  $P$ . Indeed, the diffraction peaks can still be observed for  $P$  up to 24

Table III. The highest filler derived superposing AOs to the formation of the MOs connected to the filler-cage bonding. The nature of the AOs and the symmetry character of the MOs are indicated. The Final orbital composition analysis was performed adopting the Ros-Schuit partition method via the Multifwfn program [60].

$R$	AOs character	Room Pressure		$\sim 13.6$ GPa	
		Orbital Cont. (%)	$E - E_F$ (eV)	Orbital Cont. (%)	$E - E_F$ (eV)
Ca	$3p_x$ ( $t_u$ )	30.77	-3.23	30.82	-3.46
Sr	$4d_{xy}, 4d_{xz}, 4d_{yz}$ ( $t_g$ )	11.84	-1.70	15.37	-1.82
Ba	$5d_{xy}, 5d_{xz}, 5d_{yz}$ ( $t_g$ )	19.54	-1.60	28.00	-1.68

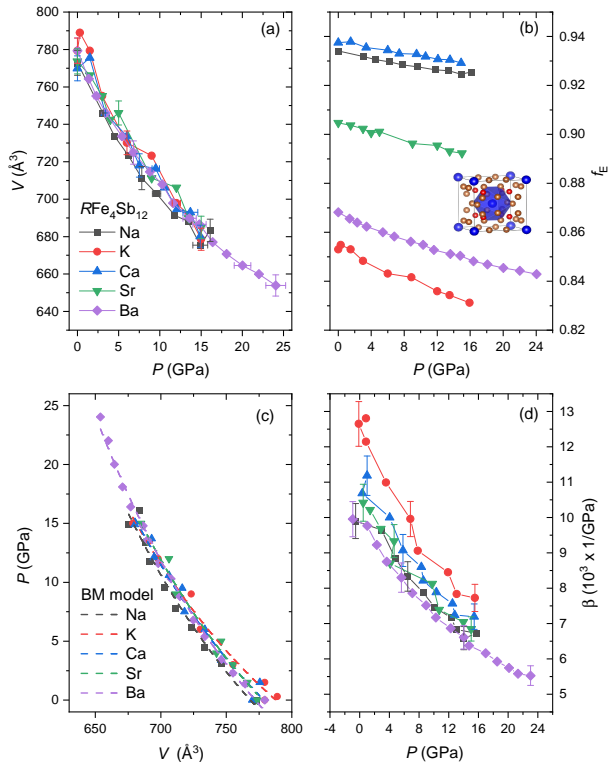


Figure 5. (a) The unit cell volume  $V$  as function of  $P$ . Error bars for  $P$  are estimated from the half-width at half maximum of the ruby fluorescence spectra and amount to about 3 – 5 % in this pressure interval. (b) The cage empty volume fraction  $f_E$  (see text) as a function of  $P$ . The inset shows a representation of the skutterudite structure highlighting the Sb cage around the filler site (the cage volume was calculated with VESTA [47]). (c) The  $P$  as a function of  $V$  data and their respective fittings to the Birch-Murnaghan model. (d) The compressibility  $\beta$  as a function of  $P$  for all samples.

GPa in the  $\text{BaFe}_4\text{Sb}_{12}$  case. The skutterudite structure is mainly stabilized by a combination of geometric and charge constraints related to the filler and cages sizes and charge distribution [2, 3]. We thus conclude that the larger structural stability of alkaline earth filled materials is likely due to the bonding stabilization of the extra charge offered by the  $R^{2+}$  cations.

#### IV. SUMMARY AND CONCLUSIONS

The site specific vibrational properties of the  $R = \text{K}, \text{Ca}$  and  $\text{Ba}$  filled skutterudites  $R\text{Fe}_4\text{Sb}_{12}$  were investigated by EXAFS experiments. As concluded from the effective spring constants obtained from experiments, materials filled with light-weight cations display weak rattler-cage couplings, reminiscent of the independent rattler scenario, and the  $R = \text{Ba}$  material display a characteristic strong Fe-Fe coupling. Based upon an effective 1D model for the skutterudite phonon dispersion, we proposed that the  $R = \text{K}$  and  $\text{Ca}$  filled skutterudites should display a conspicuous optical flat mode in accordance with the Einstein oscillator scenario.

We thus introduced our pressured dependent experiments. The  $V \times P$  curves were determined and fitted to the Birch-Murnaghan model to extract the bulk modulus  $B_0$  and then the compressibility  $\beta$ . We found that the geometrical parameter  $f_E$  cannot explain the  $B_0$  (or  $\beta$ ) dependence as a function of  $R$ . A geometrical relation, however, was observed to hold in the case of the  $R^{2+}$  filled materials. By considering DFT calculations, we uncovered that this association between  $B_0$  (or  $\beta$ ) and  $f_E$  actually reflects an emerging property of the filler-cage bonding, which is particularly relevant for heavy fillers. Moreover, the filler-cage bonding can also explain the large  $K_{\text{eff}}^{\text{Fe-Ba}}$  parameter, since the contribution from  $\text{Ba } 5d$  states to bonding makes the  $\text{Ba}$  more tightly coupled to the cage (no “independent” rattler in this case).

From the point of view of material design, our results suggest that synthesizing mixed filled skutterudites, featuring light and heavy fillers, is a good strategy to introduce localized vibrational modes (“rattlers”) in the material’s vibrational dynamics. This speculation has some ground on our calculations showing that the bonding scheme in skutterudites may include a certain degree of covalency in the case of heavy fillers. Thus, introducing light cations into materials mainly filled with heavy cations create a situation wherein the light fillers are weakly bonded and sitting in an oversized cage.

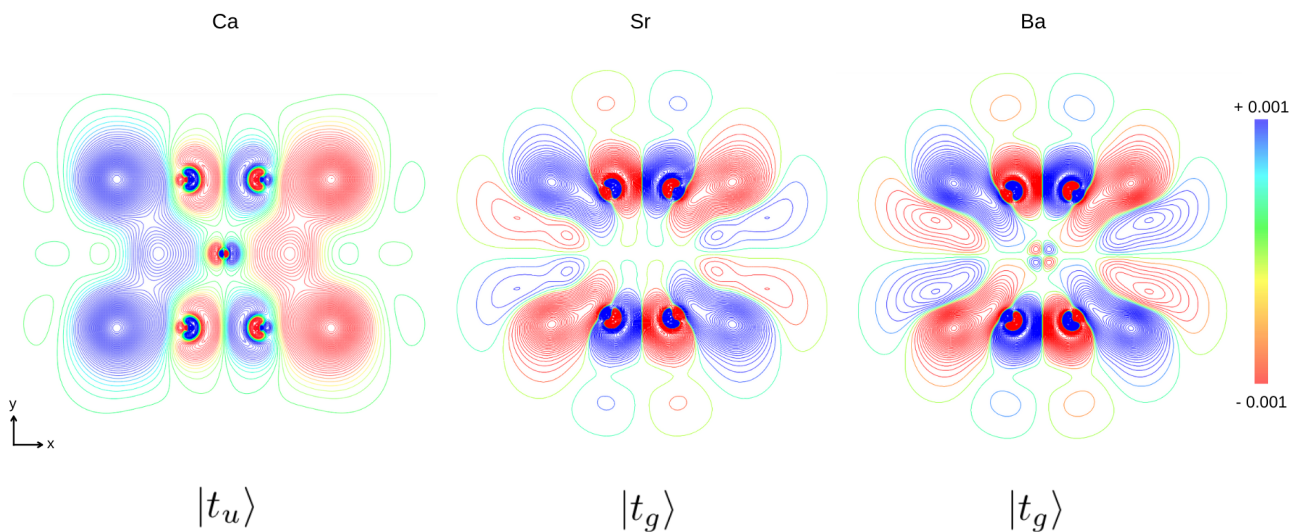


Figure 6. Contour plots for the MOs describing the filler-cage bonding in the  $(x, y)$  plane in the cases of the Ca, Sr and Ba filled materials as indicated. The figures are formed by 120 contours in the isovalue interval indicated in the color scale in the left side of the figure. Ligand Orbitals are plotted via the Gabedit program [61].

#### ACKNOWLEDGMENTS

The authors acknowledge CNPEM-LNLS for the concession of beam time (proposals No. 20160180, No. 20160181, No. 20170709 and No. 20190018). The XAFS2 and XDS beamlines staff are acknowledged for the assistance during the experiments. The Fundação de Amparo à Pesquisa do Estado de São Paulo financial sup-

port is acknowledged by M.R.C. (grant No. 2019/05150-7 and grant No. 2020/13701-0) and F.A.G. (grant No. 2019/25665-1). This study was financed in part by CAPES - Finance Code 001. E.M.B. acknowledges Fundação Carlos Chagas Filho de Amparo à Pesquisa do Estado do Rio de Janeiro (grant No. E-26/202.798/2019). A.L.J. thanks J. Grin for his steady support and interest in this work.

- 
- [1] W. Jeitschko and D. Braun, Acta Crystallographica Section B: Structural Crystallography and Crystal Chemistry **33**, 3401 (1977).
- [2] R. Gumeniuk, H. Borrmann, A. Ormeci, H. Rosner, W. Schnelle, M. Nicklas, Y. Grin, and A. Leithe-Jasper, Zeitschrift Fur Kristallographie-Crystalline Materials **225**, 531 (2010).
- [3] H. Luo, J. W. Krizan, L. Muechler, N. Haldolaarachchige, T. Klimczuk, W. Xie, M. K. Fuccillo, C. Felser, and R. J. Cava, Nature Communications **6**, 10.1038/ncomms7489 (2015).
- [4] V. Keppens, D. Mandrus, B. C. Sales, B. C. Chakoumakos, P. Dai, R. Coldea, M. B. Maple, D. A. Gajewski, E. J. Freeman, and S. Bennington, Nature **395**, 876 (1998).
- [5] G. J. Snyder and E. S. Toberer, Nature materials **7**, 105 (2008).
- [6] J. Mao, Z. Liu, J. Zhou, H. Zhu, Q. Zhang, G. Chen, and Z. Ren, Advances in Physics **67**, 69 (2018).
- [7] S. El Oualid, I. Kogut, M. Benyahia, E. Geczi, U. Kruck, F. Kosior, P. Masschelein, C. Candolfi, A. Dauscher, J. D. Koenig, A. Jacquot, T. Caillat, E. Alleno, and B. Lenoir, Advanced Energy Materials **11**, 2100580 (2021).
- [8] R. P. Hermann, F. Grandjean, and G. J. Long, American Journal of Physics **73**, 110 (2005).
- [9] F. A. Garcia, D. J. Garcia, M. A. Avila, J. M. Vargas, P. G. Pagliuso, C. Rettori, M. C. G. Passeggi, S. B. Osleroff, P. Schlottmann, B. Alascio, and Z. Fisk, Physical Review B **80**, 052401 (2009).
- [10] F. A. Garcia, R. Gumeniuk, W. Schnelle, J. Sichelschmidt, A. Leithe-Jasper, Y. Grin, and F. Steglich, Physical Review B **85**, 134402 (2012).
- [11] M. M. Koza, M. R. Johnson, R. Viennois, H. Mutka, L. Girard, and D. Ravot, Nat Mater **7**, 805 (2008).
- [12] R. Wei, G. Huiyuan, Z. Zihao, and Z. Lixia, Physical Review Letters **118**, 245901 (2017).
- [13] W. Zhao, P. Wei, Q. Zhang, H. Peng, W. Zhu, D. Tang, J. Yu, H. Zhou, Z. Liu, X. Mu, D. He, J. Li, C. Wang, X. Tang, and J. Yang, Nature Communications **6**, 6197 (2015).
- [14] J. Gainza, F. Serrano-Sanchez, J. E. Rodrigues, J. Prado-Gonjal, N. M. Nemes, N. Biskup, O. J. Dura, J. L. Martinez, F. Fauth, and J. A. Alonso, Advanced Functional Materials **30**, 2001651 (2020).
- [15] W. Schnelle, A. Leithe-Jasper, H. Rosner, R. Cardoso-Gil, R. Gumeniuk, D. Trots, J. A. Mydosh, and Y. Grin, Physical Review B **77**, 094421 (2008).
- [16] M. M. Koza, L. Capogna, A. Leithe-Jasper, H. Rosner,



- W. Schnelle, H. Mutka, M. R. Johnson, C. Ritter, and Y. Grin, *Physical Review B* **81**, 174302 (2010).
- [17] M. M. Koza, A. Leithe-Jasper, H. Rosner, W. Schnelle, H. Mutka, M. R. Johnson, M. Krisch, L. Capogna, and Y. Grin, *Physical Review B* **84**, 014306 (2011).
- [18] J. L. Feldman, D. J. Singh, and N. Bernstein, *Physical Review B* **89**, 224304 (2014).
- [19] A. Mochel, I. Sergueev, N. Nguyen, G. J. Long, F. Grandjean, D. C. Johnson, and R. P. Hermann, *Physical Review B* **84**, 064302 (2011).
- [20] M. M. Koza, M. Boehm, E. Sischka, W. Schnelle, H. Mutka, and A. Leithe-Jasper, *Physical Review B* **91**, 014305 (2015).
- [21] J. Prado-Gonjal, F. Serrano-Sanchez, N. M. Nemes, O. J. Dura, J. L. Martinez, M. T. Fernandez-Diaz, F. Fauth, and J. A. Alonso, *Applied Physics Letters* **111**, 083902 (2017).
- [22] S. H. Bae, K. H. Lee, and S.-M. Choi, *Intermetallics* **105**, 44 (2019).
- [23] Y. Wang, J. Mao, Q. Jie, B. Ge, and Z. Ren, *Applied Physics Letters* **110**, 163901 (2017).
- [24] M. B. Maple, R. E. Baumbach, J. J. Hamlin, D. A. Zocco, B. J. Taylor, N. P. Butch, J. R. Jeffries, S. T. Weir, B. C. Sales, D. Mandrus, M. A. McGuire, A. S. Sefat, R. Jin, Y. K. Vohra, J. H. Chu, and I. R. Fisher, *Physica B: Condensed Matter Proceedings of the International Conference on Strongly Correlated Electron Systems*, **404**, 2924 (2009).
- [25] A. Leithe-Jasper, W. Schnelle, H. Rosner, N. Senthilkumar, A. Rabis, M. Baenitz, A. Gippius, E. Morozova, J. A. Mydosh, and Y. Grin, *Physical Review Letters* **91**, 037208 (2003).
- [26] A. Leithe-Jasper, W. Schnelle, H. Rosner, M. Baenitz, A. Rabis, A. A. Gippius, E. N. Morozova, H. Borrmann, U. Burkhardt, R. Ramlau, U. Schwarz, J. A. Mydosh, Y. Grin, V. Ksenofontov, and S. Reiman, *Physical Review B* **70**, 214418 (2004).
- [27] D. Berardan, E. Alleno, and C. Godart, *Journal of Magnetism and Magnetic Materials* **285**, 245 (2005).
- [28] E. Matsuoka, K. Hayashi, A. Ikeda, K. Tanaka, T. Takabatake, and M. Matsumura, *Journal of the Physical Society of Japan* **74**, 1382 (2005).
- [29] A. Leithe-Jasper, W. Schnelle, H. Rosner, W. Schweika, and O. Isnard, *Physical Review B* **90**, 144416 (2014).
- [30] S.-i. Kimura, H. Im, T. Mizuno, S. Narazu, E. Matsuoka, and T. Takabatake, *Physical Review B* **75**, 245106 (2007).
- [31] B. Mounssef, M. R. Cantarino, E. M. Bittar, T. M. Germano, A. Leithe-Jasper, and F. A. Garcia, *Physical Review B* **99**, 035152 (2019).
- [32] D. Cao, F. Bridges, P. Chesler, S. Bushart, E. D. Bauer, and M. B. Maple, *Physical Review B* **70**, 094109 (2004).
- [33] F. Bridges, B. Car, L. Sutton, M. Hoffman-Stapleton, T. Keiber, R. E. Baumbach, M. B. Maple, Z. Henkie, and R. Wawryk, *Physical Review B* **91**, 014109 (2015).
- [34] F. Bridges, *Modern Physics Letters B* **30**, 1630001 (2016).
- [35] T. Keiber and F. Bridges, *Physical Review B* **92**, 134111 (2015).
- [36] F. Birch, *Physical Review* **71**, 809 (1947).
- [37] J. R. L. Mardegan, G. Fabbri, L. S. I. Veiga, C. Adriano, M. A. Avila, D. Haskel, and C. Giles, *Physical Review B* **88**, 144105 (2013).
- [38] S. J. A. Figueroa, J. C. Mauricio, J. Murari, D. B. Beniz, J. R. Piton, H. H. Slepicka, M. F. a. d. Sousa, A. M. Espíndola, and A. P. S. Levinsky, *Journal of Physics: Conference Series* **712**, 012022 (2016).
- [39] J. J. Rehr and R. C. Albers, *Reviews of Modern Physics* **72**, 621 (2000).
- [40] B. Ravel and M. Newville, *Journal of Synchrotron Radiation* **12**, 537 (2005).
- [41] F. A. Lima, M. E. Saleta, R. J. S. Pagliuca, M. A. Eleotério, R. D. Reis, J. Fonseca Júnior, B. Meyer, E. M. Bittar, N. M. Souza-Neto, and E. Granado, *Journal of Synchrotron Radiation* **23**, 1538 (2016).
- [42] B. H. Toby and R. B. Von Dreele, *Journal of Applied Crystallography* **46**, 544 (2013).
- [43] F. Neese, F. Wennmo, U. Becker, and C. Riplinger, *The Journal of Chemical Physics* **152**, 224108 (2020).
- [44] F. Neese, *WIREs Computational Molecular Science* **2**, 73 (2012).
- [45] A. Dittmer, R. Izsák, F. Neese, and D. Maganas, *Inorganic Chemistry* **58**, 9303 (2019).
- [46] H. Luo, J. W. Krizan, L. Muechler, N. Haldolaarachchige, T. Klimczuk, W. Xie, M. K. Fuccillo, C. Felser, and R. J. Cava, *Nature Communications* **6**, 6489 (2015).
- [47] K. Momma and F. Izumi, *Journal of Applied Crystallography* **41**, 653 (2008).
- [48] Y. Hu, J. R. Salvador, N. Chen, A. Alatas, and Y.-J. Kim, *Journal of Applied Physics* **130**, 185105 (2021).
- [49] J. E. F. S. Rodrigues, J. Gainza, F. Serrano-Sánchez, C. Marini, Y. Huttel, N. M. Nemes, J. L. Martínez, and J. A. Alonso, *Chemistry of Materials* **34**, 1213 (2022).
- [50] M. R. Cantarino, R. Lora-Serrano, R. Gumeniuk, W. Schnelle, J. Sichelschmidt, A. Leithe-Jasper, Y. Grin, and F. A. Garcia, in preparation (2022).
- [51] A. Valério, R. F. S. Penacchio, M. B. Estradiote, M. R. Cantarino, F. A. Garcia, S. L. Morelhão, N. Rafter, S. W. Kycia, G. A. Calligaris, and C. M. R. Remédios, *MRS Communications* **10**, 265 (2020).
- [52] J. G. de Abrantes, M. R. Cantarino, W. R. da Silva Neto, V. V. Freire, A. G. de Figueiredo, T. M. Germano, B. Mounssef Jr., M. B. Eduardo, A. Leithe-Jasper, and F. A. Garcia, *Supplemental material* (2022).
- [53] I. Sergueev, K. Glazyrin, I. Kantor, M. A. McGuire, A. I. Chumakov, B. Klobes, B. C. Sales, and R. P. Hermann, *Physical Review B* **91**, 224304 (2015).
- [54] J. a. E. F. S. Rodrigues, J. Gainza, F. Serrano-Sánchez, M. M. Ferrer, G. S. L. Fabris, J. R. Sambrano, N. M. Nemes, J. L. Martínez, C. Popescu, and J. A. Alonso, *Inorganic Chemistry* **60**, 7413 (2021).
- [55] I. Shirovani, T. Noro, J. Hayashi, C. Sekine, R. Giri, and T. Kikegawa, *Journal of Physics: Condensed Matter* **16**, 7853 (2004).
- [56] W. Liu, Q. Jie, Q. Li, Z. Chen, and B. Li, *Physica B: Condensed Matter* **406**, 52 (2011).
- [57] A. P. Grosvenor, R. G. Cavell, and A. Mar, *Physical Review B* **74**, 125102 (2006).
- [58] K. Takegahara, H. Harima, and A. Yanase, *Journal of the Physical Society of Japan* **70**, 1190 (2001).
- [59] D. J. Garcia, F. A. Garcia, J. G. S. Duque, P. G. Pagliuso, C. Rettori, P. Schlottmann, M. S. Torikachvili, and S. B. Oseroff, *Physical Review B* **78**, 174428 (2008).
- [60] T. Lu and F. Chen, *Journal of Computational Chemistry* **33**, 580 (2012).
- [61] A.-R. Allouche, *Journal of Computational Chemistry* **32**, 174 (2011).